2021-06-16

Behavior of Unreinforced Lightweight Cellular Concrete Backfill for Reinforced Concrete Retaining Walls

Ryan Jeffrey Wilkinson
Brigham Young University

Behavior of Unreinforced Lightweight Cellular Concrete Backfill for Reinforced Concrete Retaining Walls

Ryan Jeffrey Wilkinson

A thesis submitted to the faculty of
Brigham Young University
in partial fulfillment of the requirements for the degree of

Master of Science

Kyle M. Rollins, Chair
Fernando S. Fonseca
Johnn P. Judd

Department of Civil and Environmental Engineering

Brigham Young University

ABSTRACT

Behavior of Unreinforced Lightweight Cellular Concrete Backfill
for Reinforced Concrete Retaining Walls

Ryan Jeffrey Wilkinson
Department of Civil and Environmental Engineering, BYU
Master of Science

Lightweight cellular concrete (LCC) is a mixture of cement, water and foam, with a density less than 50 pcf. This material is being used increasingly often in a variety of construction applications due to its self-leveling, self-compacting, and self-consolidating properties. LCC may be used as a backfill or structural fill in areas where traditional granular backfill might normally be used. This material may be especially advantageous in areas where the underlying soil may not support the weight of a raised earth embankment. Testing on the behavior of LCC when used as backfill behind retaining walls is relatively limited. The effects of surcharge on the development of active pressure material are unknown.

Two large-scale active pressure tests were conducted in the structures laboratory of Brigham Young University. Each test was performed within a 10-ft x 10-ft x 12-ft box that was filled with four lifts of LCC. Hydraulic jacks mounted to a steel reaction frame provided a surcharge load to the LCC surface. In the first test, the LCC was confined on three sides by the reaction frame, while the fourth side was confined by a reinforced concrete cantilever (RCC) wall. Both vertical and horizontal pressures and deflections were measured to determine the effect of the surcharge load on the development of active pressure behind the wall. In the second test, the LCC was confined on three sides and exposed on the fourth. Surcharge was applied to this sample in a similar fashion until the LCC reached ultimate failure. Vertical pressures and displacements, along with horizontal displacements, were measured in this test. Sample cylinders of LCC were cast at the time the test box was filled. These samples were tested periodically to determine the material strength and density.

It was observed that the LCC backfill developed active pressure most similarly to a granular soil with a friction angle of 34º and a cohesion between 700 and 1600 psf. The RCC wall was seen to add vertical bearing capacity to the LCC, as well as prevent the catastrophic and brittle failure seen in the free-face test. It was also observed that an induced shear plane in the material dramatically decreased the total bearing capacity when compared to a uniformly loaded specimen with no induced shear plane. The results of this study were compared with design parameters given in previous research, and new design suggestions are presented herein.

Keywords: active pressure, backfill, cellular concrete, surcharge

ACKNOWLEDGEMENTS

I would like to express my gratitude to the many individuals who have assisted me with this thesis. The faculty and staff of BYU have been monumental in their support and encouragement through all the setbacks and trials that have occurred throughout this research. I would like to specifically thank Kyle M. Rollins for his dedication and perseverance that made this research possible. His efforts to coordinate with various contractors and researchers were invaluable to the success of this thesis.

I would also like to thank Dave Anderson, Rodney Mayo, and Andrew Cheney of the BYU Structures Laboratory for their immeasurable contributions, both in setting up the testing systems and in performing the tests. I likewise thank my fellow student researchers Christian Lundskog, Meghann Morgan, and Joel Smith, whose friendship and remarkable assistance made this research possible. We are also grateful to the Cell-Crete Corporation for supplying and placing the Lightweight Cellular Concrete (LCC) for this study. The staff at Gerhart Cole Inc. and various contractors from Cell-Crete Corporation also worked many long hours making sure this research was successful, and I am deeply grateful for the help they provided.

This study was funded through FHWA Transportation Pooled Fund TPF-5(433) Behavior of Reinforced and Unreinforced Lightweight Cellular Concrete (LCC) For Retaining Walls" and was supported by Departments of Transportation from Florida, Iowa, Kansas, Massachusetts, Minnesota, Michigan, New York, Oregon, Washington, along with the Federal Highway Administration. Utah served as the lead agency with David Stevens as the project manager. This support is gratefully acknowledged; however, the opinions, conclusions and recommendations contained herein do not necessarily represent those of the sponsoring organizations.

TABLE OF CONTENTS

LIST OF TABLES

LIST OF FIGURES

1 INTRODUCTION

Cellular concrete is a mixture of cement, water and foam, mixed at the time of casting so air pockets formed by the foam stay within the mixture as it cures. Like standard concrete, cellular concrete mixes can be varied to produce different strengths, variable set times and specialized densities. Cellular concrete density can range from 20 to 90 pcf (Elastizell, 2014). Higher densities and strengths can be achieved with the addition of aggregate (Spinney, 1993).

Lightweight cellular concrete (LCC) is a subcategory of cellular concrete, defined as a cellular concrete mix having a density of less than 50 pcf. It is gaining popularity for use as a structural backfill, providing may advantages over traditional backfill due to its light weight and relative ease of placement (Tian, Li, Zhao, Zhou, & Wang, 2009). Its self-consolidating and highly flowable properties enable it to fill voids around existing features while still maintaining a compressive strength comparable to well-compacted granular backfill.

LCC is often used as a replacement for backfill around bridge abutments in locations where existing utilities, high labor costs, tight deadlines or low native soil strength prevent the use of more traditional methods. Often, concrete retaining walls or mechanically stabilized earth (MSE) walls are constructed to hold the LCC in place when used in such applications; however, little is known about the interaction between the LCC and the retaining structure when a surcharge load is applied. LCC is considered both a structural material comparable to low-strength traditional concrete and a soil with a defined friction angle and cohesion. State

Departments of Transportation have differing requirements for the design of these retaining walls—some indicate the LCC backfill behaves like concrete so a retaining wall is not necessary, while some indicate LCC behaves like soil and must be supported by a retaining wall, MSE wall, or other retaining structure. Estimates have been made about the lateral pressures generated by the LCC when subjected to surcharge loads, but these estimates have primarily been made based on geotechnical properties measured during laboratory testing and correlations to the behavior of soils with similar properties. No large-scale tests directly measuring the interactions between LCC and a retaining structure have been recorded.

1.1 Research Objectives

This research project aims to clarify discrepancies regarding the design of concrete retaining walls for cellular concrete backfill—MSE wall behavior will be addressed in a subsequent research venture. This is the first of a five-part test series, each of which will have a different retaining structure or backfill configuration. The specific topics that will be addressed in this particular test include:

- The necessity of retaining structures supporting LCC backfill
- The presence or absence of failure planes within the LCC when loaded with a vertical surcharge, and if present, the configuration of such planes
- The validity of estimating the behavior of LCC using its material properties and correlations/equations developed for soils with similar properties
- Recommended design requirements for cantilevered retaining walls with LCC backfill
- Scalability and applicability of these test results

The project will not directly address the mechanical properties of LCC or the effects of various levels of confinement on the strength of the material, though these properties will be explored to develop correlations.

1.2 Scope of Work

This research includes designing and building a test apparatus (cantilevered reinforced concrete retaining wall, steel reaction frame, instrumentation, etc.) and performing a single surcharge test. Construction and testing were performed by the graduate students working on this and all subsequent tests, in conjunction with the structures laboratory staff at Brigham Young University (BYU). Third-party contractors were hired to do specialized work as required. Cell-Crete Corporation provided a crew of workers to mix and pour the cellular concrete; the BYU Precision Machining Lab (PML) assisted with the machining and welding of steel plates and beams; Gerhart Cole performed compression and density tests for LCC samples gathered during the pour; and the BYU Groundskeeping staff excavated and disposed of the LCC after testing was completed.

1.3 Outline of Report

This thesis contains nine chapters. Chapter 1 presents the scope of work and defines the objectives of this research. Chapter 2 contains background information regarding the uses and properties of cellular concrete and explores various active earth pressure theories. In Chapter 3, the test apparatus design and instrumentation are described. Chapter 4 contains preliminary test data gathered at BYU that contributed to the design of the main experiment. Chapter 5 contains laboratory test results of cellular concrete samples obtained during the time of casting. In Chapter 6, the results of the retained-face test are presented, while Chapter 7 contains the results

of the free-face test and compares it to the retained-face test. Chapter 8 gives a greater analysis of the results and presents design recommendations. Chapter 9 contains final conclusions and recommendations for future research.

2 LITERATURE REVIEW

2.1 Lightweight Cellular Concrete

Cellular concrete, composed of cement, water, and aerated foam, has been used in various applications since the early 1900s. The most popular use has been as insulation or fire-resistance within structures. Its use in geotechnical and structural applications is becoming ever more common as designers and contractors seek to build larger, more resilient infrastructure. Because of its light weight, ease of placement, and high strength relative to other structural fill products, it has the potential for a very wide range of uses. It can be pumped over long distances and can be mixed on-site, making it one of the most versatile fill materials available.

Lightweight cellular concrete (LCC) is defined in ACI 523 as "concrete made with hydraulic cement, water, and preformed foam to produce a hardened material with an oven-dry density of 50 lb/ft^3 (800 kg/m^3) or less." Higher-density cellular concrete can be manufactured when higher strength is required, but these high-density mixes usually require the addition of aggregate or slag.

2.2 Cellular Concrete Uses

Cellular concrete is used in a variety of applications including roadway construction, fill for abandoned pipelines, structural backfill, and filling voids around active utilities.

2.2.1 Roadway Use

Using cellular concrete as a road subbase has proved to be a highly effective method of road construction. Cellular concrete can be pumped for long distances and is self-leveling and self-compacting, reducing or eliminating the need for equipment and labor costs associated with placing and leveling the road subbase. The higher initial cost of the material can be quickly offset by the savings in labor (Nandi, Chatterjee, Samanta, & Hansda, 2016).

Cellular concrete has proved to be durable in a multitude of roadway projects around the world. Averyanov (2018) suggested that the fatigue performance of cellular concrete, when used as a subbase, is between 10 and 14 times more durable than traditional granular backfill. It also reduces overall settlement of roadways due to its light weight and moderate tensile strength compared to granular fills. These properties make this a particularly attractive material for use around bridge abutments and beneath bridge approaches. Studies reported by Black (2018) indicate that cellular concrete backfill behind abutments can provide passive resistance comparable to compacted granular fill and still be excavatable.

In areas with very soft native soils, roadways can be built up using cellular concrete without adding extreme vertical surcharge to the soil below. This reduces the overall cost of retaining structures, deep foundations, and potential settlement mitigation (Cox, 2005). If enough native soil is excavated below an embankment of cellular concrete, a net-zero pressure can be attained on the native soil, which eliminates the need for ground-improvement efforts prior to construction (Pradel & Tiwari, 2015). Pradel and Tiwari (2015) suggest that pre-manufactured products like geofoam may be used as a comparable lightweight fill, but the tendency of geofoam to dissolve when exposed to petroleum-based products such as gasoline and motor oil suggests that cellular concrete may provide a longer-lasting structure when the fill may be

exposed to gasoline or oil from a roadway. In addition, geofoam fill used for highway projects are usually two to three times more expensive to place than cellular concrete fill.

2.2.2 Use as Backfill Behind Walls

Retaining structures typically placed around cellular concrete embankments act as both a confinement measure and a protective coating. If cellular concrete is not encased by an exterior shell, it is left exposed to potential damages such as hailstorms and vehicle impacts. If such impacts were to occur, the cellular concrete structure could be easily damaged and the embankment may become structurally unstable (Pradel & Tiwari, 2015). Likewise, the top surface of a cellular concrete block should be protected against exposure to water to retain good freeze-thaw resistance. Resistance to freeze-thaw cycles increases with increasing density, and mixes with a density greater than 36 pcf are recommended for surfaces exposed to water ("Guide for Cast-in-Place Low-Density Cellular Concrete," 2006). Freeze-thaw cycles cause micro-cracks within the cellular concrete structure, which can lead to rapid deterioration of the concrete surface, as well as reduction in both compressive and tensile strength (Shang, Song, & Qin, 2008). To shield against this deterioration, a water barrier placed above the surface of the cellular concrete is widely recommended.

Both MSE walls and cantilevered retaining walls have been used to retain raised cellular concrete roadways and bridge approaches. Figure 2-1, from Pradel and Tiwari (2015), shows the design cross-section for a raised embankment constructed in San Jose, California, formed with cellular concrete placed above native fill. This cellular concrete fill was stabilized with MSE walls on each side and protected with a concrete slab above.

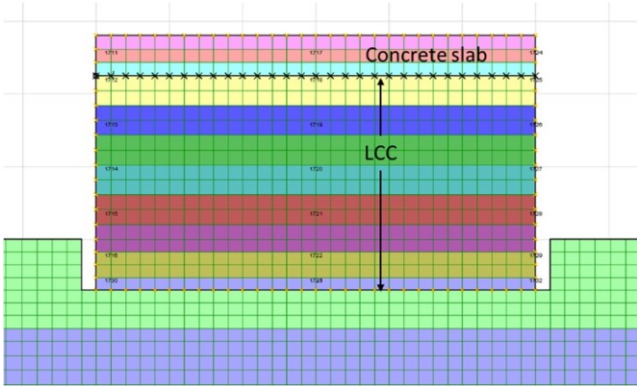

Figure 2-1: Design cross-section of a raised cellular concrete embankment (Pradel & Tiwari, 2015)

Once cured, cellular concrete does not creep or flow as a clay backfill might, so absent the presence of surcharge loads, the confining structure must only resist the fluid pressure of the wet cellular concrete before it has cured (Grutzeck, 2005). This statement is valid under the assumption that the top lifts induce so little vertical pressure on the lower lifts that negligible horizontal expansion occurs. Such an assumption is acceptable in most situations where additional vertical surcharge is not present because the material is very lightweight. In a static loading condition, a block of 30 pcf (4.7 kN/m^3) LCC with a height of 50 feet (15.25 m) imposes a stress at the bottom of the block of only 10-15% of its ultimate compressive strength. The range of maximum vertical stress at which this assumption is valid is unknown, but tall embankments or embankments that are exposed to high surcharge loads may invalidate the assumption.

2.3 Other Lightweight Fills

LCC is only one of many lightweight fills regularly used in construction. Other fills include shredded tires, polystyrene foam, Geofoam, natural volcanic material, expanded shale, wood fibers, and fly ash (FHWA, 2017). These other materials have all proven to be viable

alternatives to traditional backfill. Each jurisdiction has different limitations on use of these materials, and one may be more generally accepted in one jurisdiction than another.

2.4 Mechanical Properties of Low-Strength Cellular Concrete

2.4.1 Characterization

Cellular concrete behavior is most often defined by its unconfined compressive strength and its density. Using these two properties, many researchers have suggested correlations for estimating modulus of elasticity, thermal conductivity, and other properties. ASTM defines only a single test to determine the properties of a cellular concrete sample: ASTM C495, "Standard Test Method for Compressive Strength of Lightweight Insulating Concrete". In this specification, an unconfined compression test is used to compress the sample. Rahman, Zaidi, and Rahman (2010) suggest that the behavior of cellular concrete cannot be captured or modeled simply through compression tests, whether confined or unconfined. The behavior is too complex to be represented by a single test. Traditional Portland Cement concrete is typically characterized using only compressive strength because it is typically designed to act in compression. Because cellular concrete is often used in other applications such as seismic loading, soil remediation, and roadway support, it may experience failure in shear, tension, compression, or a combination of these stresses.

2.4.2 Unconfined Compressive Strength

Cellular concrete has a higher unconfined compressive strength than most compacted soils but a lower strength than traditional concretes. Table 2-1 contains typical mix design values

suggested for LCC as a function of cast density (Sutmoller, 2017). These values represent simple mix designs commonly used in industry—the actual design values of the material can be adjusted as necessary to produce a material with the desired performance.

Table 2-1: Typical cellular concrete mix guidelines (Sutmoller, 2017)

Cast Density		Typical Compressive Strength at 28 days		Portland Cement		Water		Foam Volume	
lb/ft³	kg/m³	psi	MPa	lb/yd³	kg/m³	gal	L	ft³/yd³	m³/m³
20	320	50	0.34	328	195	19.7	97.3	22.7	0.84
25	400	80	0.55	420	249	25.2	124.6	21.5	0.80
30	481	140	0.97	512	304	30.7	151.9	20.3	0.75
35	561	210	1.45	603	358	36.2	178.8	19.1	0.71
40	641	330	2.28	695	412	41.7	206.1	17.9	0.66
45	721	450	3.10	787	467	47.2	233.4	16.7	0.62
50	801	640	4.41	878	521	52.6	260.4	15.5	0.57
55	881	790	5.45	970	575	58.2	287.7	14.3	0.53
60	961	930	6.41	1062	630	63.7	315.0	13.1	0.49

As the density of the cast cellular concrete increases, the compressive strength tends to increase. Tests from Tiwari et al. (2017) suggest that a strong correlation exists between the density and unconfined compressive strength for cellular concrete between 3 and 8 kN/m^3 (20 to 50 pcf). Statistical analyses performed on various data sets support this assertion (Ni, Averyanov, Melese, & Tighe, 2018). The strength of the correlation is good, but some variability still exists within the samples. As seen in Figure 2-2, most of the samples fall within 0.5σ of the best-fit regression line, but a high degree of variability still exists within each batch.

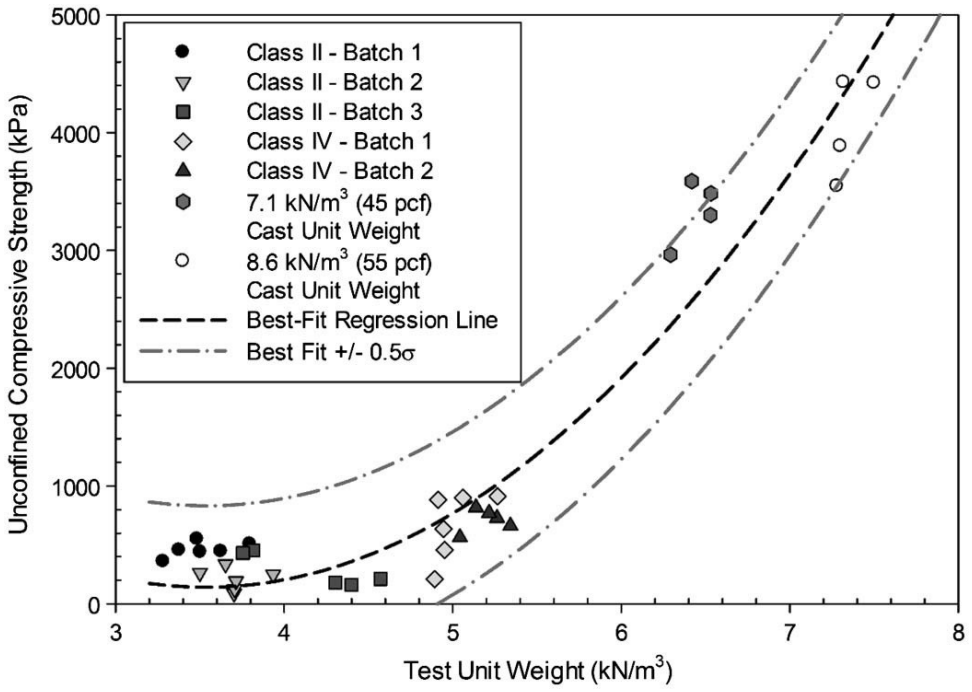

Figure 2-2: Relationship between unconfined compressive strength and test unit weight of LCC specimens (Tiwari et al., 2017)

Caltrans (2014) developed a class system to distinguish between the various densities of cellular concrete. Because the strength of the concrete is correlated with the cast density, estimates of the material properties can be made based on the cast unit weight. Table 2-2 summarizes the Caltrans class system in terms of cast density and minimum compressive strength.

Table 2-2: Caltrans cellular concrete classes

Cellular Concrete Class	Cast Density, pcf (kN/m^3)	Minimum 28-day Compressive Strength, psi (kPa)
I	21-25 (3.30-3.93)	10 (70)
II	25-30 (3.93-4.71)	40 (275)
III	30-36 (4.71-5.66)	80 (550)
IV	36-42 (5.66-6.60)	120 (825)
V	42-50 (6.60-7.85)	160 (1105)
VI	50-80 (7.85-12.57)	300 (2070)

2.4.3 Friction Angle and Cohesion

Several research projects have been carried out to determine the most effective friction angle and cohesion to use in design of cellular concrete. Many of these studies have resulted in a single recommended value for friction angle and cohesion to be used in design. The behavior of cellular concrete samples under various loading conditions has been compared to soil behavior to obtain the design values. Table 2-3 shows several suggested design values.

Table 2-3: Material properties of cellular concrete recommended for design

Author	Suggested Friction Angle, degrees	Suggested Cohesion, psf (kPa)
Deni, Gladstone (2019)	40	0 (0)
Tiwari et al. (2017)	35	0 (0)
Black (2018)	34	700 (33.5)
Remund (2017)	0	3900 (187)
Ni et al. (2018)	47	145 (6.94)

Each of these values has been produced using a different method of evaluating strength. These methods include compressive strength tests, direct shear tests, triaxial tests, and interpretations from passive force tests, among others. Depending on the loading scenario, cellular concrete may behave very differently than it would in another loading scenario.

2.4.4 Shear Strength

Correlations between compressive strength and shear strength are required to determine the shear strength of cellular concrete, as compression tests are typically the only tests carried out on a construction site. A direct shear analysis performed on cellular concrete suggests that the shear strength of the material is approximately 35% of the unconfined compressive strength (Wagstaff, 2016). This value is supported with data from Filz, Reeb, Grenoble, and Abedzadeh

(2015) based on soil-cement mixing tests, which estimates that the shear strength of these materials is approximately 50% of the unconfined compressive strength, with a factor of 0.7 applied for small samples. The strength envelope can be represented by Figure 2-3, given in Filz et al. (2015), with a direct tension strength of 0.12 times the unconfined compressive strength. This envelope assumes a maximum shear strength of 50% of the unconfined compressive strength and a friction angle of 0 degrees.

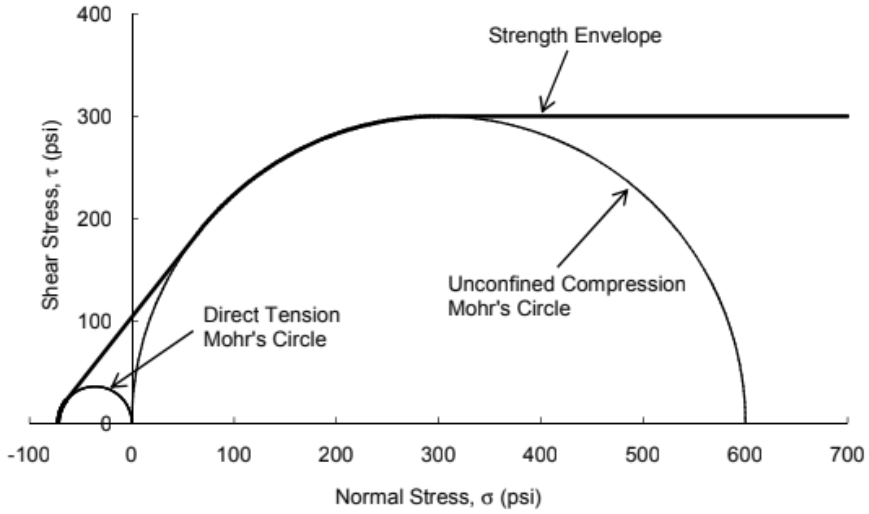

Figure 2-3: Proposed strength envelope for soil-cement mixtures (Filz et al., 2015)

2.4.5 Variations in Density Based on Application

Cellular concrete can be placed at a variety of densities. It is not uncommon to see multiple specified densities or minimum strengths specified for a single project, with lifts consisting of higher-density and higher-strength cellular concrete typically placed below lifts of lighter material. Table 2-4, published by Mohd Sari and Mohammed Sani (2017), suggests various densities of cellular concrete used for various applications.

Table 2-4: Cellular concrete use by density (Mohd Sari & Mohammed Sani, 2017)

Density (kg/m^3)	Application
300-600	Replacement of existing soil, soil stabilization, raft foundation.
500-600	Currently being used to stabilize a redundant, geotechnical rehabilitation and soil settlement. Road construction.
600-800	Widely used in void filling, as an alternative to granular fill. Some such applications include filling of old sewerage pipes, wells, basement and subways.
800 - 900	Primarily used in production of blocks and other non-load bearing building element such as balcony railing, partitions, parapets, etc.
1100-1400	Used in prefabrication and cast-in place wall, either load bearing or non-load bearing and floor screeds.
1100-1500	Housing applications.
1600-1800	Recommended for slabs and other load bearing building element where higher strength required.

Higher-density cellular concrete has higher structural strength but less benefit as a lightweight fill alternative. For this reason, cellular concrete with a density less than 1000 kg/m^3 (60 pcf) is primarily used in geotechnical applications.

2.5 Earth Pressures Based on Geotechnical Theory

Geotechnical theory divides earth pressure into active, passive and at-rest conditions. Active earth pressures develop when a retaining structure moves away from the retained soil, leading to extension in the soil. Passive earth pressures develop when a structure moves into the retained soil, leading to soil compression. At-rest earth pressures develop when there is no lateral movement of the soil or structure. Active and passive earth pressure coefficients, K_a and K_p, respectively, are defined at failure states and can be multiplied by the vertical effective stress to produce the minimum and maximum earth pressures, respectively.

2.5.1 Active Earth Pressure

Active earth pressure for a retaining structure is typically estimated using either the Log-Spiral, Rankine, or Coulomb methods. Research indicates that the log-spiral method is preferred for passive failure cases, but all three methods give approximately the same results for active failure cases (Xu, Lawal, Shamsabadi, & Taciroglu, 2019).

The simplest model of active soil pressure, the Rankine method, ignores friction along the surface of the retaining wall. This assumption is conservative in most cases, making it a preferred design method. The active earth pressure coefficient, K_a, may be determined using Equation 2-1 with level backfill.

$$K_a = \frac{1-sin\phi}{1+sin\phi} \qquad \text{Equation 2-1}$$

If the friction between the soil and wall is considered, the Coulomb active pressure method, modeled by Equation 2-2 for cases with level backfill and a vertical wall face, may be used.

$$K_a = \frac{cos^2\phi'}{\cos(\delta'+\theta)\left[1+\sqrt{\frac{\sin(\delta'+\phi')\sin(\phi')}{\cos(\delta')}}\right]^2} \qquad \text{Equation 2-2}$$

For both methods, the pressure on the retaining structure may be determined using the equation

$$\sigma_h = K_a\gamma z + K_a q - 2c\sqrt{K_a} \qquad \text{Equation 2-3}$$

where γ = material unit weight, z = depth below the top of the fill, q = applied uniform surcharge, and c = material cohesion.

2.5.2 Passive Earth Pressure

Passive earth pressure is determined using the K_p parameter with a similar approach to that used in determining active earth pressure. Prior research indicates that the resistance from passive force in LCC can be closely modeled using a log-spiral approximation with a friction angle of 34º and cohesion of 700 to 1000 psf (Black, 2018). The recommendation made by Tiwari et al. (2017) to ignore cohesion in design has been shown to be overly conservative when designing for passive resistance (Black, 2018). Figure 2-4 shows the comparison between test results and a theoretical PYCAP (Duncan & Mokwa, 2001) analysis using a cohesion of 0.

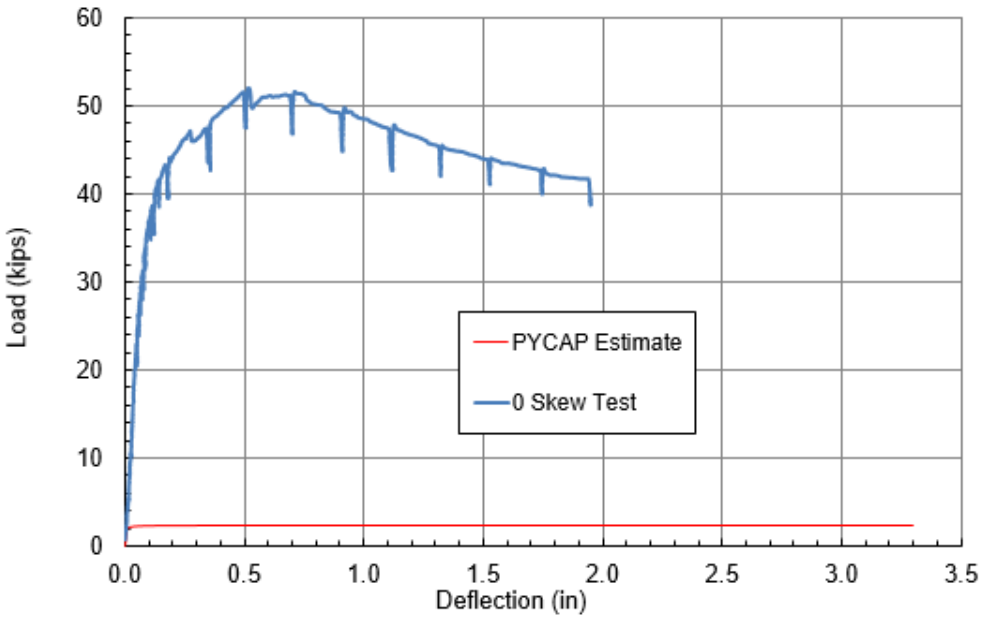

Figure 2-4: Theoretical analysis of the passive force resistance of cellular concrete with no cohesion compared to passive force tests performed on a cellular concrete sample (Black, 2018)

In contrast, the recommendation made by Remund (2017) to design with a friction angle of 0º and a cohesion of 0.35 multiplied by the unconfined compressive strength (UCS) has been shown to be under-conservative for passive pressure. Figure 2-5 shows a PYCAP analysis using this design criteria compared to large-scale passive force test data.

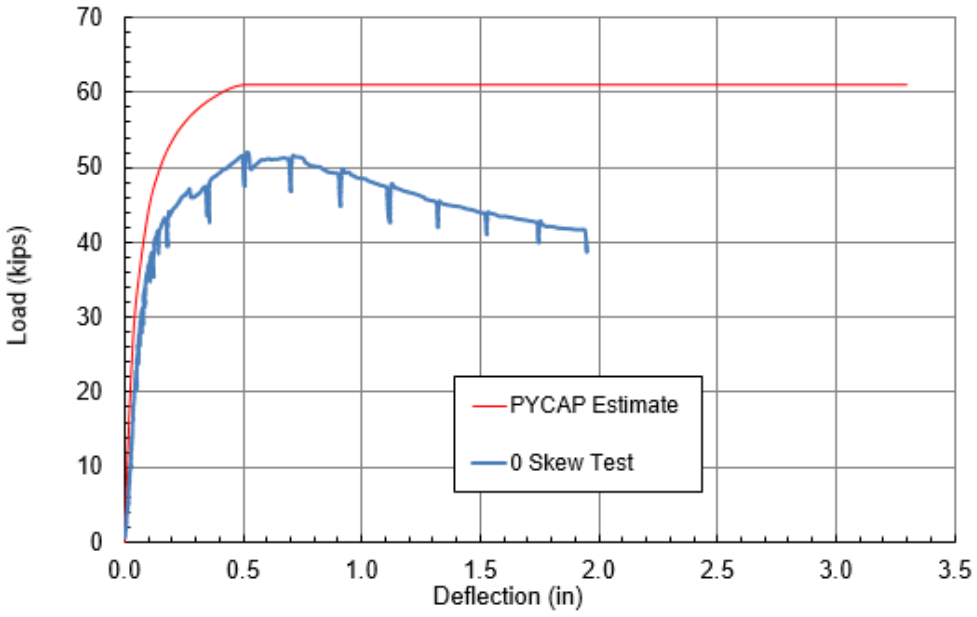

Figure 2-5: Theoretical analysis of the passive force resistance of cellular concrete with a cohesion of 0.35UCS and a friction angle of 0º compared to large-scale test data (Black, 2018)

2.5.3 Nonlinear Variation in Active and Passive Pressures

Coulomb, Rankine, and Log-Spiral analyses of soil are approximations and do not represent the exact behavior of the soil. Chen (2014) theorized that the active earth pressure profile acting on a retaining wall is nonlinear due to soil deformation at failure. A small, progressive deformation in the soil structure can cause the friction angle to change, which results

in a different Coulomb or Rankine earth pressure coefficient. Despite the non-linearity of the active pressure distribution, the Coulomb method still produces results that are approximately accurate (Chen, 2014). In this thesis, a linear analysis model (Rankine's active earth pressure model) will be used, although subsequent research should investigate the potential non-linearity of the pressure distribution within LCC.

Rao, Chen, Zhou, Nimbalkar, and Chiaro (2016) derived new equations to estimate the horizontal active pressure on a retaining structure with frictional and cohesive backfill. The shape of the new pressure curve is approximately linear with depth as anticipated by Rankine's active earth pressure equations but varies from traditional pressure estimations between the bottom of the wall and 20% of the wall height, where the pressure decreases substantially. Figure 2-6 shows the pressure distribution proposed in this research. The range of applicable unit weights and cohesions in this study are limited; therefore, the applicability of these findings to LCC are unknown.

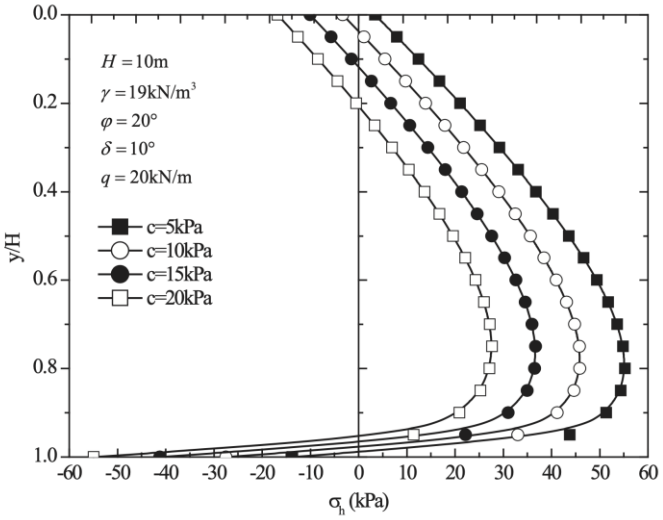

Figure 2-6: Theoretical distribution of horizontal pressure on a retaining structure (Rao et al., 2016)

Other studies support the idea that the pressure distribution on a retaining structure is nonlinear. Figure 2-7, from Matsuzawa and Hazarika (1996) shows the difference in active pressure distribution with various movements from the retaining structure. Each structural failure mode produces a different pressure distribution. In this thesis, the failure mode under consideration is the RB (rotation around base) failure mode, which produces an approximately linear pressure distribution when subjected to only active pressure. The distributions shown in the figure below were developed from tests performed on walls with no applied surcharge.

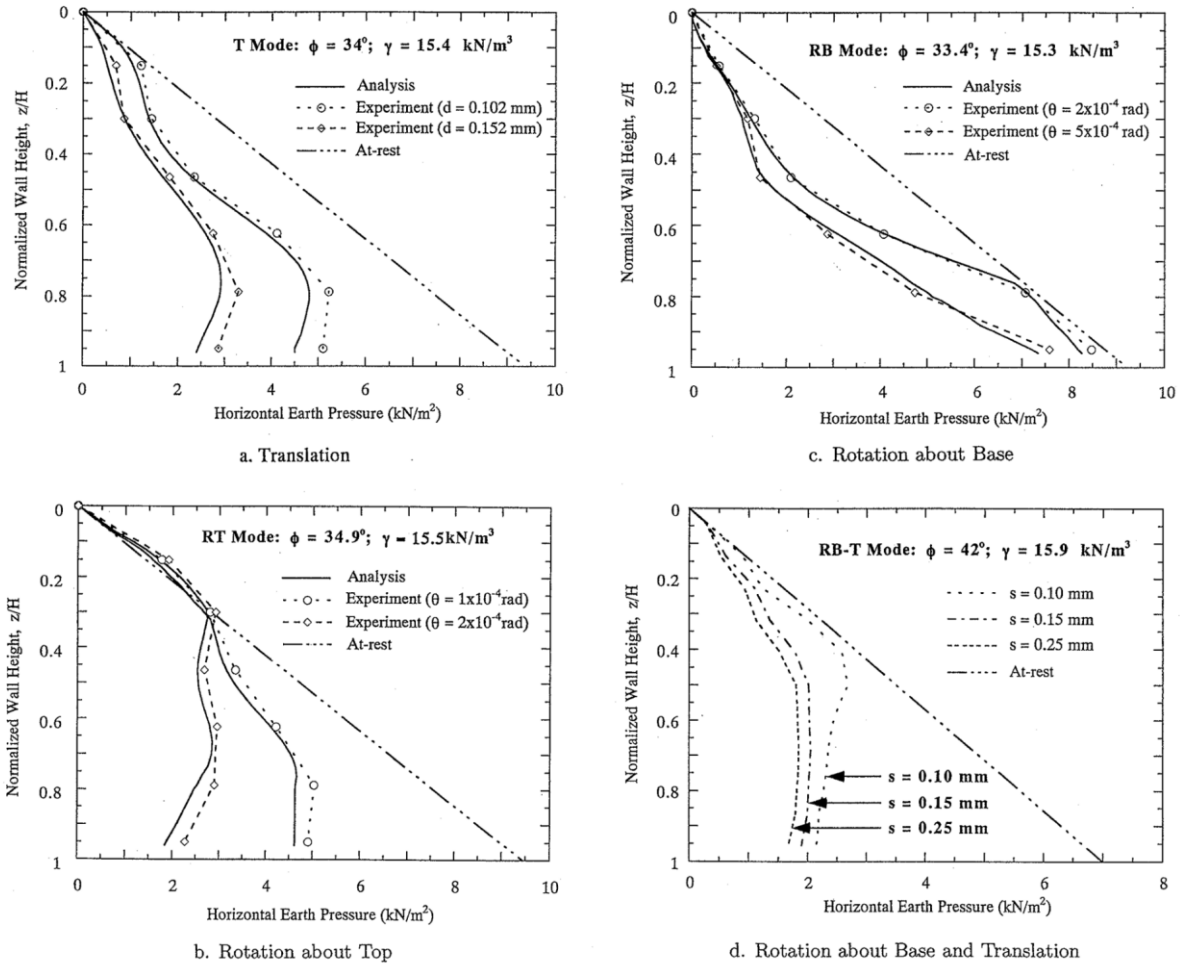

Figure 2-7: Active pressure distribution on retaining structures compared to the at-rest pressure distribution for various failure modes (Matsuzawa & Hazarika, 1996)

2.5.4 Effect of Surcharge on Active Pressure

Surcharge effects on active pressure are usually approximated with a uniform pressure distribution along the height of the retaining wall. From the equation for active pressure (Equation 2-3), the term $K_a q$ represents the effect of the vertical surcharge on the horizontal pressure applied to the wall, which is simply a fraction of the applied surcharge applied uniformly over the surface of the wall. Any surcharge applied outside the zone of active failure is assumed to have no effect on the pressure at the wall face.

Nevertheless, surcharge may produce a more complicated pressure distribution than assumed. Figure 2-8, from Ghanbari and Taheri (2012), shows the results of a numerical model simulation based on the horizontal method of slices. This figure shows that the pressure distribution along the face of a retaining wall from a line surcharge is not linear, and that the effect of the surcharge decreases as the line load gets further from the wall. The highest horizontal pressure is located between 80% and 90% of the wall height in most cases.

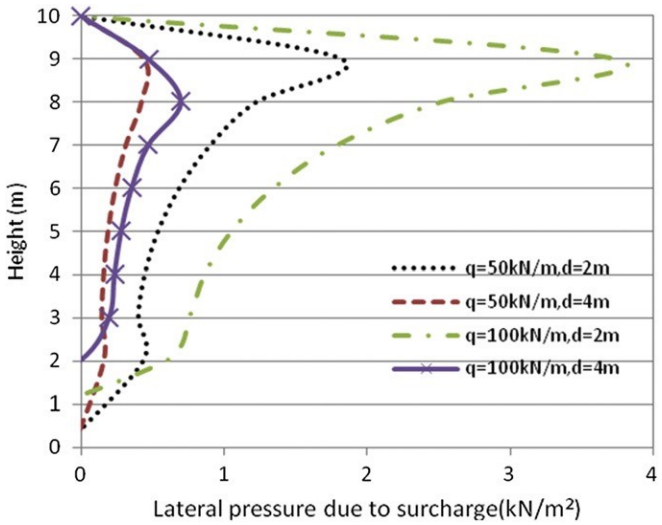

Figure 2-8: Numerical model for line surcharge effects on a retaining structure with varying magnitudes and locations relative to the wall face (Ghanbari & Taheri, 2012)

As the distance from the edge of the line surcharge to the face of the wall decreases, the nonlinearity of the pressure distribution also increases. This pattern is not seen in every soil as it is highly dependent on the soil properties, so the horizontal pressure distribution due to line surcharges applied to cellular concrete is yet unknown. The pressure distribution shown above is not anticipated in this research because the applied surcharge will be an effectively uniform surcharge across the zone of active pressure rather than a strip surcharge; however, the contrast in nonlinearity between Figure 2-6 and Figure 2-8 shows the wide range of possible pressure distributions that are commonly idealized with a uniform pressure distribution.

The distance from a line surcharge to the wall face has little or no effect on the failure angle of the wedge; conversely, the magnitude of the surcharge does affect the failure angle (Ghanbari & Taheri, 2012). This assertion indicates that traditional methods of calculating the effects of surcharge may be flawed. Greco (2005) supports this hypothesis by reasoning that the component of active pressure due to surcharge cannot be represented by the term $K_a q$ because this equation is based on elastic theory. Soil in an active pressure condition must fail, which negates the possibility of using elastic theory to calculate the surcharge effects. Additional studies support the idea that a linear horizontal pressure distribution due to vertical surcharge does not accurately represent the true behavior of soil due to both progressive soil failure and wall movement (Matsuzawa & Hazarika, 1996). However, given the limited amount of test data available for cellular concrete, a simple linear and uniform distribution due to vertical surcharge consistent with standard practice must be assumed. Further research should investigate any nonlinearity of the active pressure distribution within cellular concrete.

In this thesis, the applied surcharge will be approximately uniform across the entire backfill surface within the zone of active failure. It should not be considered as a line surcharge,

but rather a uniform surcharge; thus, the nonlinearity shown in Figure 2-8 is not expected in the test results. The nonlinearity shown in Figure 2-6 is somewhat likely to occur at low surcharge levels in this study, but because the active pressure due to the maximum applied surcharge should far eclipse the active pressure due to the soil weight, the likelihood of such a distribution being seen at moderate or high surcharge levels is reduced.

2.5.5 Design and Analysis Assumptions

Current AASHTO specifications require highway bridges to be designed for a uniform vertical load of 0.64 k/ft (9.34 kN/m) live load per lane, plus a series of point loads modeling truck axles. This loading can be approximated as a uniform surcharge load over a small area using the equation

$$q_{live} = w + \frac{P}{A_t} \qquad \text{Equation 2-4}$$

where w = uniform live load, P = axle point load, and A_t = area of axle influence. Figure 2-9 shows this design loading with no reduction factors applied.

For a standard tandem-axle truck, the approximated q_{live} load would be approximately 1625 psf (77.8 kPa), assuming a total axle width of 8'-0". Design consideration must also be given to the self-weight of the embankment or construction loads that may occur (Deni & Gladstone, 2019). A tall cellular concrete embankment supporting construction loads may have an effective applied surcharge exceeding 3000 psf (144 kPa) at the base of the embankment.

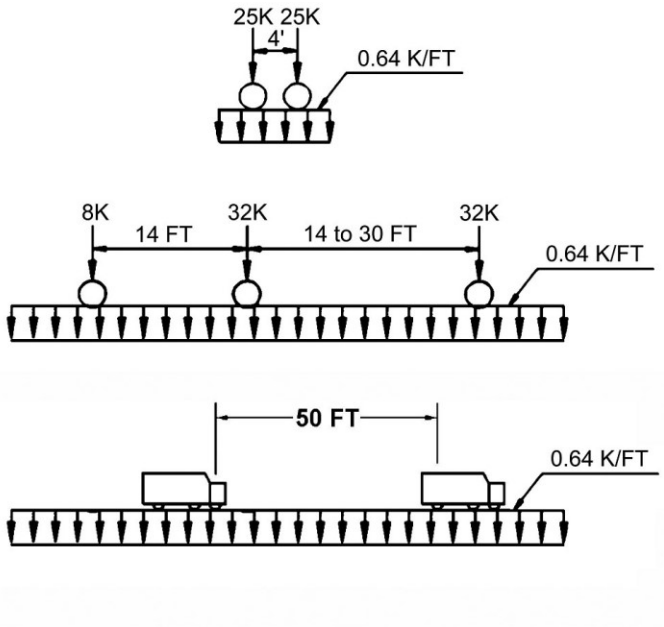

Figure 2-9: AASHTO bridge and highway design loads

A 150 ft (45.7 m) MSE wall with granular backfill was built as part of the Seattle-Tacoma International Airport expansion project. This required extensive reinforcement, ground improvement, and compaction, but its performance has been very good (Stuedlein, Bailey, Lindquist, Sankey, & Neely, 2010). If the compacted earth behind this MSE wall were replaced with 30 pcf (4.7 kN/m^3) cellular concrete, the vertical stress at the bottom would be approximately 4500 psf (215.5 kPa). This is significantly larger than the design vehicle live load alone.

2.5.6 Analysis of Friction Angle

Traditional Coulomb and Rankine design methods use the internal friction angle of the soil to determine static or active earth pressures. This friction angle can be determined through laboratory tests including the direct simple shear and triaxial tests. Studies comparing the

laboratory-measured internal friction angle of a soil with the friction angle after active failure suggest that the friction angle to be used in design should be decreased slightly to account for the progressive failure of the soil (Frydman & Keissar, 1987). For cohesionless soils, Chen (2014) concluded that the friction angle of the soil must be adjusted to account for the failure mechanisms of the soil. Though the behavior of cellular concrete in various failure modes is relatively unknown, some variation between the laboratory-measured friction angle and the tested friction angle can be expected.

2.6 Behavior Under Confined Conditions

Cellular concrete behaves very differently in a confined state than it does when unconfined. Compressing the material, regardless of the environment, causes micro-cracks within the cellular structure. In an unconfined state, these cracks propagate and join together to create larger cracks, ultimately leading to the failure of the material (Rahman et al., 2010). When the material is confined, the micro-cracks cannot propagate as effectively, leading to a different failure mechanism. Research also suggests that internal reinforcing with geo-grids can limit crack propagation in a similar way (Tiwari, Ajmera, & Villegas, 2018). Figure 2-10 shows the shape of the stress-strain curve for a confined test, while Figure 2-11 shows a typical stress-strain curve for unconfined cellular concrete based on data obtained from preliminary tests performed for this project.

Three regions have been defined to approximate the behavior of cellular concrete in a confined condition. The first, the elastic region, represents the steep portion at the beginning of the curve. This behavior is seen in both confined and unconfined samples. The next regions, plateau and densification, occur only for confined tests (see Figure 2-10) while a rapid increase in strain with no gain in stress is seen in unconfined tests (see Figure 2-11). Though both the

confined and unconfined tests show similar compressive strengths through the end of the elastic region (Abdul Rahman, Ahmad Zaidi, & Abdul Rahman, 2010), the ductile failure makes a confined condition ideal if the material is to be stressed near its maximum compressive strength (Rahman et al., 2010).

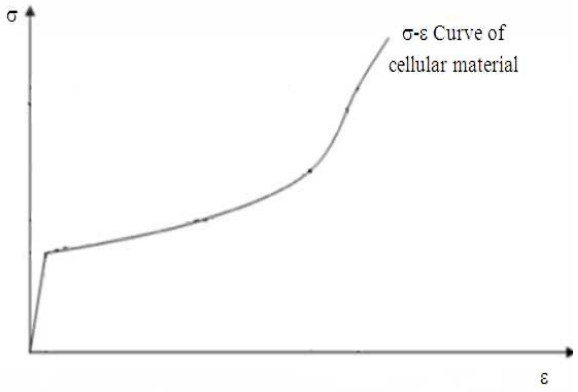

Figure 2-10: Stress-strain curve for confined cellular concrete (Abdul Rahman et al., 2010)

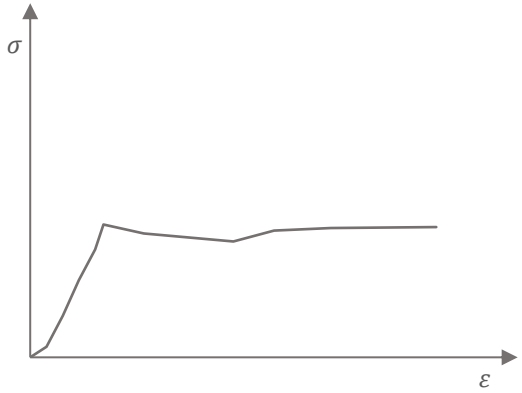

Figure 2-11: Stress-strain curve for unconfined cellular concrete

This research project focuses on the behavior of the cellular concrete after shear failure due to axial force rather than pure compression failure. The discussion of cellular concrete behavior in confined conditions serves to illustrate the possibility of a ductile material failure. Unconfined testing has shown that cellular concrete exhibits a relatively ductile failure when the entire surface area is stressed, but as the material becomes stiffer, the failure becomes more brittle. Figure 2-12 shows the stress-strain plot for a series of 4-cylinder samples after a 28-day cure time. Each of these cylinders experienced a sudden loss of strength after reaching their ultimate compressive strengths. This is not ideal behavior because the cellular concrete may fail catastrophically once a certain loading is achieved.

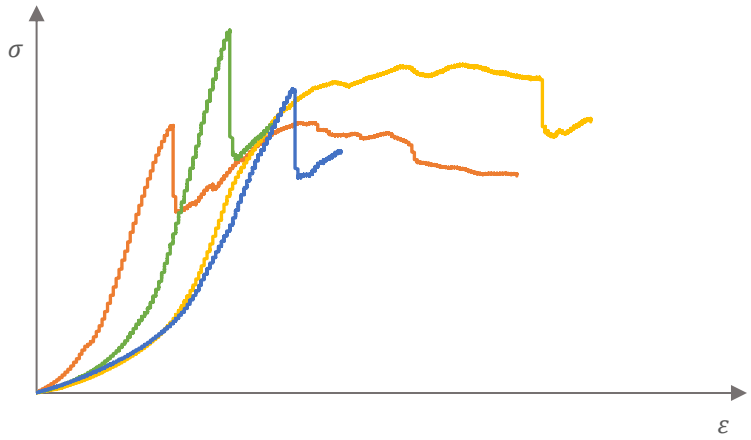

Figure 2-12: Stress-strain curves for 4 sample cylinders after 28-day cure

Preliminary testing indicates that LCC fails in a more brittle manner after 28 days of cure time than it does after 7 days. Testing also indicates that LCC with lower compressive strength also fails in a more ductile manner than LCC with a higher compressive strength after the same cure time. If a retaining structure is designed and constructed such that it can provide enough

confinement to make the stress-strain behavior of the LCC closer to that of the confined test, the risk of catastrophic failure may be minimized. A ductile failure is desirable to prevent loss-of-life in the event that the extreme compressive stress of the material is reached.

2.7 Summary

Cellular concrete is becoming increasingly popular in construction projects as a road base, a ground improvement measure, and as a lightweight fill alternative. Its self-leveling and self-consolidating properties make it a cost-effective alternative to other lightweight fills when labor costs are high.

Various laboratory tests have been performed on cellular concrete samples to determine correlations between unconfined compressive strength, density, shear strength, cohesion, and friction angle. Tests have also been performed to approximate its behavior under passive stress with a friction angle and a cohesion. These laboratory tests indicate that cellular concrete behaves more like a soil than traditional Portland cement concrete, but its behavior under active pressure loading conditions is still unknown.

Uncertainty still exists as to whether cellular concrete acts as a self-supporting material or as a cohesive soil behind a retaining structure. It is self-supporting under its own weight, but external pressures and forces may cause it to behave differently than anticipated. Recommendations have been made to design retaining walls as if the cellular concrete backfill has a friction angle of 35º and no cohesion as a conservative estimate. Passive pressure analysis has shown that this may be over-conservative, but active pressure tests are required to confirm the estimated behavior.

The effect of surcharge on the horizontal pressure exerted on a retaining wall is also unknown. The nonlinear nature of the surcharge load makes it difficult to predict the pressure distribution on the wall. A linear and uniform distribution must be assumed until further research shows otherwise.

3 TEST LAYOUT, INSTRUMENTATION, AND PROCEDURES

3.1 Overview

Two large-scale tests were performed on a block of cellular concrete 10’ wide, 12’ long and 10’ tall. This test was designed to be significantly larger than previous tests performed on samples in a laboratory setting to more closely model the true behavior of cellular concrete backfill in real-world settings. Secondary tests, such as direct shear and unconfined compression tests, were performed in the laboratory to correlate the material properties with previous research data. All large-scale tests were performed in the structures lab at Brigham Young University (BYU). Lab tests on material samples were performed by lab personnel at BYU and by the materials testing staff at Gerhart Cole in Salt Lake City.

3.2 Direct Shear Testing Layout and Procedures

Because LCC is usually not placed in lifts higher than 40” due to potential material instability, several lifts were required to construct the block used in the large-scale tests. Direct shear tests were performed to ensure that the bond between lifts had sufficient strength to withstand the development of a shear plane and not skew the results of the tests.

Three split boxes measuring 12” x 12” were filled halfway with LCC. After a curing period of 24 hours, a second lift was added to each split box. The cold joint between lifts was positioned such that the shear plane would develop at the joint rather than within one of the lifts.

Each direct shear test was performed at a strain rate of 1% per minute. Hydraulic jacks were used to apply normal force to the top and shear force to the side of the split box, while the bottom of each split box was restrained against a reaction frame. The boxes were stressed at 8, 12, and 16 psi (55, 83, and 110 kPa) of normal force. The tests were carried out after a curing time of 6 days and 7 days for the top and bottom lifts, respectively.

One direct shear test was performed with the split box filled with a single lift of cellular concrete. This box was stressed with a normal force of 12 psi (83 kPa) and tested in the same manner as the other boxes. This test was performed to correlate the material used in the other direct shear tests with previous tests done by Black (2018) and Remund (2017).

3.3 Large-Scale Testing Overview

3.3.1 Frame Design

A test box 10 ft tall x 12 ft long x 10 ft wide was constructed in the structures laboratory at BYU to perform the test. The box was designed to minimize lateral movement of the cellular concrete block on three vertical faces but allow lateral movement of a Reinforced Concrete Cantilever (RCC) wall on the fourth side as a vertical surcharge was applied to the top surface of the cellular concrete. Limited movement on three sides of the box encourages a plane-strain condition.

The size of the box was determined based on laboratory space constraints and compatibility requirements for future tests performed at BYU. Future tests using Mechanically Stabilized Earth (MSE) walls in place of the RCC wall used in this test required the dimensions of the test box to be compatible with the 5 ft x 5 ft precast MSE wall panels. The width and height of the box were determined to each be 10 ft to ensure compatibility with future tests. The

length of the box (12 ft) was determined based on laboratory constraints, as anchor points in the structural floor were located at 3 ft intervals.

A steel reaction frame was incorporated into the design of the box to apply a maximum surcharge of 1,000 kips distributed evenly across the surface of the cellular concrete during a uniform load test, or a total force of 625 kips distributed across half the surface of the cellular concrete during a partial load test. The different loading procedures will be presented in a later section. This steel frame was constructed using various steel shapes as beams, columns, diagonal braces, and connection plates.

A series of six hydraulic jacks were mounted to a double W30x191 reaction beam spanning across the top of the frame to provide a vertical surcharge load to the surface of the cellular concrete. Six reinforced concrete beams with steel bearing plates were placed below the jacks to transfer the load from the hydraulics to the cellular concrete surface. Each concrete beam was 2 ft wide x 10 ft long x 16” deep. The beams were designed to transfer a maximum surcharge load of 200 kips each with a deflection of less than 0.25”. The surcharge beams were intended to produce a uniform surcharge pressure while allowing independent settlement across the LCC surface because the failure mode was not known in advance.

Horizontal beams spaced at 30” on center were added to 3 sides of the steel frame to contain the horizontal pressure generated as the LCC was compressed. Wood wall panels were placed inside the framework to provide a flat surface both to contain the LCC and to transfer the horizontal pressure to the steel beams. The walls were constructed of 2x4 studs with ¾” oriented strand board on the inside face. Shims were placed between the wood walls and the steel beams as needed to ensure that they sat flush inside the frame.

I performed the design and analysis of the test box and steel reaction frame using SAP2000 computer software. I designed the frame to minimize total costs by using steel beams and columns previously used in research at BYU. The existing columns and beams included a variety of steel shapes, including W, HP, C, and MC shapes, along with various sizes and strengths of steel rods. I designed each beam connection by hand and provided shop drawings to the BYU Precision Machining Laboratory, which manufactured all the steel plates and connections required for the frame. I also designed the cantilevered retaining wall, the wood wall panels, the horizontal bracing for all the wall panels, the anchorage between the reaction frame columns and the structural floor, and the bearing plates and concrete beams that transferred load from the hydraulic jacks to the LCC surface. Using the original structural drawings for the BYU Clyde Engineering Building, I also performed an analysis of the strength of the structural 2-way concrete floor in the structures laboratory to ensure the uplift from the reaction frame, combined with the downforce from the hydraulic jacks, would not cause a structural failure of the floor or the basement walls supporting the floor. The design of the testing apparatus was ultimately limited by the strength of the frame columns, which were subjected to tension, torsion, strong-axis moment, and weak-axis moment concurrently throughout the test.

Assuming a Poisson's ratio of 0.25 as suggested by Tiwari et al. (2017), and a total vertical deflection of 3", the anticipated horizontal expansion of the LCC under unconfined conditions would be approximately 0.75". To more closely resemble a plane strain condition, the total deflection of the steel frame was limited to 0.1" at any point on the side walls. The deflection of the wood walls was also limited to 0.1", but some settlement was expected at the beginning of the test as the walls pressed evenly against the steel beams. Because the horizontal deflection expected inside the frame was much smaller than the anticipated unconfined

horizontal deflection, the assumption was made that the horizontal expansion against the steel frame was negligible and the LCC behaved as it would in a fully confined state. Figure 3-1 through Figure 3-5 show the design and construction of the steel reaction frame.

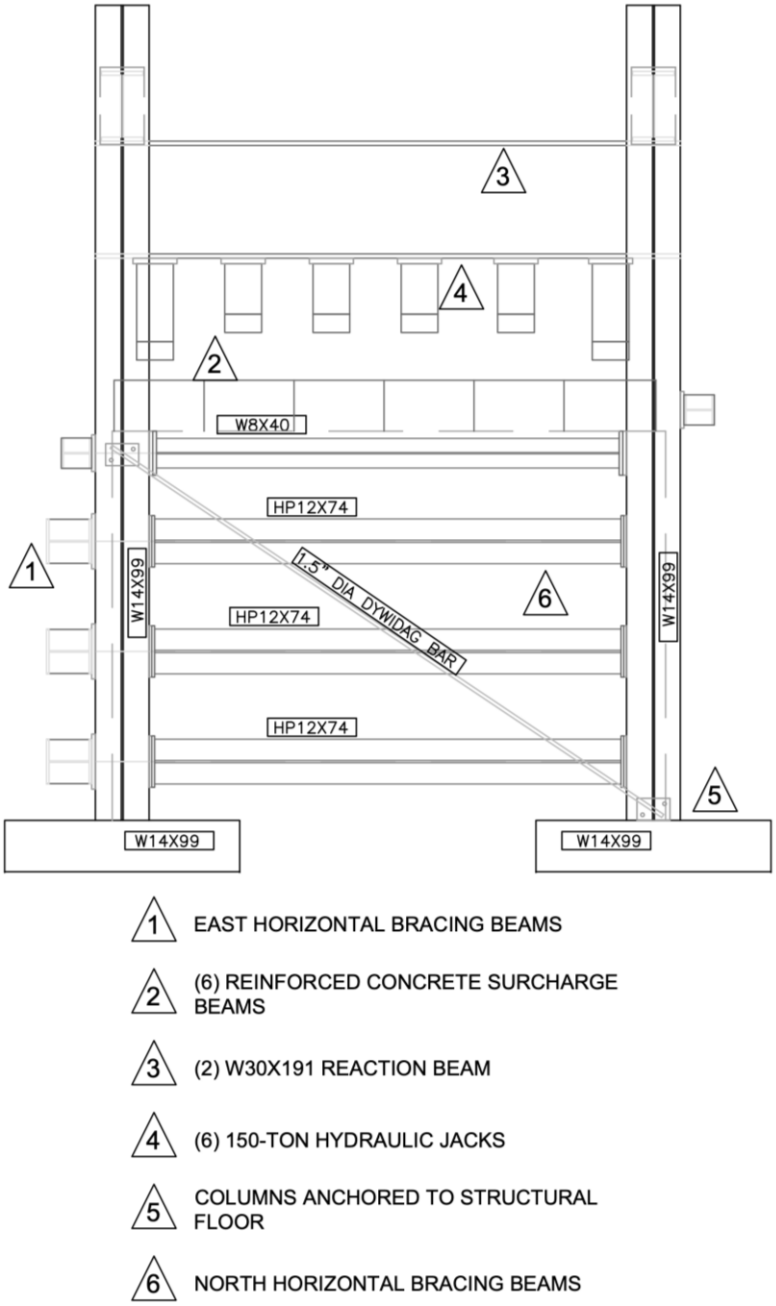

Figure 3-1: Steel reaction frame design – North elevation view (South similar)

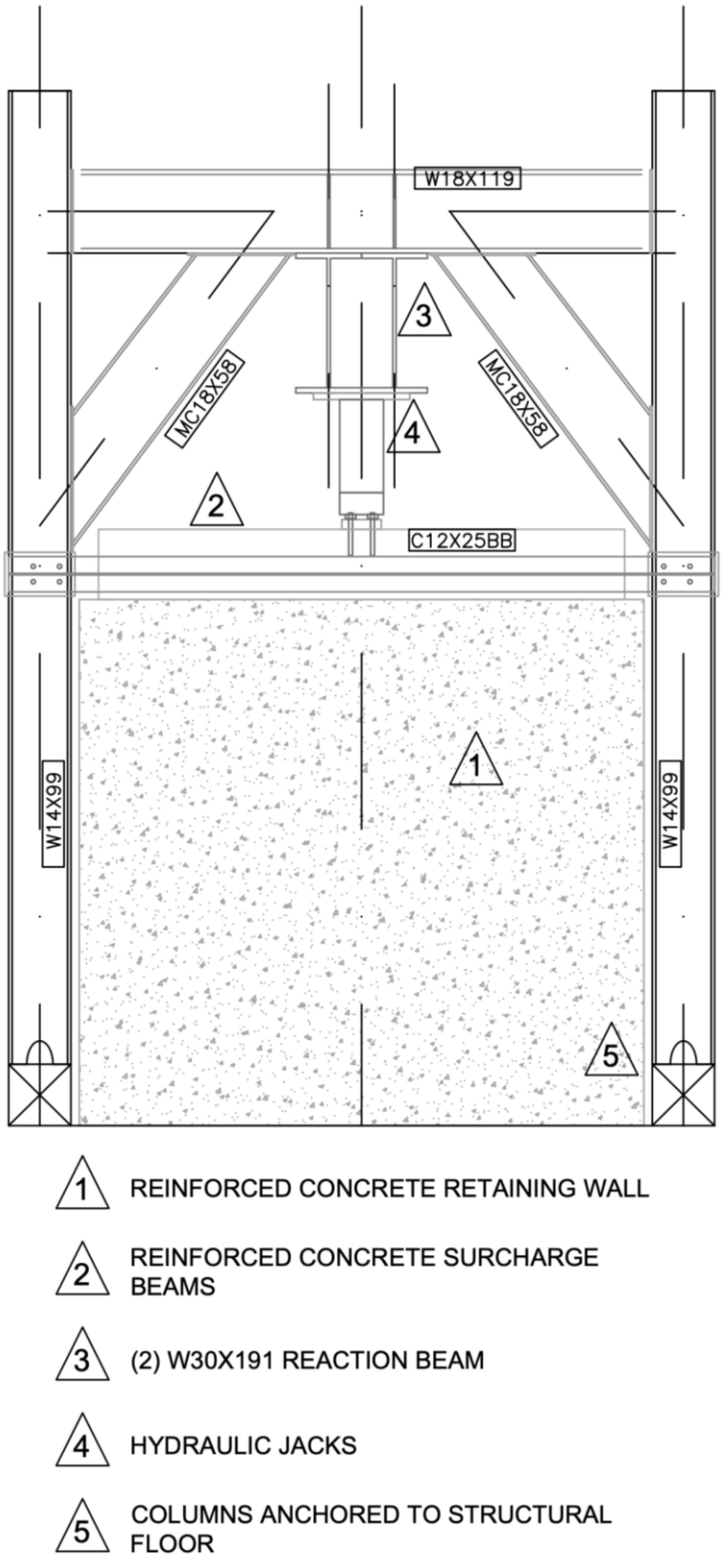

Figure 3-2: Steel reaction frame design – West elevation view

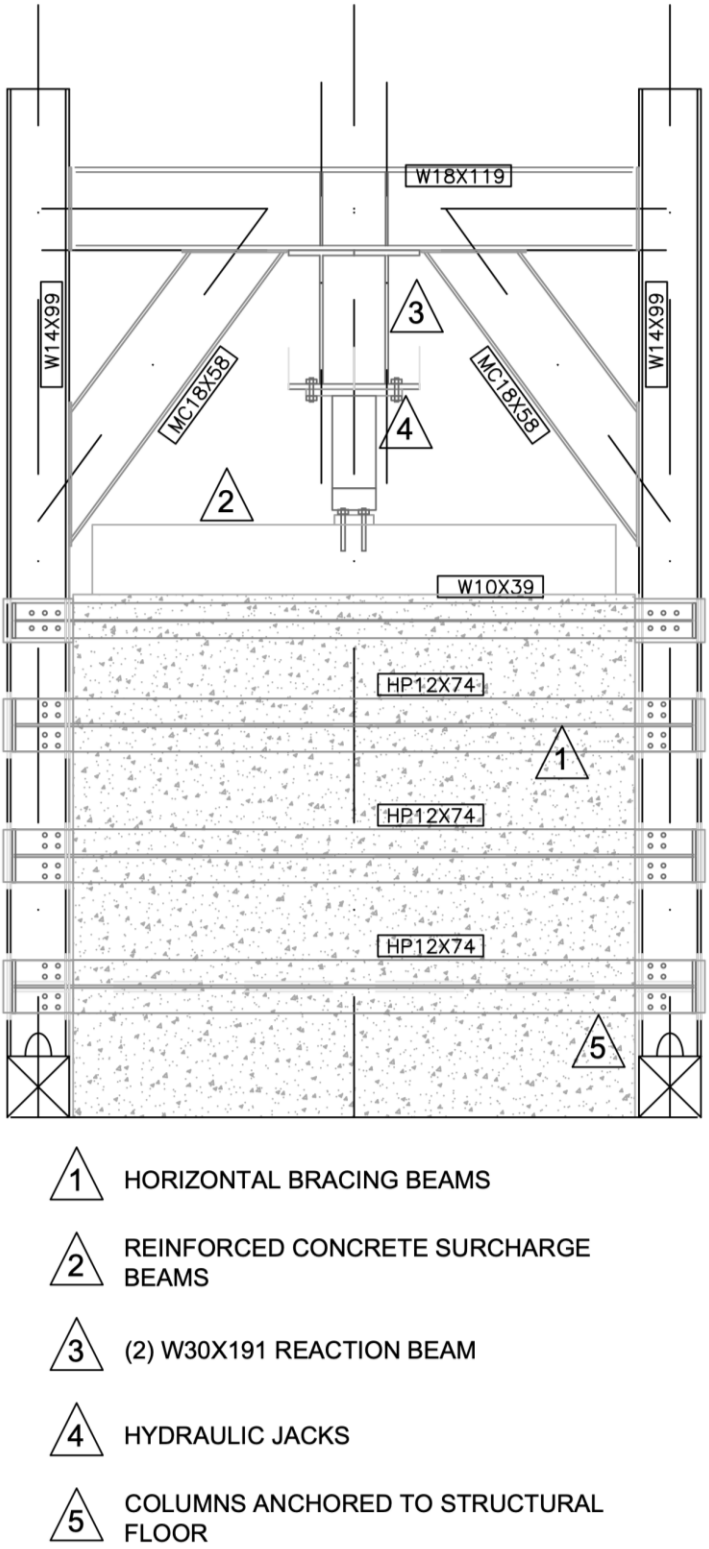

Figure 3-3: Steel reaction frame design – East elevation view

Figure 3-4: Completed steel reaction frame (East elevation view)

Figure 3-5: Wood panels inside the steel reaction frame

Prior to filling the box with cellular concrete, seams between walls and along the floor were sealed with a foam sealant, and the walls and floor were covered with plastic sheeting. A total of three layers of plastic, with molybdenum grease between each layer, were applied to each wall. The grease and plastic layers were designed to create a low-friction interface between the wall surface and the LCC block. This would allow the LCC to settle more uniformly under the surcharge pressure and to deform more uniformly in the direction of the RCC wall without influencing the failure of the LCC block. Plastic was on the outermost surface of the wall; the cellular concrete was not in contact with the grease at any point, avoiding potential

contamination. The RCC retaining wall and footing, with embedded pressure plates, were left exposed to the LCC backfill to model the wall-LCC interaction. Figure 3-6 shows the inside of the box prior to pouring.

Figure 3-6: Top view of the test box prior to filling

3.3.2 Retaining Wall Design

A concrete cantilevered retaining wall was designed using design criteria suggested by Tiwari et al. (2017) and Black (2018). The horizontal pressure anticipated on the wall was calculated using the equations

$$\sigma_h = K_a \gamma z + q K_a - 2c\sqrt{K_a}$$ Equation 3-1

$$K_a = \tan^2\left(45 - \frac{\emptyset}{2}\right)$$ Equation 3-2

where γ=30psf, z=depth below LCC surface, and q=surcharge pressure applied. A vertical surcharge of 8640 psf (415 kPa) was determined to be the upper threshold for this test. Cohesion estimates between 700 and 1000 psf (Black) and 700 and 1600 psf (Tiwari, Ajmera et al.) were used to compute anticipated horizontal pressures on the wall. Table 3-1 contains the calculated anticipated σ_h values at the total surcharge of 8640 psf.

Table 3-1: Anticipated horizontal pressure for various cohesion estimates

Cohesion psf (kPa)	Anticipated σ_h psf (kPa)
0 (0)	2380 (114)
700 (33.5)	1650 (79)
1000 (47.9)	1340 (64.2)
1600 (76.6)	710 (34)

Active pressure development requires some movement of the retaining wall. Retaining walls usually allow active pressure to develop through slight compression of the soil beneath the toe of the wall, which causes the top of the wall to deflect. Other modes of wall displacement include sliding, rotation around the top, and a combination of rotation and sliding.

Because the floor of the laboratory (a structural concrete slab) is essentially rigid, the wall could not rotate about its base by compressing the bearing surface like a wall constructed on soil might. To ensure the wall would deflect a small amount and active pressure would develop, the reinforcing steel inside the wall stem was designed to reach its yield point partway through

the test and create a rotational effect. The wall was designed to resist a maximum uniform horizontal pressure of 4.93 psi (34.0 kPa). Table 3-2 shows the anticipated surcharge pressures required to stress the reinforcement in the retaining wall to its yield point. These values were calculated using LRFD reinforced concrete design methodology with a strength reduction factor (phi) of 0.9.

Table 3-2: Estimated surcharge to produce wall yield for various cohesion estimates

Cohesion psf (kPa)	Surcharge at Yield psf (kPa)
0 (0)	2450 (117.3)
700 (33.5)	5150 (246.6)
1000 (47.9)	6300 (301.6)
1600 (76.6)	8600 (411.8)

The retaining wall footing was designed to have a large heel to prevent the wall from overturning at the base. Wood blocks were placed between the footing toe and an independent reaction frame to prevent sliding failure. As previously noted, restricting the wall from rotating about the top or sliding at the base is critical to assuming an approximately linear soil pressure distribution (Matsuzawa & Hazarika, 1996).

To level and square the retaining wall, the wall was lifted with an overhead crane and gypsum cement was poured around and under the footing. The total thickness of the gypsum cement beneath the footing was 3”. The compressive strength of the gypsum, approximately 5,000 psi, was similar in strength to the 4,000 psi concrete used in the retaining wall construction. Figure 3-7 shows the retaining wall design parameters.

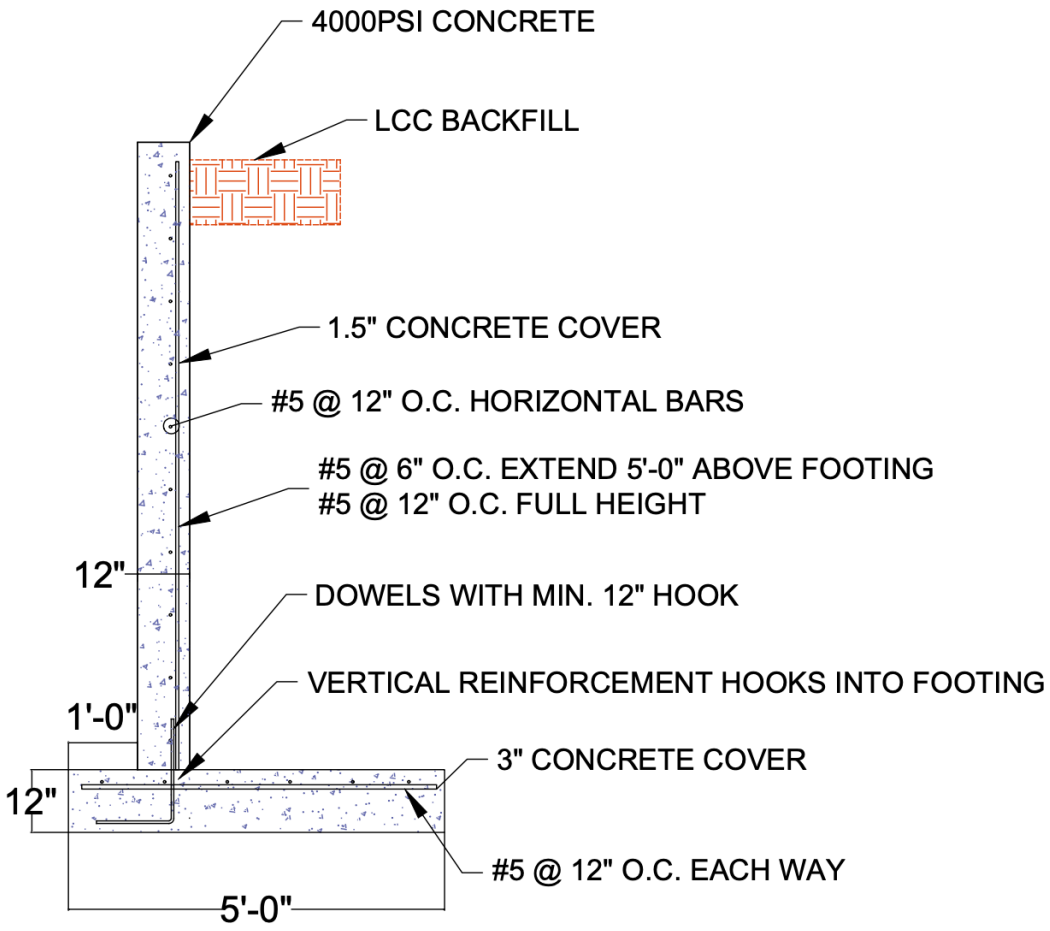

Figure 3-7: Reinforced concrete cantilever retaining wall design

3.3.3 Reinforced Concrete Cantilever (RCC) or Retained-Face Test Layout

Two different configurations were used in the RCC wall tests. A uniform surcharge was applied to the entire surface of the LCC block in the first test, while a uniform surcharge was applied to one-half of the surface adjacent to the RCC wall during the second test.

3.3.3.1 Uniform Surcharge Layout

The first configuration, uniform surcharge across the entire surface, was used in a preliminary test in January 2020. The layout of the test is presented in Figure 3-8. This loading

sequence places the entire LCC backfill in uniform compression throughout the test. The results of this preliminary test are presented in Chapter 4.

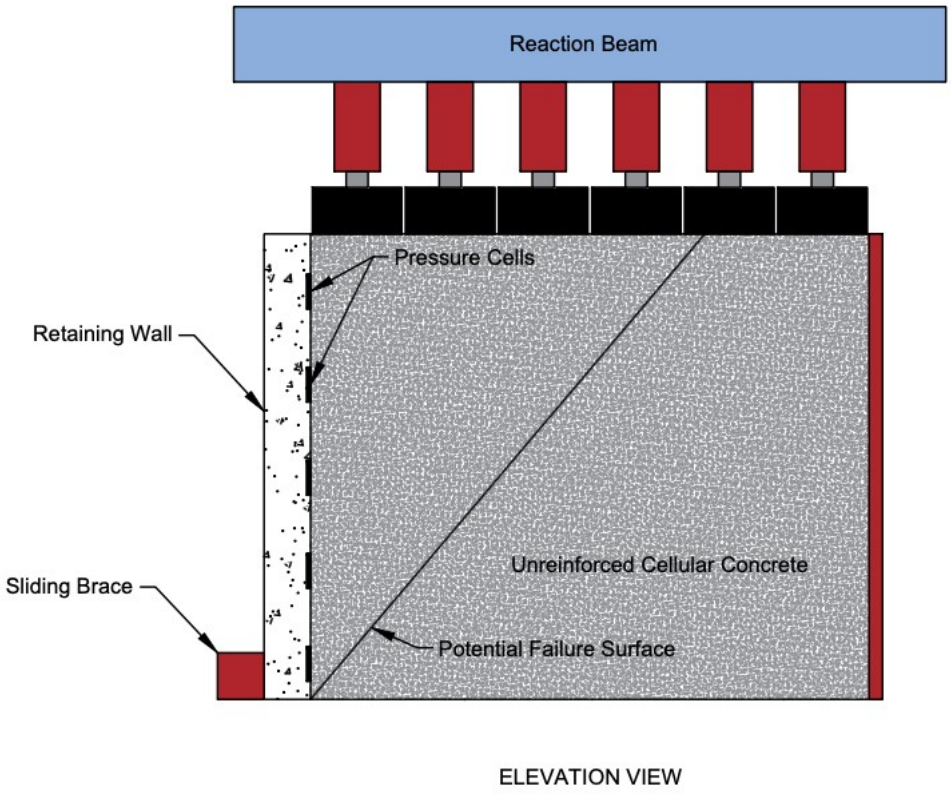

Figure 3-8: Uniform surcharge layout diagram – elevation view

3.3.3.2 Partial Surcharge Layout

RCC walls may also be subjected to surcharge loadings of limited width behind the wall. These loadings have the potential to induce both compressive and shear stresses in the LCC which may represent a more critical loading case. To better simulate the development of a potential shear plane, only half the surface of the LCC was loaded with a uniform surcharge

during the second test. The surcharge was applied using only three of the concrete surcharge beams, extending six feet behind the wall as shown in Figure 3-9.

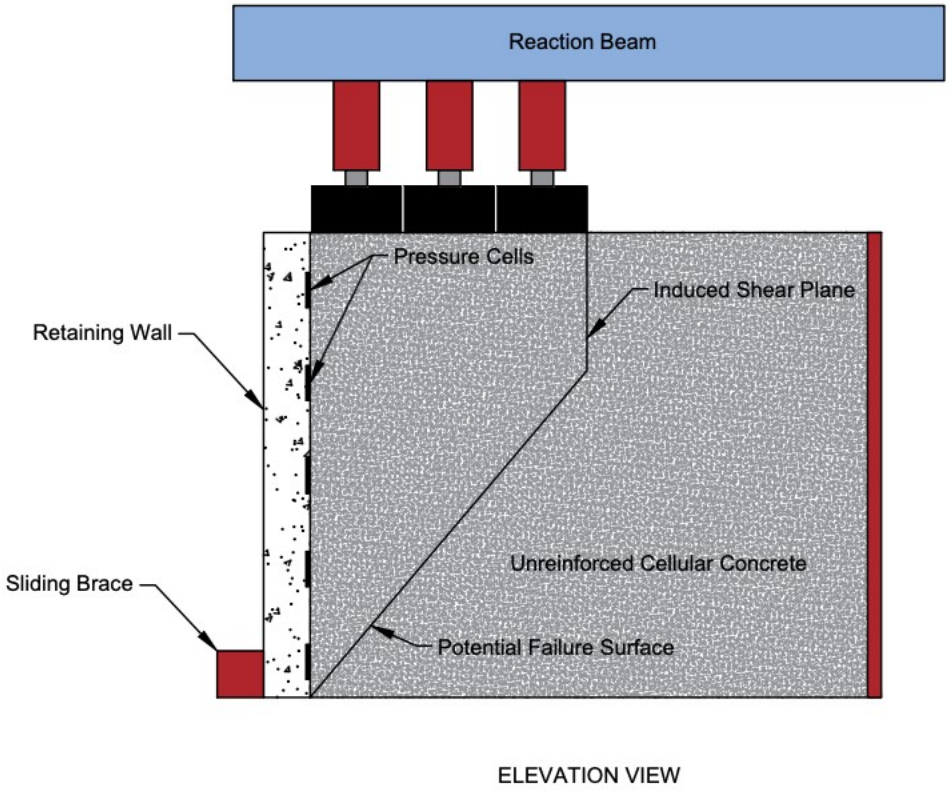

Figure 3-9: Partial surcharge layout diagram – elevation view

3.3.4 Free-Face Test Layout

After the RCC or retained-face test was carried out, the East wall of the frame (opposite the retaining wall) was removed and a free-face test was performed. A uniform surcharge was applied to the three surcharge beams (6 ft by 10 ft area) on the other half of the LCC surface and incrementally increased until the LCC failed. Figure 3-10 shows the loading diagram for this test.

The free-face test was performed within 48 hours of the retained-face test so the material strengths were as similar as possible. By performing both tests on the same material, comparisons between failure in retained and free-face conditions can be made, and the relative merits of a retaining structure can be determined.

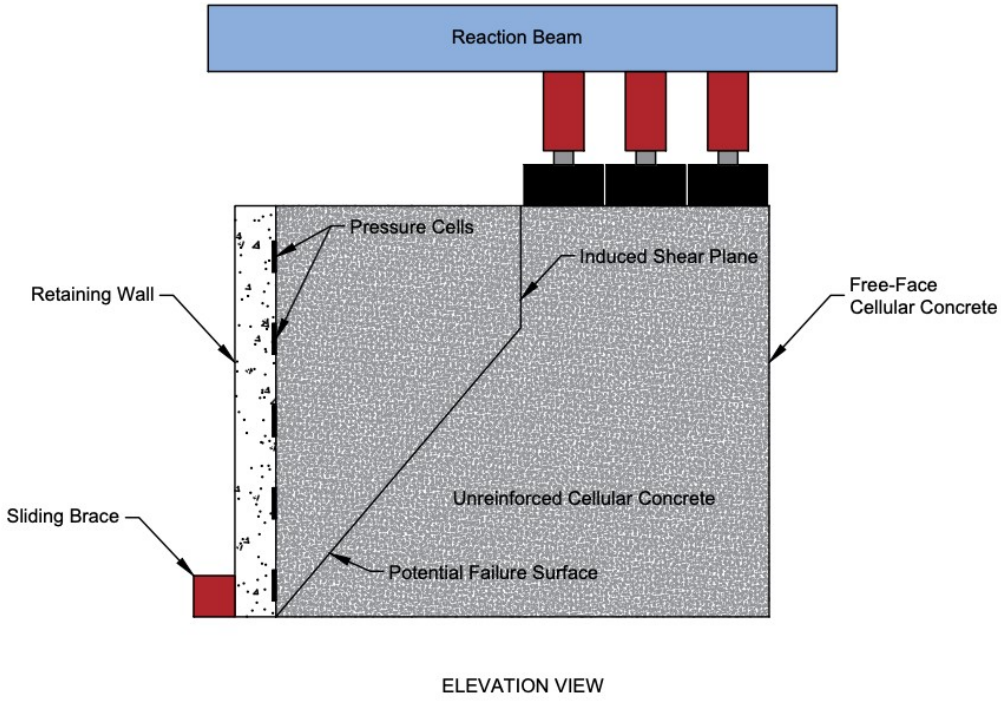

Figure 3-10: Free-face surcharge layout diagram – elevation view

3.4 Large-Scale Test Instrumentation

3.4.1 RCC or Retained-Face Test Instrumentation

Instrumentation for the retained-face test consisted of string potentiometers, embedded pressure sensors, external pressure sensors, thermal couples, and load cells. Readings were taken

throughout all the tests at a rate of 5 samples per second. Thermal couples and an accelerometer were also used during the pours and curing to monitor any external temperature changes or vibrations that might adversely affect the curing process. All readings were recorded in CSV format and manually analyzed after the test was completed.

3.4.1.1 Vertical Surcharge

Load cells were located inside a circular steel pocket beneath each hydraulic jack to measure the total force applied to each concrete beam. Hemispherical bearing platens were placed below the load cell to produce a vertical load and prevent damage to the hydraulics should the beams experience uneven settlement during the loading process. Figure 3-11 shows the configuration of the load cells, hemispherical platens, and hydraulic jacks above the concrete surcharge beams. Steel beams and/or stacked plates were use as spacers to allow the jacks to contact the beams early in the stroke length.

Figure 3-11: Hydraulic jacks, hemispherical platens, and load cells mounted to steel reaction beams and concrete surcharge beams.

3.4.1.2 Horizontal Pressure

Six Geokon® Model 4810 “Fat Back” pressure plates were embedded flush with the interior face of the retaining face of the retaining wall. These pressure plates were left exposed to the surface of the LCC to ensure that a representative contact surface was made at the interface.

Additional pressure pads were placed on the surface of the retaining wall as a supplemental measurement system. The pads were sealed against water, but due to the extremely long initial set time of the LCC, they still experienced water damage. Some of the pads dried out before the full test was performed and yielded some data, but many did not function properly. Data obtained from these pads was used sparingly in the analysis due to the sporadic functionality and overall inconsistency of the sensors. Figure 3-12 shows the layout of the pressure pads and embedded pressure plates on the face of the retaining wall.

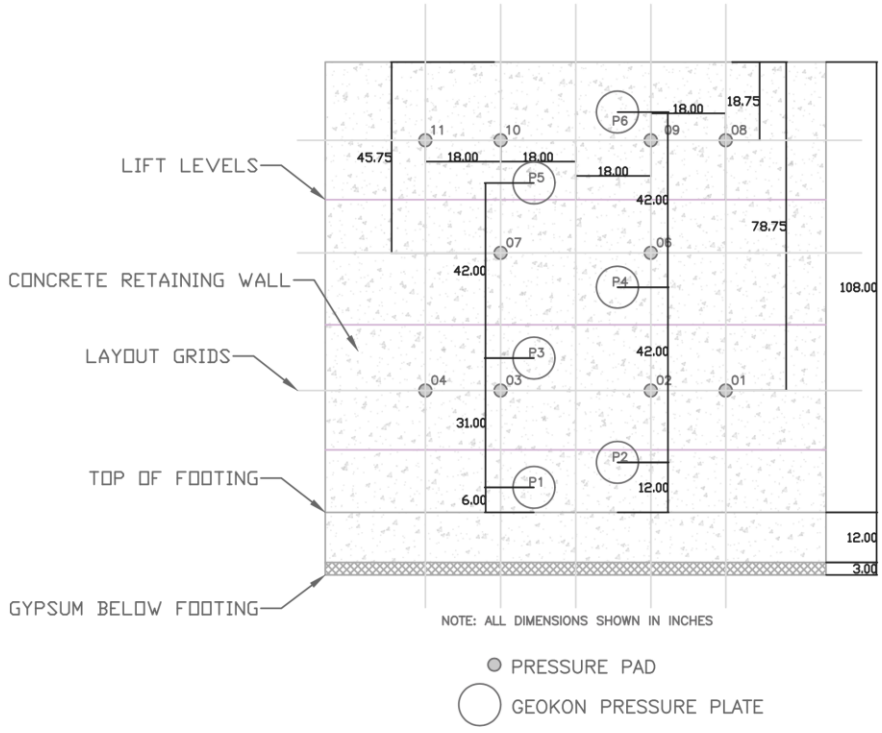

Figure 3-12: Retaining wall instrumentation layout – elevation view

3.4.1.3 Frame Deflection

A series of string potentiometers were placed on the beams and columns around the frame to monitor deflection. Anticipated deflections for each beam and column were determined using the SAP2000 frame model. Throughout the test, the actual deflections were compared to the anticipated deflections to determine if the frame was behaving as expected. String potentiometers were also placed on the wood walls surrounding the LCC to measure horizontal expansion. Figure 3-13 shows the layout of the potentiometers on the North side of the reaction frame. Similar instrumentation was placed on the South side of the frame.

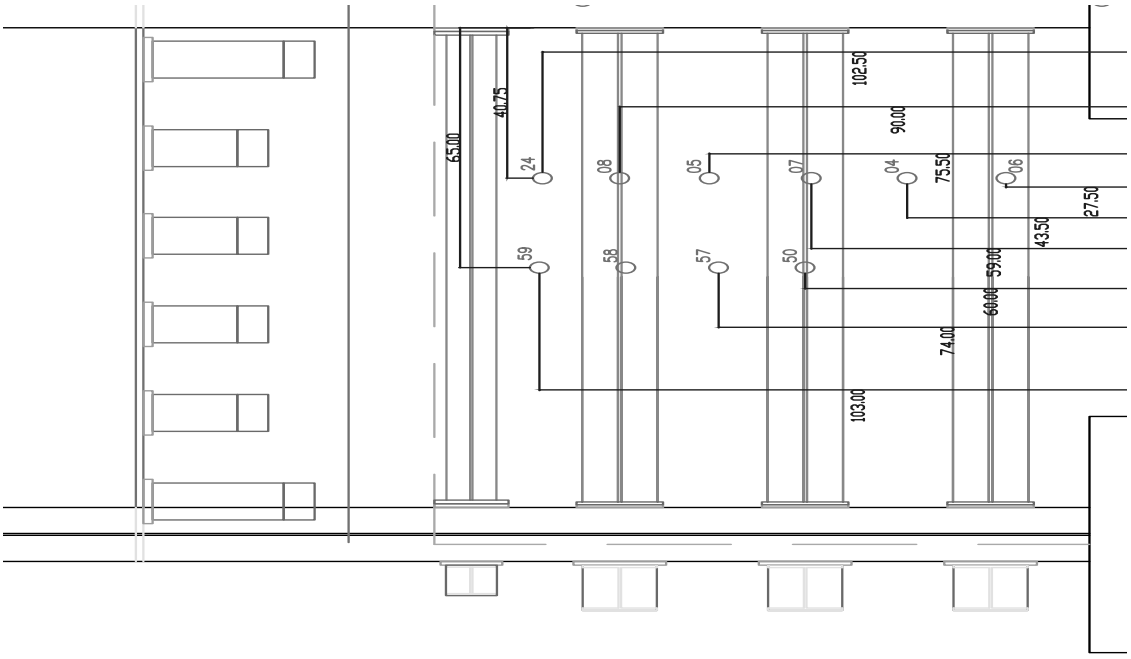

Figure 3-13: Steel frame instrumentation – North elevation view

3.4.1.4 Retaining Wall Deformation

Deformation of the RCC retaining wall was measured with 9 string potentiometers mounted at the top, midpoint, and base of the wall. Figure 3-14 shows the placement of the instruments along the back face of the retaining wall.

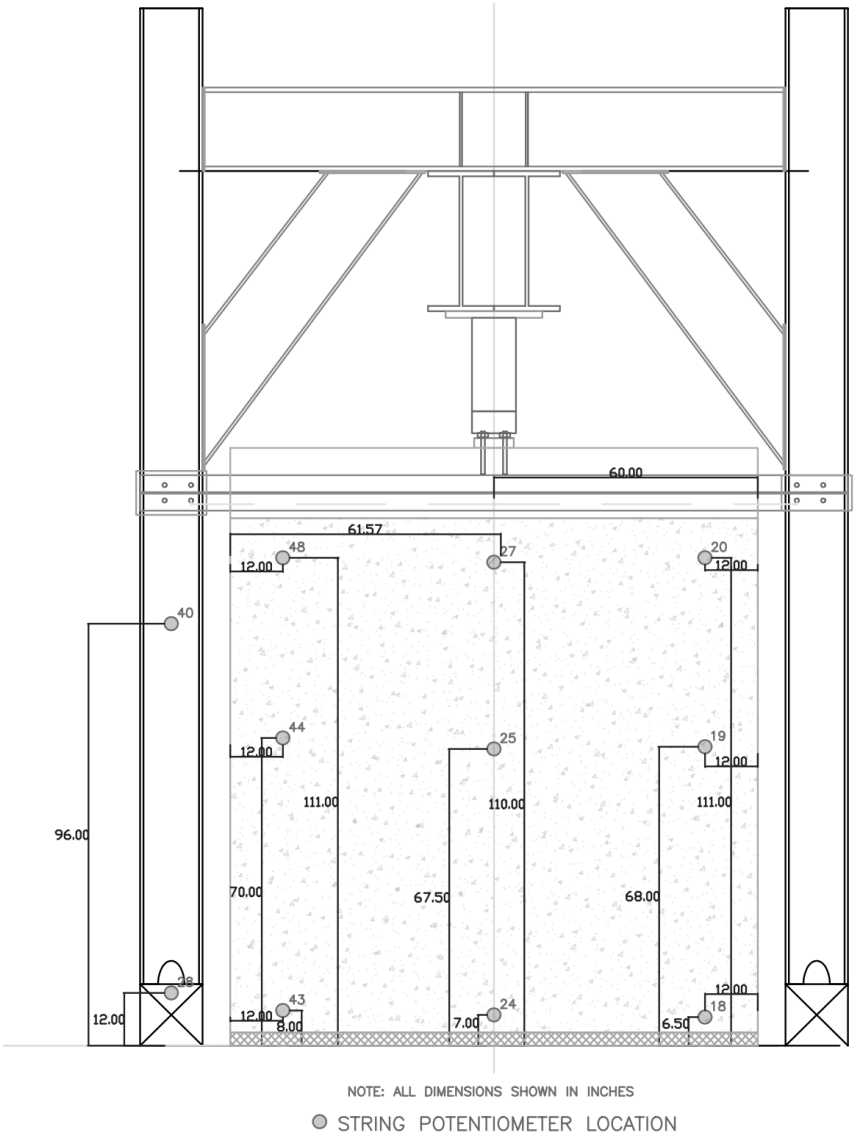

Figure 3-14: RCC wall instrumentation – elevation view

String potentiometer 27, located at the top of the wall, produced results inconsistent with the other measurements throughout the duration of the test. After the test was completed, troubleshooting revealed that the readings produced at this location were not valid. Values for the deformation of the wall at this location were obtained by averaging the readings of the potentiometers located at the top corners of the wall.

3.4.1.5 Internal Stresses and Deformations

Pressure, strain, and temperature sensors were placed inside the LCC block. A thermocouple was placed in each lift approximately 6" from the face of the retaining wall to monitor the curing temperature and temperature at the time of testing. Two soil deformation sensors were embedded in the LCC to identify internal horizontal strain during loading. Two additional pressure sensors were embedded approximately 6" from the face of the RCC wall at different depths to measure internal horizontal pressures. These sensors all malfunctioned due to inadequate waterproofing, and no usable data was obtained. No vertical pressure sensors were placed inside the LCC.

3.4.1.6 Vertical Surcharge Deformation

A series of 3 string potentiometers were placed on each concrete surcharge beam—one in the center of the beam and one at each end. These instruments were anchored to an independent reference frame to determine the total deformation of the surface of the LCC block. Figure 3-15 shows a plan view diagram of the concrete beams and instrumentation.

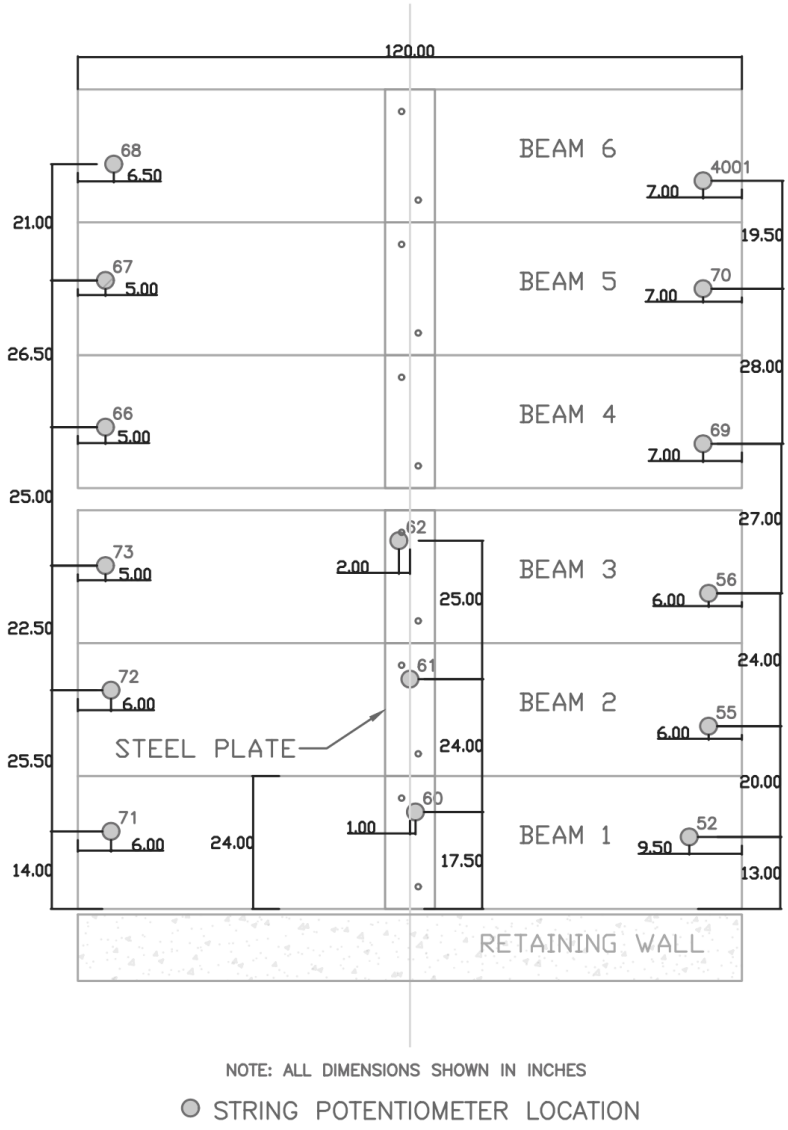

Figure 3-15: Concrete surcharge beam instrumentation layout – plan view

3.4.2 Free-Face Test Instrumentation

All pressure plates and temperature sensors used in the confined test remained in place for the unconfined test. The location of the string potentiometers remained largely unchanged between the two tests, but a few instruments were either moved to a different location or added

to the existing set to better acquire data near the free face. All six concrete beams atop the LCC block remained in place throughout the duration of both tests.

3.5 Placement Procedures

All LCC used in this test was prepared and placed by Cell-Crete Corp. The material was mixed in one-yard batches and pumped on-site and was continuously monitored by an on-site foreman.

3.5.1 Test Box Placement

The cellular concrete was placed in 2.5-foot-thick lifts to a height of 10 feet behind the RCC retaining wall over a four-day period (one lift per day). LCC was pumped into the test box at a rate of approximately 0.25 cubic yards per minute. The contractor measured the unit weight of the concrete at intervals of 5 minutes to ensure the mix stayed within the prescribed bounds. The average unit weight of the LCC was 28.5 pcf, and no unit weight test yielded a weight higher than 29 pcf or lower than 27 pcf.

The concrete was pumped directly into the testing box using standard construction practices and methods, and no consolidation methods were employed during or after the pour. After the final lift was completed, the top was lightly screeded to provide a level bearing surface for the concrete beams but was not finished using trowels or floats. The temperature in the laboratory was held between 70 and 75 degrees throughout the duration of the pouring and curing process to minimize any adverse effects due to changes in the curing environment.

3.5.2 Direct Shear Box Placement

The direct shear split boxes were filled by hand using buckets. Plastic buckets were filled with cellular concrete at the end of the pumping hose, and the concrete was carefully poured into each split box. Consolidation methods were not used, and the cold joint between lifts in the split box was not screeded or finished. Each lift in the split boxes was poured within a 5-minute interval to minimize any variance within the material.

3.6 Loading Procedures

3.6.1 Retained-Face Test Loading Procedure

Load was applied to the surface of the LCC block in increments of 50 kips until the total load reached 200 kips (890 kN); load was then applied in increments of 25 kips (111 kN). Each load increment was held for 3 minutes. If excessive frame deflection or faulty data acquisition occurred, the holding period was lengthened slightly so the problem could be diagnosed and resolved.

Load was applied with an electric hydraulic pump. The hydraulic pump was connected to all three jacks, loading the LCC with equal pressure. During the load holding period, the pump was switched off, but pressure was not released from the system. Settlement of the cellular concrete during the load holding periods allowed the hydraulic cylinders to extend slightly, thereby decreasing the pressure in the hydraulic system. Loading was stopped once the maximum allowable load for the frame was reached.

3.6.2 Free-Face Test Loading Procedure

The free-face test followed the same loading procedure as the retained-face test. When the cellular concrete began to fail and a clear shear plane developed, the loading was stopped to prevent the concrete blocks from falling off the top surface.

3.6.3 Direct Shear Test Procedures

The direct shear tests were carried out using hand-pump hydraulic pistons to apply both shearing and normal force to the samples. The load applied by each piston was measured with a load cell while the displacement of each half of the split box was measured with a string potentiometer. Load was applied to achieve a strain rate of approximately 1% per minute. The loading was stopped shortly after the peak shear stress was obtained.

4 PRELIMINARY TESTING DATA

LCC was placed in both the large-scale test box and sample cylinder containers in both November 2019 and January 2020, but material inadequacies required that the LCC be discarded. Preliminary laboratory and full-scale tests were carried out on these samples despite the known defects in an effort to optimize the test setup and rehearse the designed procedures prior to gathering usable data. No data obtained from the laboratory samples or the preliminary full-scale test was used in the conclusions of this research; however, this chapter will present results gathered from these tests and address the material problems so as to properly document the proceedings of the research.

4.1 Material Behavior

In November 2019, the LCC poured at the BYU laboratory exhibited many strange behaviors. The most notable behavior was a boiling effect, which began between 75 and 80 minutes after each lift was placed. After sitting dormant for this period of time, air bubbles began rising from the depths of the LCC and popping on the surface. The LCC surface looked much like boiling water, with bubbles coming to the surface very regularly. Neither the contractors nor anyone on the research team had seen such a behavior before.

The “boiling” effect has been seen in various projects around the world, but it is extremely rare. The effect was studied by Jones, Ozlutas, and Zheng (2016) to better understand

its causation. Their findings indicate that LCC batches with densities between 25 and 62 pcf (400 to 1000 kg/m^3) were generally stable, while mixes with densities less 25 pcf (400 kg/m^3) regularly "boiled" between 70 minutes and 120 minutes after the material was placed. By replacing a small amount of the Portland Cement in the mix with CSA cement, this research team was able to create a stable LCC mix. CSA cement drastically reduces the initial set time, allowing the LCC to set before the air bubbles would normally begin to rise.

4.1.1 November 2019 Casting

The mix design used in the November 2019 tests produced LCC with a density between 27 and 28 pcf, which falls outside the range at which instability may be generally expected (Jones et al., 2016). After the LCC finished "boiling", it was observed that the depth of the lift had been reduced from approximately three feet to two feet due to the escaped air. This indicated that the LCC simply collapsed on itself, allowing all the entrained and entrapped air to escape. Though the LCC in the main test box collapsed, none of the samples placed in cylinder molds during the filling of the box collapsed. Figure 4-1 and Figure 4-2 show the result of the collapse, with approximately 1/3 of the original lift height lost.

After the LCC had finished "boiling", several sample cylinder molds were filled with the collapsed material before it reached initial set so laboratory tests could be performed and the properties of the post-collapse material could be compared to the un-collapsed cylinder samples taken previously. Density tests performed on both cylinders after curing for a period of 24 hours showed that the density of the material increased from 27 to 43 pcf (4.25 to 6.75 kN/m^3) during the collapse, an increase of just over 50%.

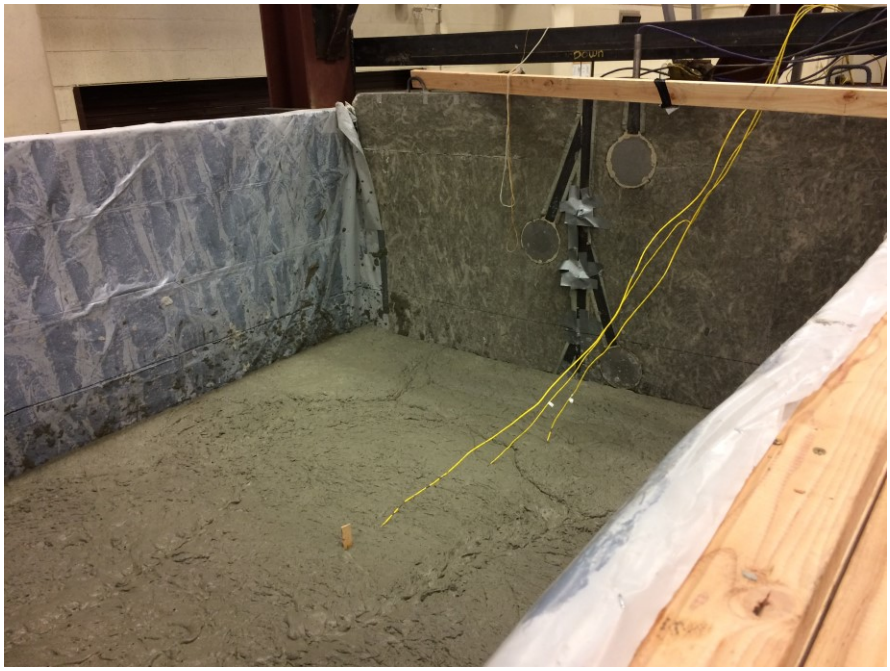

Figure 4-1: November 2019 LCC immediately after lift placement

Figure 4-2: November 2019 LCC after full collapse

Efforts were made to replicate the behavior on a small scale. After the first lift collapsed, the research team explored several avenues to try to prevent a similar event from happening the next day. Special sample cylinder molds were prepared and treated with various chemicals or processes to attempt to isolate the problem. Molds were lined with molybdenum grease, WD-40, and plastic sheeting. Additional molds were allowed to cure at various temperatures and humidities. The second lift was poured the next day and ultimately collapsed in the same manner as the first, but none of the sample cylinders, treated or non-treated, exhibited any degree of collapse. After a thorough chemical evaluation of the materials used in the pour was performed, traces of petroleum were found in the concentrated foaming agent. Petroleum products are naturally anti-foaming agents, and these traces may have aided the LCC collapse; however, no conclusive evidence was found that this was the cause, and the effect was never replicated on a small scale.

Core and block samples were taken from the large-scale test box and compared to sample cylinders. Figure 4-3 shows the difference in pore size between the collapsed sample and the non-collapsed sample. The air bubbles in the collapsed sample were significantly larger than the non-collapsed sample, indicating that the mix became unstable at some point in the curing process, allowing air bubbles to join and rise to the top. The difference in color is due to a difference in curing environment and extraction time—the cylinder pictured was damp from curing in a humid environment (one of the test variables) and from being recently extracted from the polystyrene cylinder mold, while the block sample of the collapsed LCC cured in the laboratory and had been extracted several hours earlier.

Figure 4-3: Pore size comparison between a cast cellular concrete sample (left) and a block sample of the collapsed cellular concrete (right).

4.1.2 January 2020 Casting

After the November lifts cured, the LCC was excavated from the test box, the retaining wall and pressure sensors thoroughly cleaned, and the plastic liner in the test box was replaced. In January 2020, LCC was once again poured into the large-scale test box. This pour utilized a lift height of 2'-6" rather than the 3'-4" height used in November in an attempt to decrease the vertical stresses on the material at the bottom of each lift, and several samples were again cast in molds lined with plastic, grease, oil, and other chemicals that may have previously contributed to the collapse. The steel frame and box walls were constantly monitored with an accelerometer and string potentiometers to track any movements or vibrations that may have influenced the LCC.

The first two lifts cured without collapsing, but the third lift collapsed in the same manner as the November lifts. Nothing was adjusted about the materials or pouring process between lifts 2 and 3, and again, none of the sample cylinders collapsed. This lift was excavated immediately upon collapse, before it reached initial set. The cause of this collapse is still unknown, but determining the cause is outside the scope of this research.

After the lift was excavated, the contractor decided to cease using Type I/II/V cement stored in a cement bulk truck and to begin using Type I/II cement sourced from a local hardware store. The final two lifts experienced no collapse.

Though a total height of 10'-0" was cast, the difference in cement type was deemed unacceptable and quantitative results from the testing were not used. The maximum curing temperature of each of the first two lifts (Type I/II/V cement) was approximately 110ºF, while the maximum curing temperature of each of the next two lifts was approximately 160ºF. This difference in curing temperature indicated that the top two lifts cured very differently than the bottom two lifts and likely created a non-uniform backfill material. Despite the material inconsistency, a full-scale test was still carried out to ensure the test layout (including the frame construction, instrumentation calibration, and procedural design) would yield suitable results. The qualitative data obtained in this test was used to revise the testing process used in future tests.

4.2 Cylinder Test Data

Sample cylinders were tested in January 2020 but not November 2020. These cylinders had a remarkably low strength, averaging approximately 12 psi. Notably, each cylinder appeared to have a very soft layer at the bottom—the top of the cylinder was very firm, but the bottom could easily be compressed by a finger's touch. A cylinder comparison was done to determine if

the weak layer at the bottom was causing a large problem with the compressive strength. Figure 4-4 shows a comparison between two tests performed on a single cylinder. First, an unconfined compression test was performed on the full cylinder. Only the bottom 0.5" of the cylinder experienced any cracking or spalling during this test. A second test was then performed after the bottom 2" of the cylinder was removed. Without the bottom 2", the height/diameter ratio of the cylinder was reduced from 2.0 to 1.34. An approximate correction factor was applied to the compressive stress values of the shorter cylinder to account for this ratio adjustment. ASTM C42 recommends a factor of 0.94 be applied to concrete cores with a H/D ratio of 1.34, while research by Güneyli and Rüşen (2016) suggest that a factor of 0.76 be applied to clay specimens with that same H/D ratio. A factor of 0.76 was applied to this sample because current research indicates lightweight cellular concrete behaves much more like a stiff clay than traditional concrete.

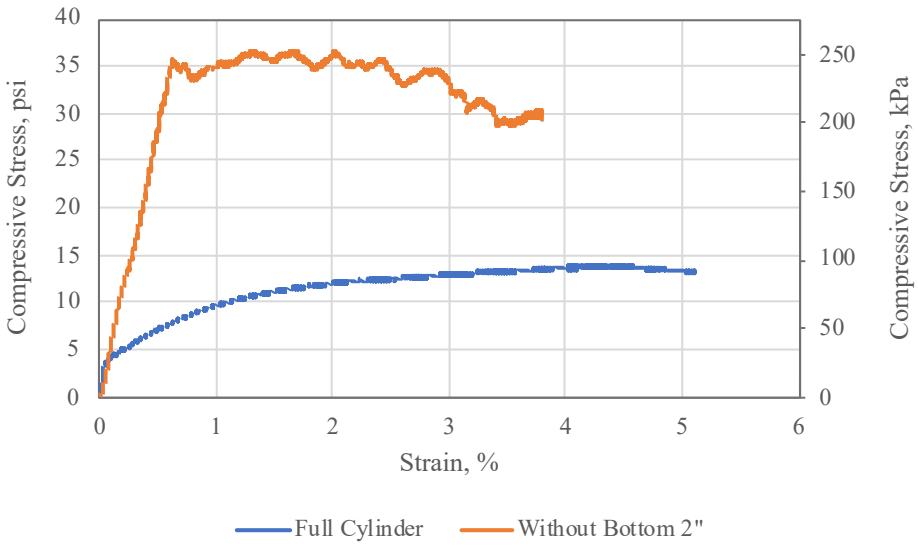

Figure 4-4: Cellular concrete stress-strain curve for sample cylinders with and without weak layers

Even with the correction for geometry, there is still a significant difference between the two cylinders. It is clear to see that the soft layer at the bottom of the cylinders played a role in the low strength and that the cylinder had reasonably good strength without that layer. However, without taking full-height core samples from the LCC held within the large-scale test box, the presence and/or magnitude of the soft layers potentially in the large block was unknown. This inconsistency in the samples further contributed to the decision to reject the results of the test.

4.3 RCC Wall or Retained-Face Test Data

A full-scale active pressure test was performed in January 2020, after the sample cylinders reached an approximate compressive strength of 35 psi without the weak bottom layer. This required an average of seven days of cure time. For this test, a uniform surcharge was applied to the entire surface of the LCC (see section 3.4.3.1).

4.3.1 Vertical Displacement

Figure 4-5 shows the stress-strain plot of the LCC block under uniform surcharge pressure. This figure also includes the stress-strain curves of the cylinders examined in Section 4.2. The axial strain was determined by dividing the axial settlement by the original height—this procedure was used for all strain measurements presented in this report. The behavior of the large-scale LCC is very similar to the behavior of the cylinder with the bottom 2” removed and strength corrected as described in Section Cylinder Test Data, indicating that any weak layers present in the large block did not have a pronounced effect on the material strength.

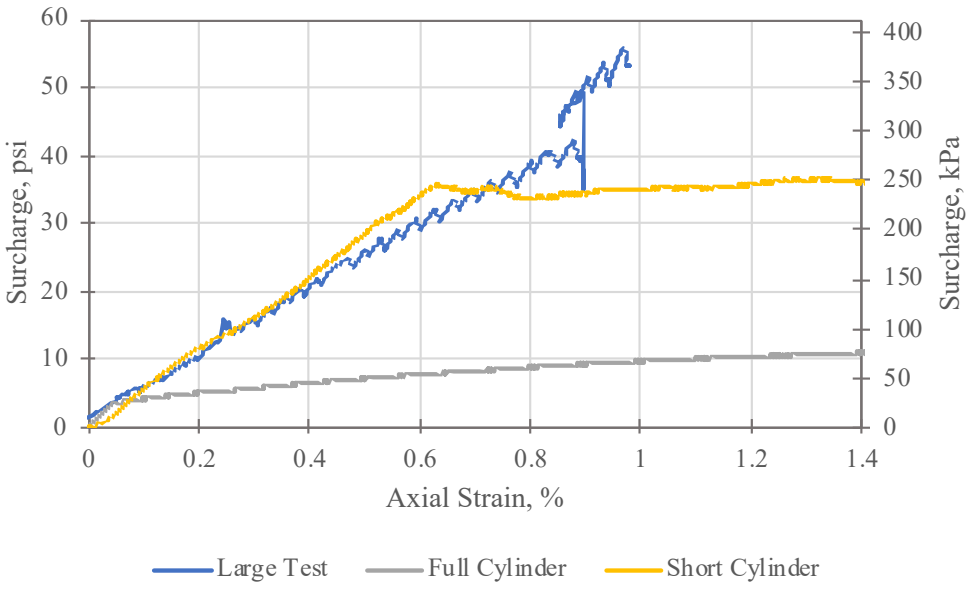

Figure 4-5: Stress-strain curve comparison between test cylinders and large-scale LCC block.

During the full-scale test, load was applied to the LCC in increments of 50 kips, or 2.9 psi (20.0 kPa). Once the applied surcharge reached 120% of the unconfined compressive strength, the pressure in the two hydraulic jacks furthest from the RCC wall was released. Additional load was then applied to the remaining four jacks in increments of 25 kips, or 2.2 psi (15.0 kPa). A jump in applied surcharge is clearly seen in Figure 4-5 at an axial strain of approximately 0.9%—this jump was caused by the unloading of the two jacks and subsequent reloading of the four jacks nearest the wall.

After this jump, the slope of the stress/strain line remained approximately the same, indicating that the cellular concrete was still deforming primarily in an elastic manner, despite being loaded to a maximum compressive pressure of 56 psi (386 kPa), or nearly 160% of the unconfined compressive strength. The test was stopped once the steel reaction frame's capacity was reached, even though neither the LCC nor RCC wall had failed.

4.3.2 Horizontal Pressures

The horizontal pressures measured on the RCC wall during this test were very small. Table 4-1 shows the maximum pressures recorded at each location on the inside face of the RCC wall. During this test, many instruments were not properly calibrated or sealed against moisture, so only limited data is available.

Table 4-1: Maximum recorded pressures on Geokon® pressure plates

Plate Number	Depth, ft (m)	Max Pressure, psi (kPa)
3	5.67 (1.73)	1.36 (9.4)
4	4.25 (1.3)	4.09 (28.19)
5	2.17 (0.66)	1.65 (11.38)

Compared to the maximum surcharge of 56 psi, a horizontal pressure of 4 psi is extremely small. From this data, it can be concluded that loading the entire surface of a cellular concrete block does not produce significant horizontal pressures on a retaining structure; rather, the pressure is mostly supported by the cellular concrete like it would be in an unconfined compression test. However, because a surcharge greater than the unconfined compressive strength was applied to the LCC block and no indication of failure was seen, the confinement likely added to the compressive strength of the material.

4.3.3 Wall Movements

The movement of the retaining wall, though small, resulted in valuable insights as to the behavior of the cellular concrete. Figure 4-6 shows the measured deflection of the top of the retaining wall as a function of the surcharge pressure. This figure also shows the point at which

the two hydraulic jacks furthest from the RCC wall were unloaded. When all 6 jacks were loaded equally, the deflection of the wall was almost 0; however, after the switch was made to using only 4 jacks, the wall began to show measurable deflection.

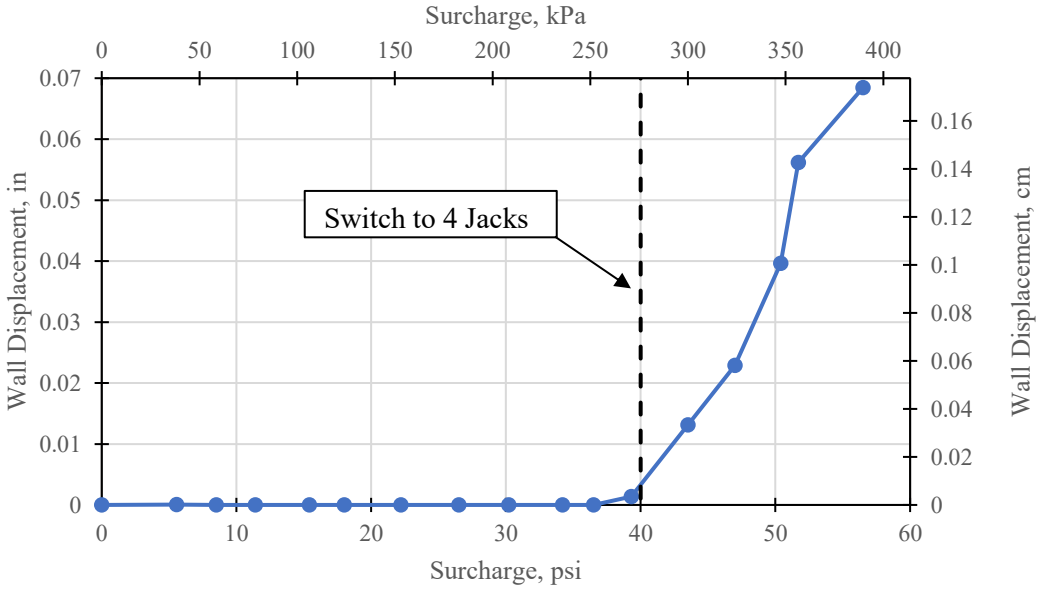

Figure 4-6: January 2020 RCC wall deflection vs. applied surcharge

Movements of the other walls reveal more important patterns. Deflections were measured at the center (horizontally and vertically) of each of the wood walls surrounding the LCC block. Figure 4-7 compares the measured deflections of the wood walls at various surcharge levels with the measured deflection at the top of the RCC wall. In Figure 4-8, the deflections of the North and South walls have been added together to create a directional deflection envelope; likewise, the East and West (RCC) wall deflections have been added together. These directional deflection lines show how the LCC expanded in each direction as it was compressed.

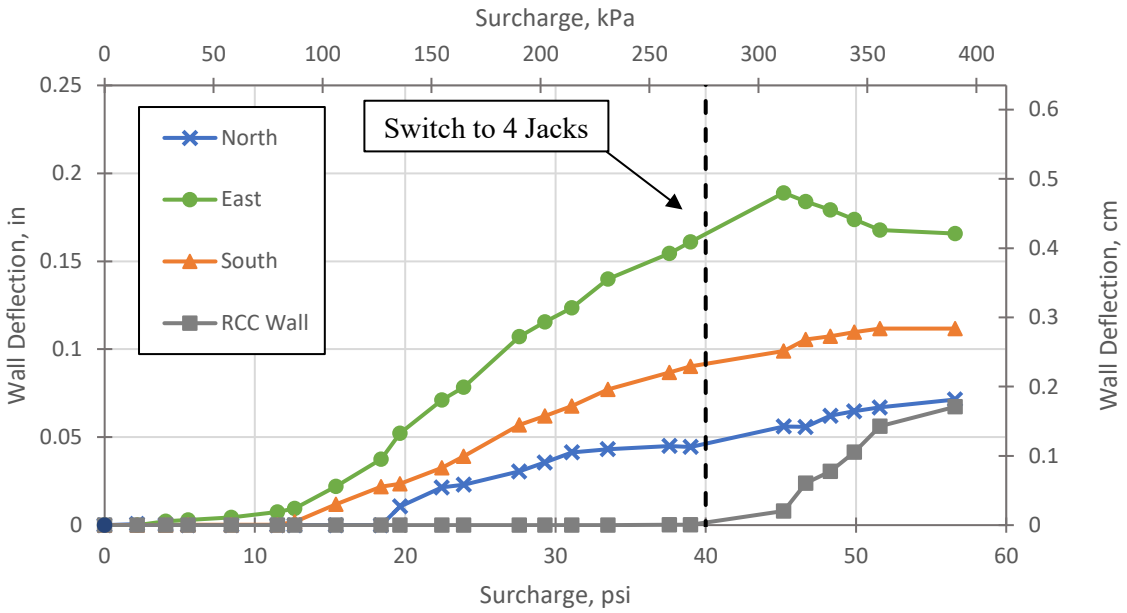

Figure 4-7: Comparison of individual wall deflections in uniform-loading test

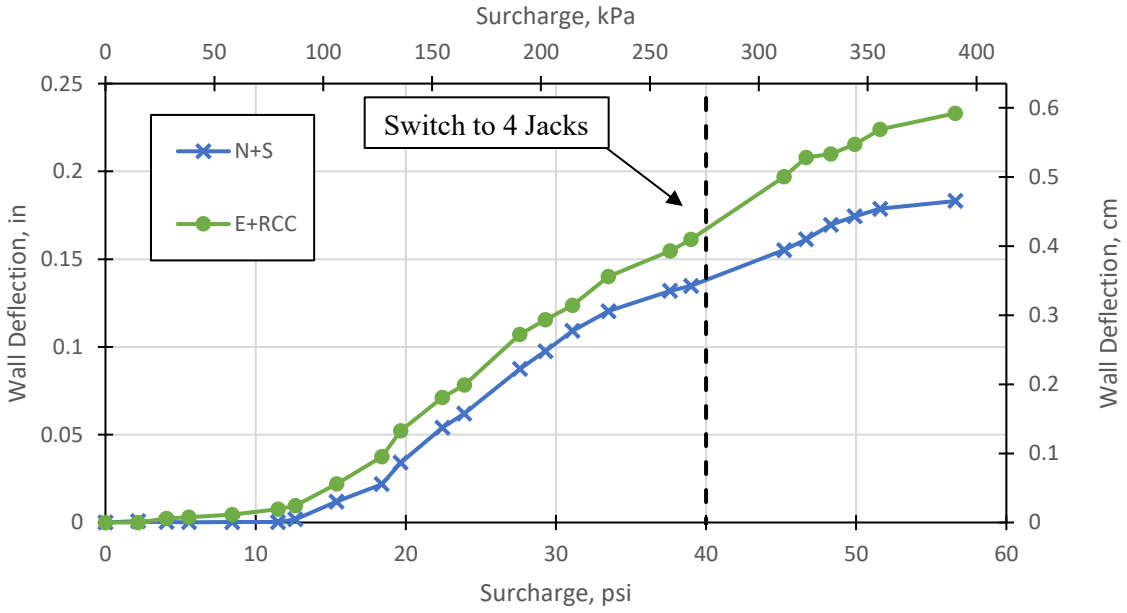

Figure 4-8: Comparison of directional envelope wall deflections in uniform-loading test

The combined deflection of the North and South walls approximately matches the combined deflection of the East and Retaining walls throughout the test. This indicates that the material expanded approximately equally in all directions. Because the East wall (wood wall supported by steel beams) had a much lower stiffness than the RCC wall (reinforced concrete), it absorbed most of the lateral expansion in the East-West direction.

When the switch was made to load four jacks instead of six, the surcharge load was concentrated closer to the retaining wall and further from the East wall. This caused the effective stiffness of the East wall to increase dramatically because the portion of LCC no longer being loaded acted as an additional confining surface for the loaded LCC, and the LCC began to expand toward the retaining wall rather than continuing to push only the East wall. The East wall deflection began to decrease at the same time as the RCC wall deflection increased, but the combined deflection of these two walls continued to climb at almost the same rate as before the switch was made.

After the change from six jacks to four, the North and South walls did not have any significant change in the rate of deflection with increasing surcharge.

4.3.4 Conclusions

Several conclusions can be drawn from this preliminary test. The first is that LCC is very unlikely to fail due to uniform surcharge over the entire surface. The reaction frame used in this experiment was unable to apply enough pressure to the top of the entire block to cause failure, even when the unconfined compressive strength was exceeded by more than 50%. If a cellular concrete backfill structure is loaded uniformly and effectively confined, the capacity of the backfill may greatly exceed the unconfined compressive strength.

The second conclusion is that the steel reaction frame was not stiff enough or strong enough to cause a full compression failure through uniform surcharge. To obtain usable data with the testing equipment available, the LCC must fail in shear or combined shear/compression rather than solely compression. Because no shear plane developed in the uniform test, an induced shear plane is required to achieve the desired results.

The final conclusion is that loading only a few hydraulic jacks close to the face of the retaining wall has the highest likelihood of successfully producing measurable pressures and deflections on the retaining wall. Not only would the retaining wall likely deflect more, as shown in Figure 4-7 and Figure 4-8, but applying surcharge to only a portion of the LCC surface would likely induce a shear plane, thereby aiding in producing an active pressure failure wedge. A shear failure typically happens with far less surcharge than a pure compression failure; such failure is the critical case for designing retaining structures because it is the most critical loading situation, and as such, is the focus of this research.

4.3.5 Modifications and Adjustments

The procedure for the next test was modified so only three of the six hydraulic jacks applying load to the top of the LCC would be loaded at a time.

After the RCC test was conducted by loading the three jacks nearest the retaining wall, a second test would be conducted on the same LCC block without the presence of the retaining wall. To create this free-face condition, the East wall of the reaction frame would be removed and the three jacks nearest the now-exposed face (opposite the RCC wall) would be loaded. The RCC wall would remain in place during this test. These modifications would ensure that the capacity of the reaction frame was not exceeded, an induced shear plane would develop, and a comparison could be made between retained- and free-face conditions.

5 CELLULAR CONCRETE PROPERTIES

In June 2020, four consecutive lifts of LCC were successfully placed into the large-scale test box. Several samples were also taken from each lift for evaluation in the laboratory. The placement processes were identical to the processes used in November 2019 and January 2020 (see Section 3.6), but the Portland Cement used was sourced from a local hardware store instead of a local cement plant. The LCC did not collapse, the measured cast densities were within acceptable tolerances, and the curing temperature of each lift was approximately the same, indicating that the material was approximately uniform throughout. Full laboratory tests were performed on the various samples obtained during the placement process. Chapter 5 will present the results of these laboratory tests. Later chapters will present the data obtained in the large-scale active pressure test and further analyses of the test data.

5.1 Mixture Properties

The cellular concrete mixture used in this test was designed by Cell-Crete to produce a minimum unconfined compressive strength of 40 psi after a curing period of 28 days. The mix design is shown in Table 5-1. This mix design is a commonly used mix design for abandoned pipe fills and structural backfill applications.

Table 5-1: Engineered cellular concrete mix design

Mix Component	Amount lb/yd^3 (kg/m^3)		Specific Gravity	Density pcf (kg/m^3)		Absolute Volume ft^3 (m^3)	
Potable Water	232.45	(137.91)	1.00	62.40	(999.58)	3.73	(0.11)
Portland Cement (ASTM C150)	422.64	(250.74)	3.15	196.50	(3147.7)	2.15	(0.06)
Foam (ASTM 796-97, 869)	73.91	(43.85)	0.05	3.50	(56.07)	21.12	(0.6)
Total	729.00	(432.50)	-	27.00	(432.51)	27.00	(0.76)

Design Notes:
1. Design Strength: 40+ psi (276 kPa)
2. Water/Cement Ratio = 0.55

After all tests in this research were completed, questions arose about the contractor's adherence to this mix design because the LCC used in later research projects at BYU had a much higher unit weight than anticipated, even though the mix design was identical. After investigation, the contractor revealed that 5 bags of type I/II Portland Cement, weighing approximately 94 lbs (0.418 kN) each, were added to each cubic yard of cellular concrete, for a total of 470 lbs. Because the contractor's mixer can only hold 1 cubic yard of concrete at a time, the weight and volume of the foam and water were likely modified to accommodate the increased cement volume because there was simply not enough space in the mixer.

Another mix design is presented in Table 5-2, which estimates the properties of the actual mix used in this research. In this estimated mix, the weight of the added water remains unchanged from the previous design, but the weight of added foam has been decreased to reduce the actual volume to 1 cubic yard. The expected density of this new mix aligns better with the 28.5 pcf average cast density recorded during the pours. This mix design also has a much lower water-cement ratio, which indicates that the LCC will likely be stronger than originally anticipated.

Table 5-2: Estimated as-mixed cellular concrete mix design

Mix Component	Amount lb/yd^3 (kg/m^3)		Specific Gravity	Density pcf (kg/m^3)		Absolute Volume ft^3 (m^3)	
Potable Water	232.45	(137.91)	1.00	62.40	(999.58)	3.73	(0.11)
Portland Cement (ASTM C150)	470.00	(278.84)	3.15	196.50	(3147.70)	2.39	(0.07)
Foam (ASTM 796-97, 869)	73.07	(43.35)	0.05	3.50	(56.07)	20.88	(0.59)
Total	775.52	(460.09)	-	28.72	(460.11)	27.00	(0.76)

Design Notes:
1. Design Strength: 40+ psi (276 kPa)
2. Water/Cement Ratio = 0.49

5.2 Laboratory Testing

5.2.1 Unconfined Compression Testing

Unconfined compression tests were performed on samples from each LCC lift in general accordance with ASTM C495, modified for laboratory and timing constraints. Recommendations from experienced testing professionals were also considered in obtaining and testing samples.

A minimum of eight sample cylinders were obtained from every lift. These samples were taken at uniform time intervals as the LCC was being placed in the large-scale test box. The samples were cast in three lifts as recommended by the Cell-Crete engineers rather than two lifts as required by ASTM C495 to allow large, entrapped air bubbles to escape, thereby reducing the variation in cylinders. The samples were cast in closed-cell polystyrene containers with each cylinder having a diameter of 3” and a height of 6”. Once filled, the containers were placed on the floor of the laboratory next to the large-scale test box to cure.

After 24 hours of curing at room temperature in the laboratory, the containers were moved to a humid environment to cure for the next 48 hours. The sample cylinders were then

extracted from the molds and placed in a controlled-storage container with a temperature of 72 ± 3 º F and humidity of approximately 30%, where they remained until they were tested.

Prior to testing, the cylinders were weighed and measured in general accordance with ASTM C495. Cylinders were not capped before testing but were ground with a sander to produce a flat top and bottom surface. Each cylinder' fell within the prescribed tolerances for height, diameter, and plumb, but the cylinders were not oven-dried prior to testing.

Preliminary sample testing indicated that a strain rate of between 0.08 and 0.15 inches per minute was satisfactory to ensure that the peak loading occurred at a time of approximately 60 seconds. A rate of 0.1 inches per minute, or approximately 1.7% strain per minute, was selected for all cylinders tested.

5.2.1.1 UCS Test – Test Day

A total of 16 cylinders (four cylinders from each lift) were tested immediately prior to the RCC retained-face test. These cylinders are representative samples of the material placed in the large test box. The unconfined compressive strength and density of each cylinder is summarized in Table 5-3.

The UCS tests were performed after the bottom lift had cured for seven days and the top lift had cured for four days. The average unconfined compressive strength of all the lifts at the time of testing was 105 psi with a standard deviation of 17 psi. Because the average compressive strength was already 105 psi, far beyond the minimum 28-day strength of 40 psi for Class II LCC, the RCC test was performed without waiting 28 days, when the strength would have been much higher and likely unrepresentative of typical Class II LCC.

Table 5-3: Unconfined compressive strengths and densities of sample cylinders immediately prior to the RCC retained-face test.

Cylinder Label	Cure Time (days)	Cast Density (pcf)	Cured Density (pcf)	Unconfined Compressive Strength (psi)
0128007-01	7	28.0	30.4	126
0128007-02	7	28.0	31.7	108
0128007-03	7	28.0	30.5	103
0128007-04	7	28.0	30.5	124
0229006-01	6	29.0	32.6	89
0229006-02	6	29.0	32.7	105
0229006-03	6	29.0	32.6	109
0229006-04	6	29.0	32.7	113
0327005-01	5	27.0	27.4	88
0327005-02	5	27.0	27.3	77
0327005-03	5	27.0	27.8	78
0327005-04	5	27.0	27.7	78
0429004-01	4	29.0	31.9	112
0429004-02	4	29.0	32.5	129
0429004-03	4	29.0	32.1	114
0429004-04	4	29.0	31.6	116
Avg. – Lift 1	7	28.0	30.8	115
Avg. – Lift 2	6	29.0	32.7	105
Avg. – Lift 3	5	27.0	27.6	80
Avg. – Lift 4	4	29.0	32.0	120
Combined Avg.	5.5	28.3	30.8	105

A large variation in strength exists among the cast cylinders. Figure 5-1 and Figure 5-2 show the unconfined compressive strength of each cylinder compared to its cast density and cure density, respectively, along with best-fit lines and the coefficient of determination for each data set. The time designation “Test-Day” refers to the day on which the large-scale active pressure test was performed, with all lifts having between four and seven days of cure time, as previously discussed.

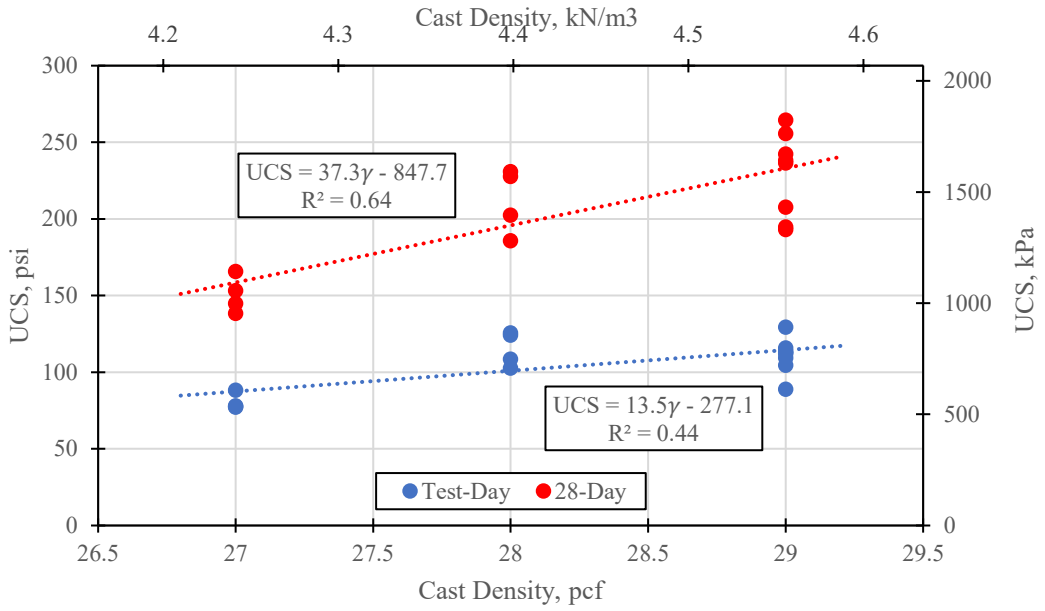

Figure 5-1: Unconfined compressive strength (UCS) and cast density of cellular concrete batches with 7- and 28-day cure times.

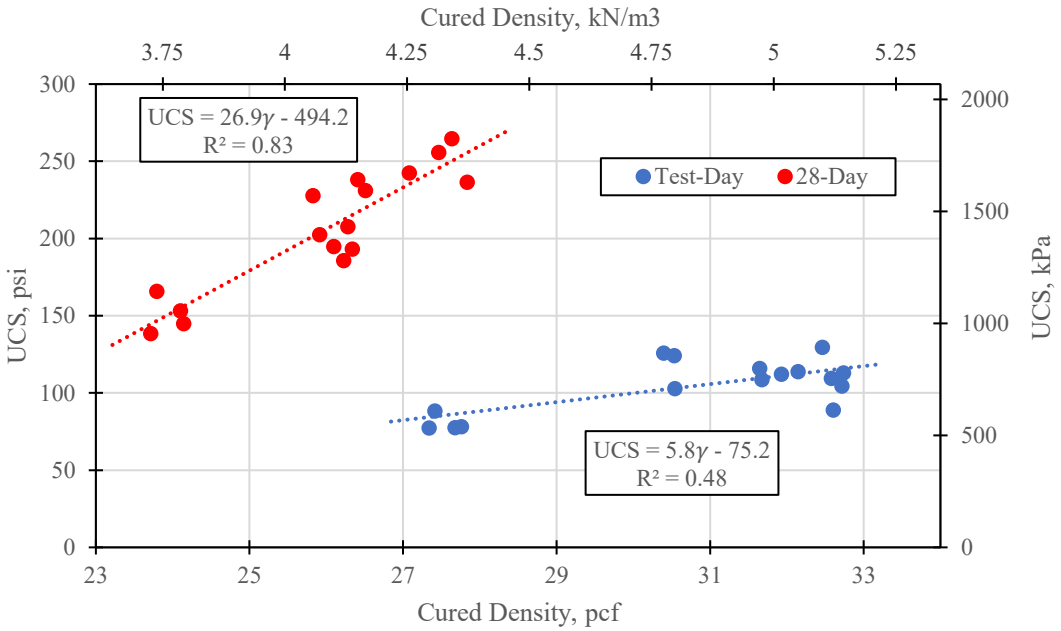

Figure 5-2: Unconfined compressive strength (UCS) and cured density of cellular concrete batches with 7- and 28-day cure times.

The trends in these figures indicate that there is a higher correlation between cured density and unconfined compressive strength than the cast density and strength. It further indicates that the relationship between density and strength gets stronger with an increase in cure time. These relationships will be explored in subsequent sections.

5.2.1.2 UCS Test Results – 28-Day Strength

The 28-day samples show a strong correlation between cured density and compressive strength, with a coefficient of determination of 0.83 as shown in Figure 5-2. $UCS = 26.9\gamma - 494.2$ Equation 5-1 may be used to estimate the compressive strength of the cellular concrete at a cure time of 28 days.

$$UCS = 26.9\gamma - 494.2 \qquad \text{Equation 5-1}$$

where γ = air-dry density of the cured material (pcf) and UCS is measured in psi. This equation fits the measured data in this research well but tends to overestimate the strengths obtained by other researchers. Figure 5-3 and Figure 5-4 show measured strengths and densities from this research for test-day and 28-day strengths, respectively, plotted on a chart developed by Tiwari et al. (2017) to estimate the 28-day strength of LCC based on density. Companion cylinders tested by Gerhart Cole Inc. (GCI), a local geotechnical engineering and materials testing firm, are also shown on these two figures. No significant difference between the cylinders tested by BYU and GCI was observed. GCI only performed tests on the test-day cylinders—all 28-day tests were performed at BYU.

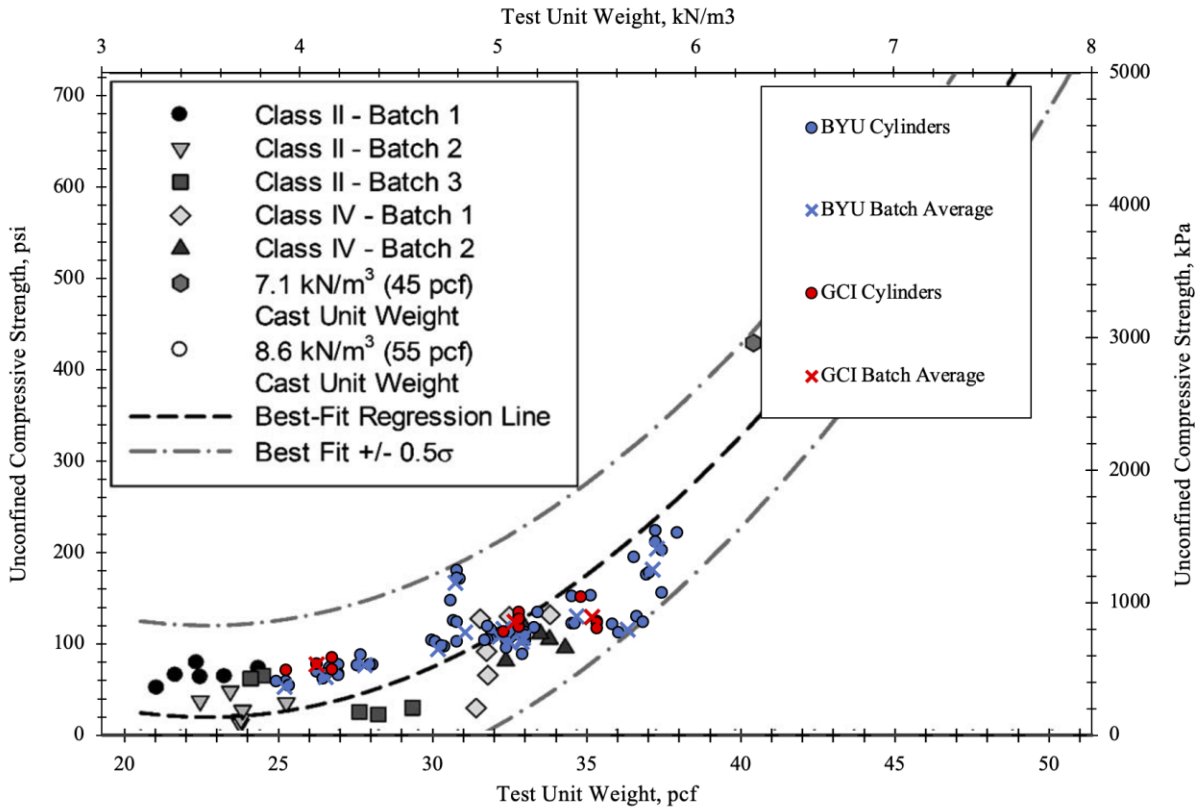

Figure 5-3: Test-day unconfined compressive strength data from BYU and GCI tests compared with 28-day results from Tiwari et al. (2017).

The test-day strengths follow the suggested 28-day strength correlation quite well, while the 28-day strengths all fall outside the bounds of 0.5 standard deviations. Determining the cause of the large strength increase is outside the scope of this research, but it may be partially due to a combination of the cement type, an increased water/cement ratio as described in Section 5.1, or other environmental factors. Because the strengths on test-day resembled average 28-day strengths, the test was performed and analyzed as if the material had cured for 28 days.

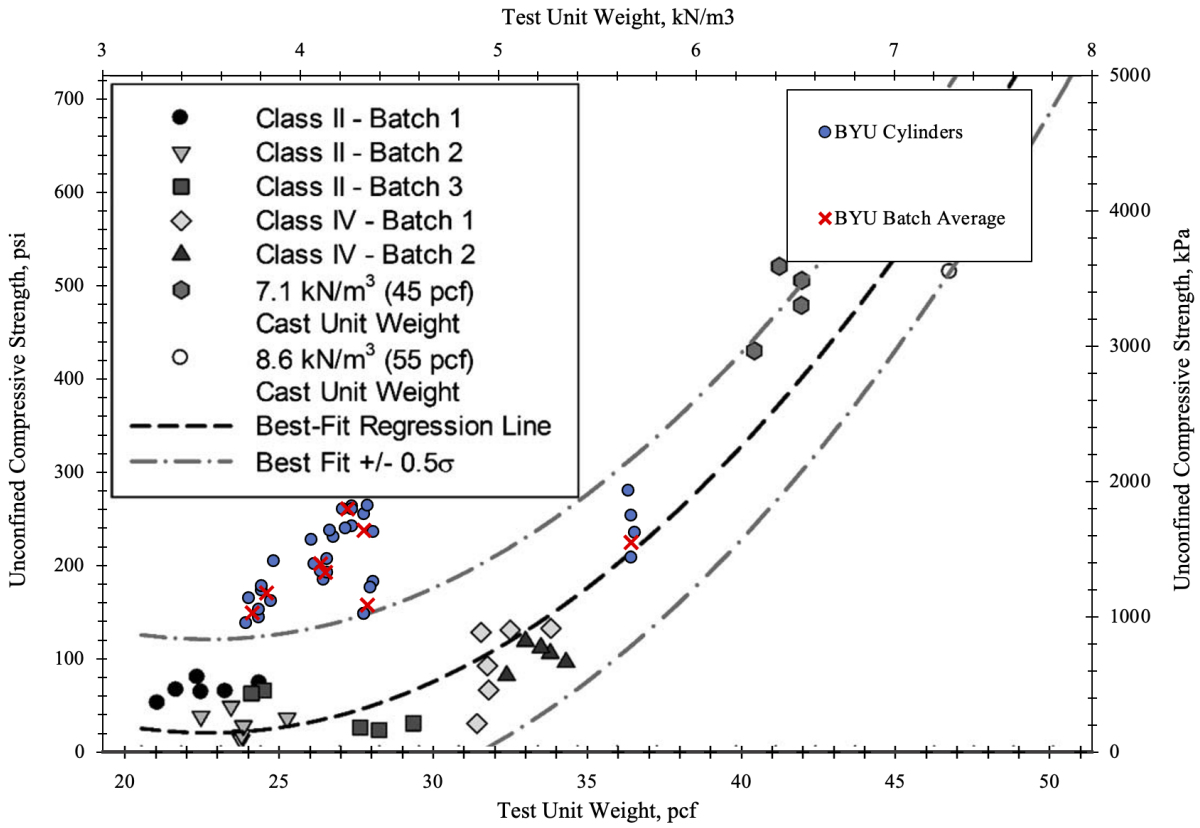

Figure 5-4: 28-day unconfined compressive strength data from BYU compared with 28-day results from Tiwari et al. (2017).

5.2.2 Material Density Analysis

Figure 5-5 compares the reported cast density of each cylinder with its measured (cured) density, measured and recorded at the time the UCS test was performed on the cylinder. Every cylinder had a higher density on test day than reported at the time of casting, but a lower density than reported after curing for 28 days.

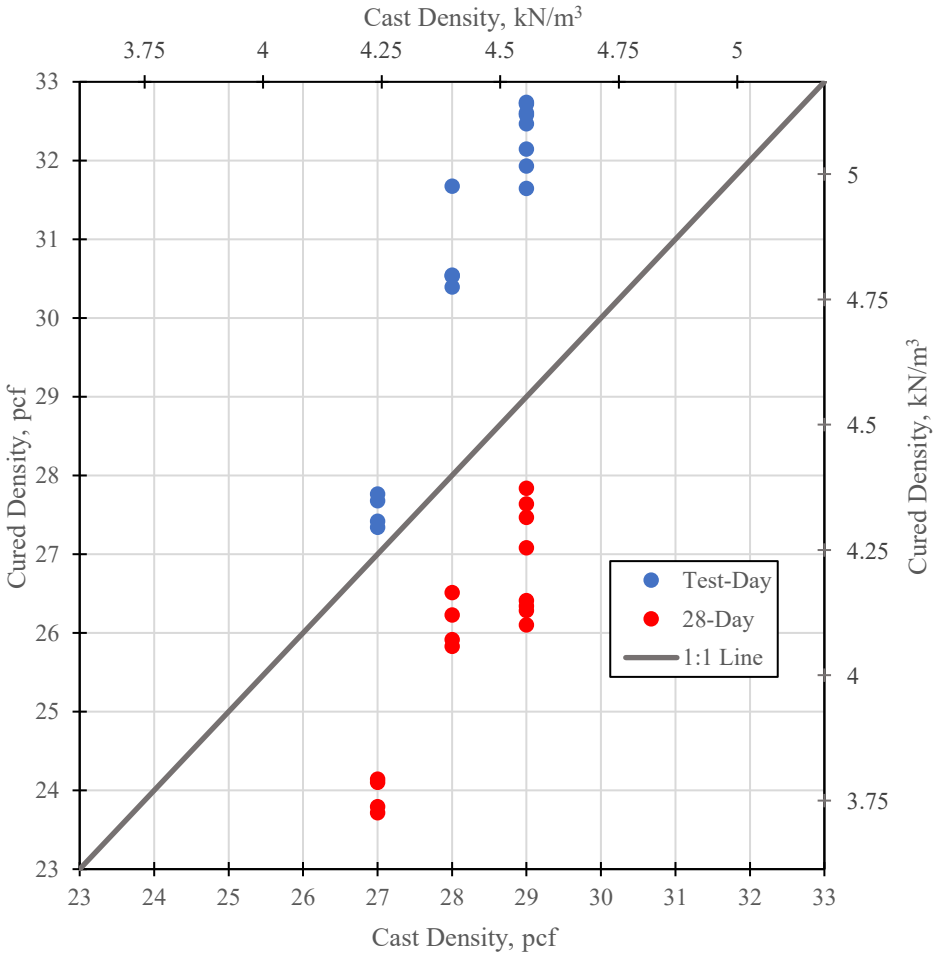

Figure 5-5: Cast density vs. cured density for sample cylinders on test-day and after 28-day cure time.

Water absorption and retention likely contributed to the unusually high densities found in many of the cylinders on test day, caused by their placement in a humid environment for 48 hours after an initial 24-hour cure time. After being removed from the humid environment, the cylinders were kept in a low-humidity environment for the remainder of the 28 days, which enabled any excess water in each cylinder to evaporate. The cylinder densities after 28 days were much nearer the target density of 27 pcf than they were on test day, which indicates that any residual water present in the cylinders on test-day evaporated before the 28-day tests were

performed. A few cylinders had densities far less than anticipated, but most were within 1 pcf of the target.

Errors in measuring the cast density likely caused the discrepancy between the cast and cured densities of each cylinder. After all the testing in this research was completed, the scale used by the contractors to determine the unit weight at the time of placement was found to only be accurate to ±10%. This extremely large margin of error could account for a large portion of the discrepancy seen between the cast and cure densities, though its exact effects cannot be determined. Because the contractor's scale was assumed to be accurate at the time of placement, no other density or unit weight measurements were taken.

Figure 5-6 shows the measured density and compressive strength of each cylinder compared to the target density and minimum 28-day strength. On test day, the cured densities were much higher than the target density range, but after 28 days, most cylinders fell back into the acceptable range. This further illustrates the effect that partial saturation may have had on the cylinders, whether the saturation was from residual bleed water or from the humid curing environment.

Figure 5-6 also demonstrates the tremendously high strengths achieved compared to the 28-day minimum strength of 40 psi. On test day, many of the cylinders had strengths approximately three times higher than the minimum 28-day strength; after 28 days, the strengths were between four and six times higher than the minimum. A lower water-cement ratio, a denser mix, and a humid curing environment are among plausible explanations for the strength increase but exploring the exact reasons for such an unexpected strength increase is beyond the scope of this research.

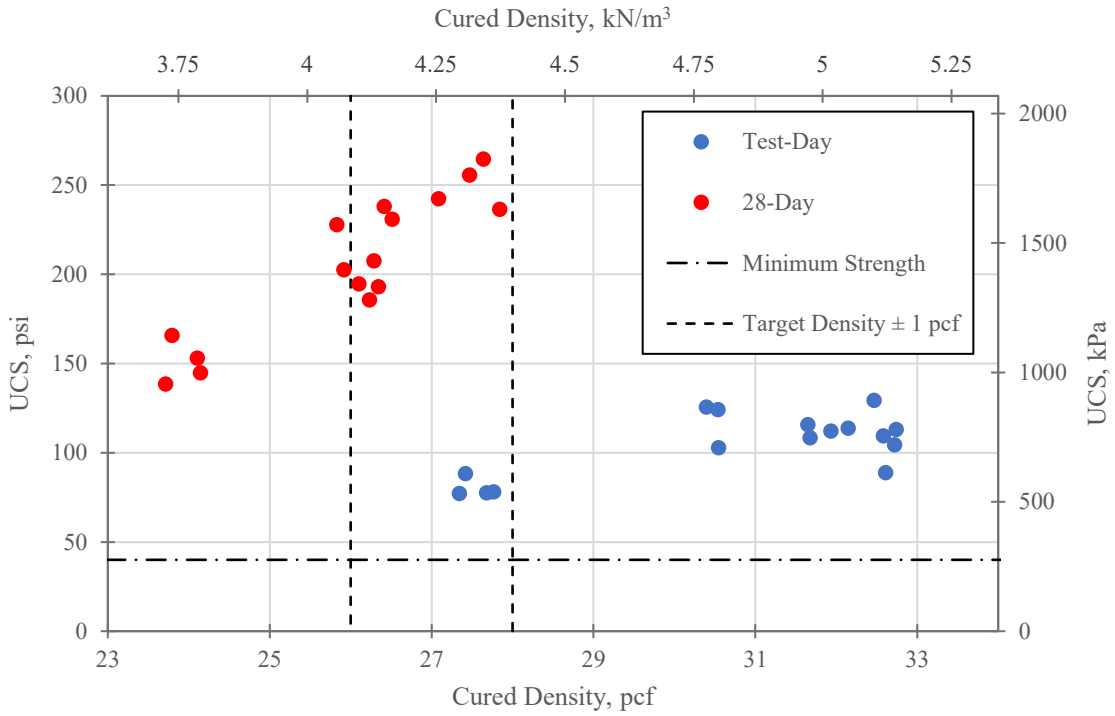

Figure 5-6: Cured density vs. UCS on test-day and after 28-day cure time

5.2.3 Triaxial and Direct Shear Testing

Isotropically Consolidated Undrained (CIU) and Isotropically Consolidated Drained (CID) tests were performed by GCI on samples of the LCC. Each test was run at confining stresses of 5, 25, and 50 psi. Tests were performed in general accordance with ASTM D7181. Four large direct shear tests were also performed at BYU with various confining pressures to model both the interface between lifts and the shear strength within a single lift (see Section 3.7.3).

The triaxial shear tests did not indicate any effect of confining pressure on shear strength. Instead, the maximum shear strength was approximately the same for each confining pressure. The maximum shear strength results of the triaxial and the direct shear tests are shown in Figure

5-7, relative to the estimated strength envelope suggested by Filz et al. (2015) and used by Remund (2017) and Wagstaff (2016) for tests on LCC and Controlled Low-Strength Material (CLSM), respectively. As suggested by Wagstaff (2016), a shear stress envelope has been included on the chart to represent a maximum shear strength of 35% of the unconfined compressive strength. The interface shear strengths approximately align with the 35% failure envelope, while the shear strengths of the solid direct shear test and the triaxial shear tests fall between the failure envelopes for 35% and 50% of the unconfined compressive strength.

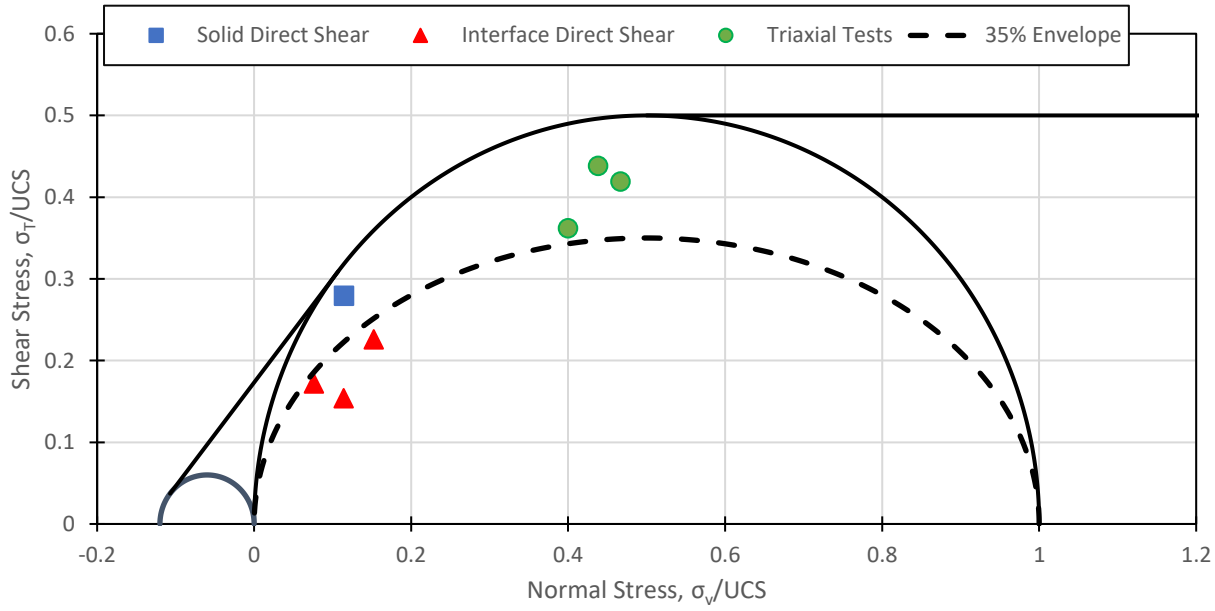

Figure 5-7: Triaxial and direct shear tests on proposed failure envelope

5.2.4 Strength vs. Time Curves

Figure 5-8 shows the UCS vs cure time for each sample cylinder tested in this research. An R^2 of 0.74 indicates that 74% percent of the variation in UCS is explained by time of curing,

while the rest of the variation is a result of other factors such as differences in unit weight as described previously.

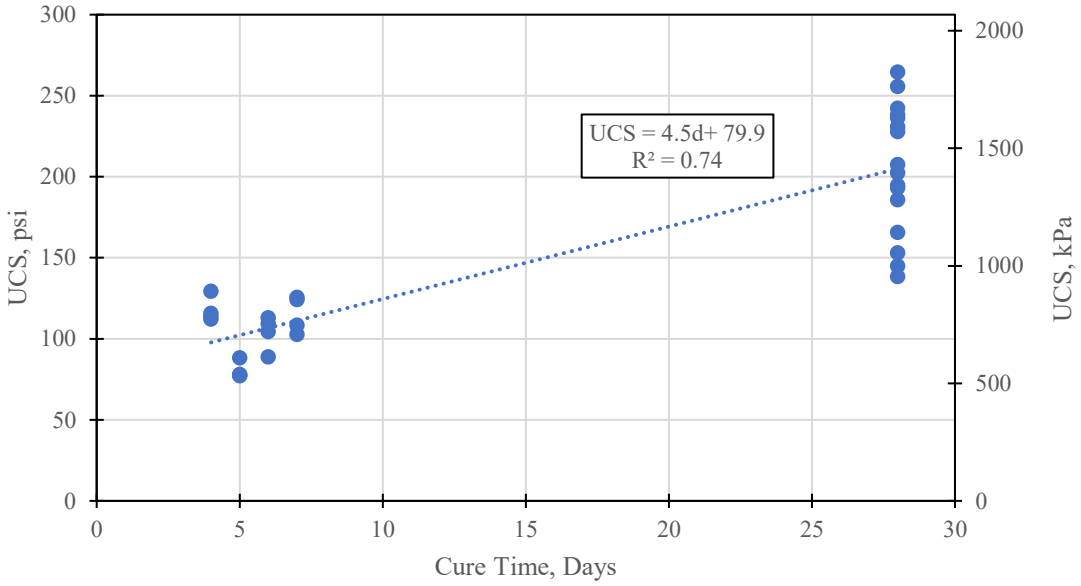

Figure 5-8: Cure time vs. UCS for individual sample cylinders

A further examination of the cylinder strength by comparing batches reveals a stronger trend. Using the average compressive strength of 4 cylinders from a batch is required in ASTM C495 so as to reduce the variability that inherently exists in the curing and casting process of each cylinder. After plotting the batch average cure time and compressive strength for each batch, an upward trend of strength versus time becomes apparent. Figure 5-9 shows the batch average compressive strengths as a function of cure time. All the batches increased in strength at a similar rate between test day and 28 days despite some batching having much higher or lower strengths than others.

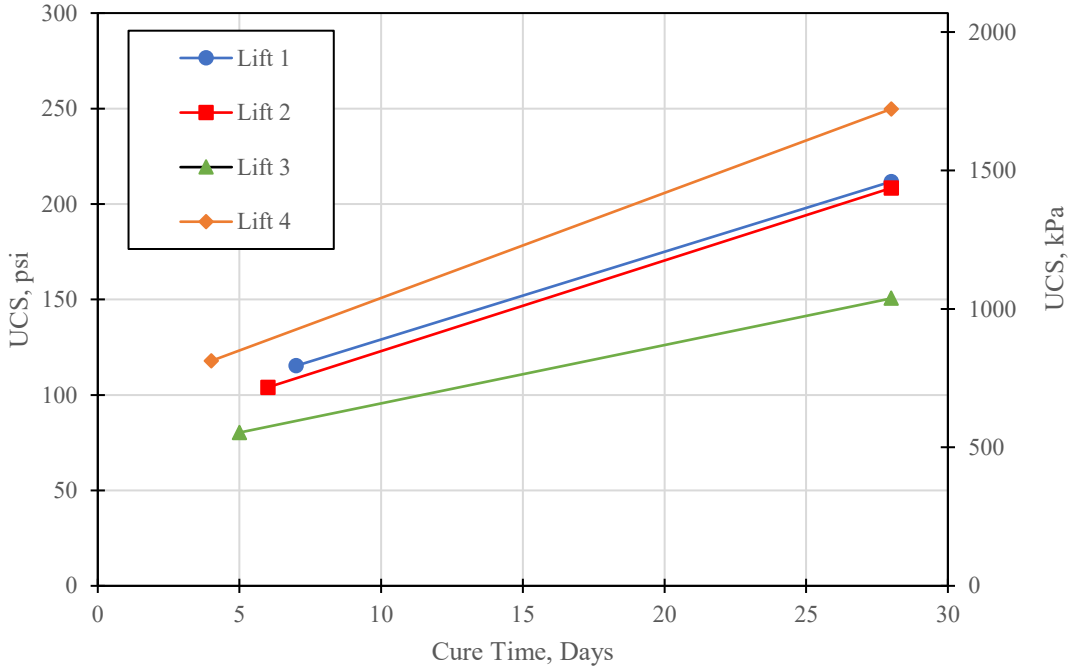

Figure 5-9: Cure time vs. UCS for batched sample cylinders

Because there is a large variation in both test-day and 28-day strengths, no accurate equation can be derived from this data to predict the strength of cellular concrete based solely on cast density; however, $UCS_{28-day} = 1.84UCS_{7-day}$ Equation 5-2 may be used to predict the 28-day strength of a cellular concrete batch based on the UCS after 7 days.

$$UCS_{28-day} = 1.84UCS_{7-day} \quad \text{Equation 5-2}$$

5.3 Behavior Analysis

Stress vs. displacement data was recorded during each of the UCS tests. The displacement values were divided by each individual cylinder height (measured prior to testing)

to obtain strain data for each cylinder. Batch average stress-strain data was obtained by averaging the strain measurements of each of the four cylinders in the batch at every stress interval.

The overall shape of the stress-strain curve for each cylinder batch changed between test day and 28 days. Figure 5-10 shows a comparison of the batch average stress-strain curves for each lift of cellular concrete on test day and after 28 days of cure time, while Table 5-4 shows tabulated data derived from these plots.

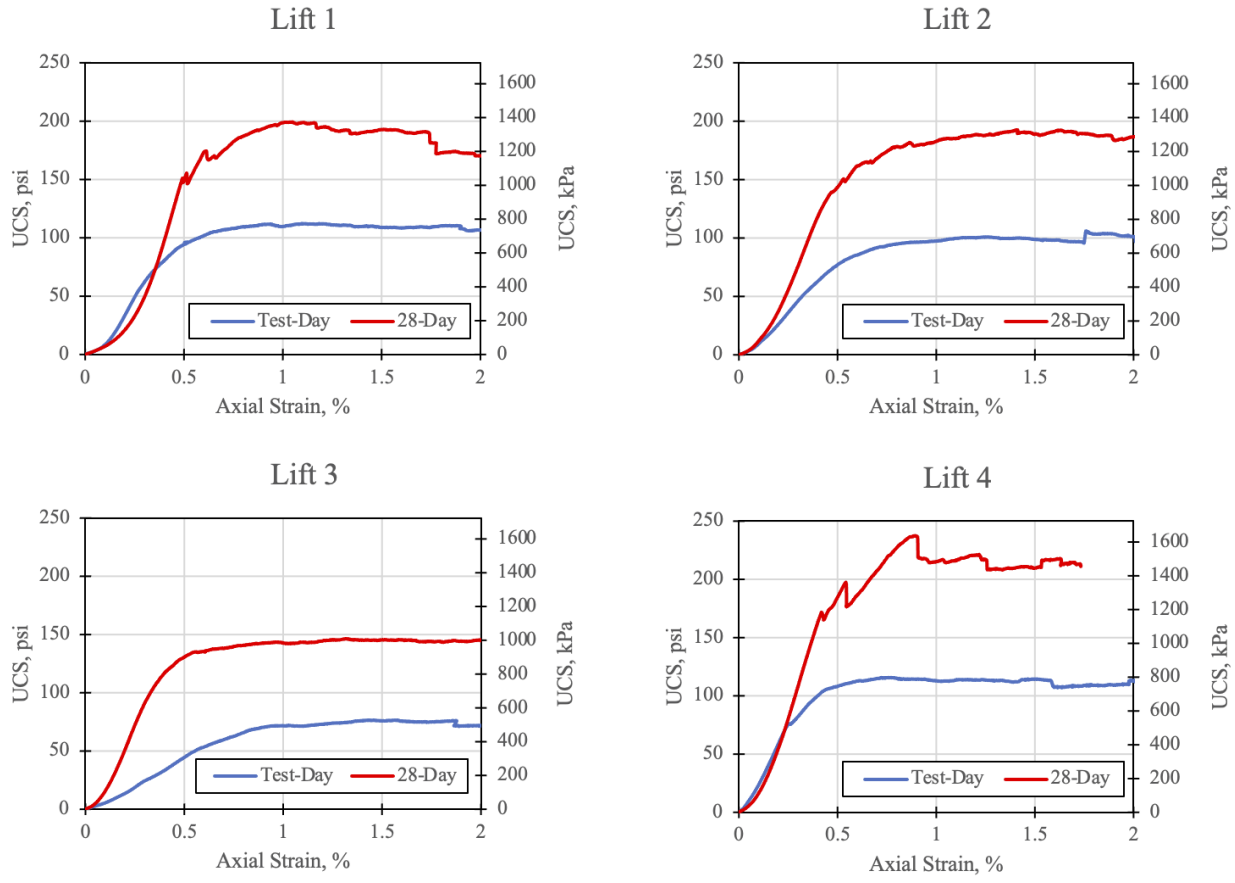

Figure 5-10: Comparison of batched stress-strain curves for cylinder samples on test-day and after 28-day cure time.

The modulus of elasticity (E) was calculated by computing the ratio of stress/strain within the linear region of each curve. Each cylinder exhibited some settlement upon initial loading before reaching a point of elastic deformation; however, this region of initial settlement was ignored in the elastic modulus calculation. The average strength of the cylinders nearly doubled between test day and 28 days, while the modulus of elasticity increased by an average factor of 2.75. Both strength and elastic modulus can influence the durability of a material but analyzing the effects of increasing strength and elastic modulus over time is outside the scope of this research.

Table 5-4: Tabulated data of observed material property changes over time

Lift	Cure Time, Days	Wet Density, pcf	Measured Density, pcf	Difference, pcf	UCS, psi	E, psi	Strain at UCS, %
1	7	28	30.8	2.8	120	21900	1.65
	28		26.1	-1.9	210	53400	1.2
2	6	29	32.7	3.7	100	16200	1.34
	28		26.3	-2.7	210	40200	0.88
3	5	27	27.6	0.6	80	9100	2.18
	28		23.9	-3.1	150	37900	2.39
4	4	29	32	3	120	26500	0.93
	28		27.5	-1.5	250	52300	0.8
Average	5.5	28.3	30.8	2.5	105	18400	1.53
	28		26.0	-2.3	205	46000	1.32

6 RCC (RETAINED-FACE) TEST RESULTS

The full-scale RCC active pressure test was performed in June 2020 following the placement of four consecutive successful lifts as described in Chapter 5. The test was performed by incrementally loading three of the six hydraulic jacks against the steel reaction frame to produce a relatively uniform surcharge pressure extending approximately 6'-0" away from the face of the RCC wall, as described in Section 3.4.3.2. The loading procedures used were also explained previously in Chapter 3. Chapter 6 will present the results of this test, while subsequent chapters will analyze the results and provide recommendations for design.

6.1 Applied Surcharge Load and Vertical Displacement

As shown in Figure 3-15, vertical displacement was measured using string potentiometers located at three points on each concrete surcharge beam during both the RCC and free-face tests. The total load applied to each beam was measured using load cells at the base of each hydraulic jack.

Though the exact forces on and deflections of all the beams are not identical, they are very close to each other. Table 6-1 shows the mean and standard deviation of the pressure applied to the LCC surface by each concrete surcharge beam at various levels of surcharge. The ratio of the standard deviation to the mean is very small (less than 8% in general) and gets

smaller with increasing load. Because this ratio is very small, it can be assumed that the surcharge applied to the top of the cellular concrete block is approximately uniform.

Table 6-1: Mean, standard deviation, and coefficient of variation for pressure applied by concrete surcharge beams to the LCC block surface at various surcharge levels.

Mean Surcharge, psi (kPa)	Std. Dev. (σ), psi (kPa)	σ/Mean, %
5.2 (36)	0.4 (2.9)	8.1%
11.5 (80)	0.9 (6.5)	8.2%
17 (117)	1.2 (8.3)	7.1%
22.2 (153)	1.3 (8.9)	5.8%
27.8 (192)	1.3 (9.2)	4.8%
35.8 (247)	1.4 (9.8)	4.0%
41.7 (287)	1.5 (10.3)	3.6%
48.6 (335)	1.3 (8.8)	2.6%
52.8 (364)	0.8 (5.2)	1.4%
56.3 (388)	0.7 (5)	1.3%
59 (407)	0.8 (5.8)	1.4%

6.1.1 Surcharge Stress vs. Axial Strain Behavior

Figure 6-1 shows the relationship between axial strain and applied surcharge pressure throughout the test for each of the three surcharge beams. In addition, the average surcharge pressure vs strain curve is plotted for comparison. Axial strain was computed by dividing the average deflection of each beam by the height of the LCC block (10 ft).

Beam 1 (immediately adjacent to the RCC wall) consistently had higher displacement than beams 2 or 3, and beam 3 had the lowest strain at every surcharge. As the RCC wall rotates away from the cellular concrete block, some horizontal expansion must occur within the LCC to

maintain contact between the wall and the cellular concrete. The material beneath beam 1, closest to the retaining wall, must expand horizontally to fill this void, causing slightly higher axial strain at a given surcharge. Beam 3 was immediately adjacent to the induced shear plane approximately 6'-0" from the face of the RCC wall. It is reasonable to expect lower vertical displacement from this beam than the others because the friction and cohesion at the shear plane adds stiffness and strength.

The average stress-strain curve in Figure 6-1 shows the axial strain increasing rapidly with little to no increase in surcharge once the pressure reached approximately 58 psi. This flattening of the curve indicates that the LCC began to fail, but because the applied surcharge never decreased, the failure was not catastrophic.

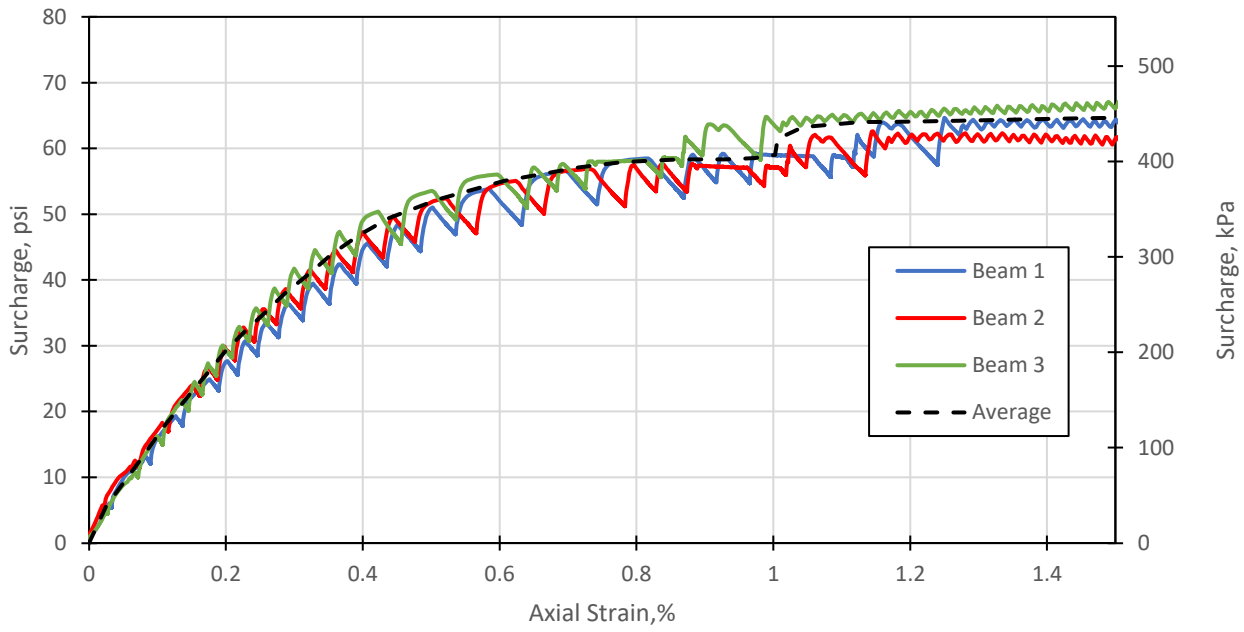

Figure 6-1: Axial stress vs. strain of LCC surface beneath each surcharge beam in the RCC retained-face test.

The hydraulic jacks were loaded in increments as described in Section 3.7 throughout this test. Once the target load for each increment was achieved, the hydraulic pump supplying the fluid to the jacks was locked for the holding period of 3 minutes. During each holding period, the LCC surface slowly crept under the applied load. The slight displacement of the LCC surface led to a slight expansion of each hydraulic jack cylinder, which caused a decrease in overall hydraulic pressure and thereby a decrease in total surcharge pressure. This effect is clearly seen in Figure 6-1, where the stress-strain curve for each individual beam is staggered. The peaks of each line correspond to the end of each loading increment, while the troughs correspond to the end of each holding period. The average stress-strain line shown in the figure above was created by averaging the stress-strain curves of each beam, using only the peaks of each line as data points.

Loading only three of the six concrete surcharge beams produced a shear plane in the LCC as desired. The surface of the LCC did not remain smooth throughout the test, and a shear plane clearly formed at the boundary of the surcharge beams. Figure 6-2 shows an image obtained from a point-cloud model of the cellular concrete surface after all testing was complete and the surcharge beams and reaction frame walls were removed, while Figure 6-3 shows a measurement of the displacement between the low and high surfaces of the LCC at the main shear plane. The relative displacement between surfaces was nearly uniform along the surface, averaging approximately 3 inches (7.5 cm). Small cracks developed between each of the six surcharge beams in both the RCC and free-face tests, so each beam's approximate location can be clearly identified on the image.

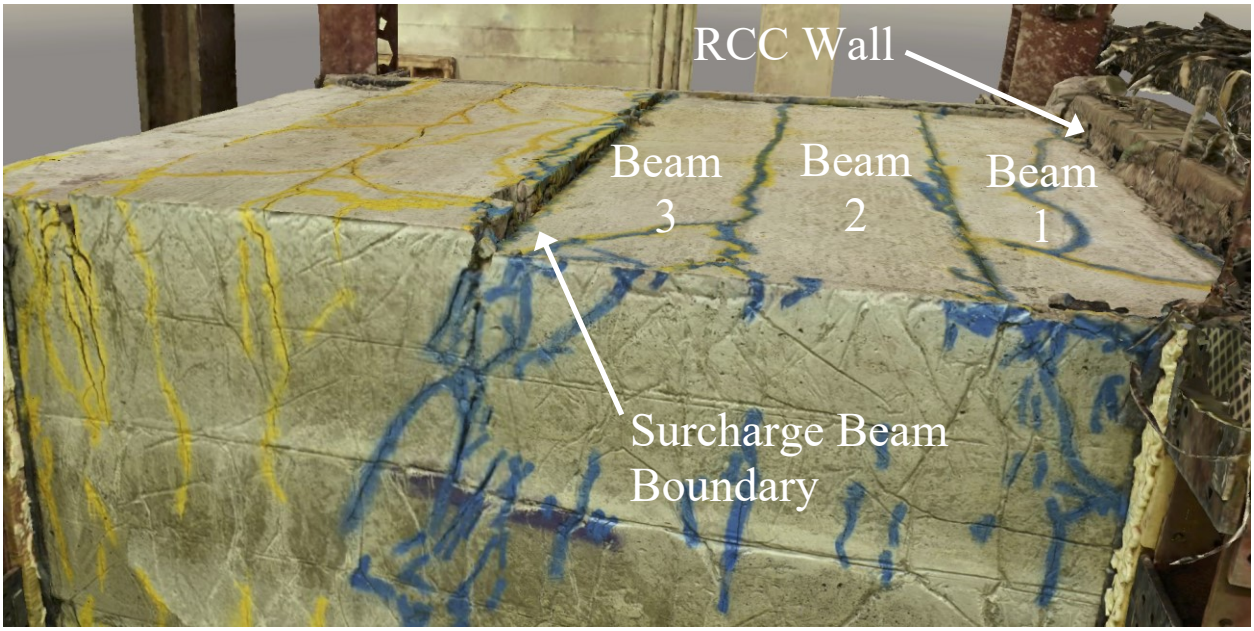

Figure 6-2: LCC block surface after the reaction frame walls and concrete surcharge beams were removed, with approximate surcharge beam and other significant locations labeled

Figure 6-3: Measurement of the vertical displacement at the boundary of the surcharge beams at 6 ft behind the RCC wall

6.1.2 Elastic Modulus and Yield Point

Figure 6-4 shows the measured average surcharge stress versus average axial strain for the RCC test. Although the curve exhibits a relatively linear initial slope (elastic modulus), like many composite materials, cellular concrete does not usually exhibit a clear yield point. To estimate the yield point, the 0.2% offset method can be used where the best-fit regression line based on the initial elastic stress-strain curve is shifted by a strain of 0.2% to the right. The intersection with the measured stress-strain curve then defines the yield stress or yield point. Figure 6-4 shows both the estimated modulus of elasticity line and the 0.2% offset line relative to the average compressive stress vs. axial strain line for the RCC retained-face test. The vertical strain at yield in the RCC retained-face test was approximately 0.62%, with a yield stress of 51.5 psi (351 kPa).

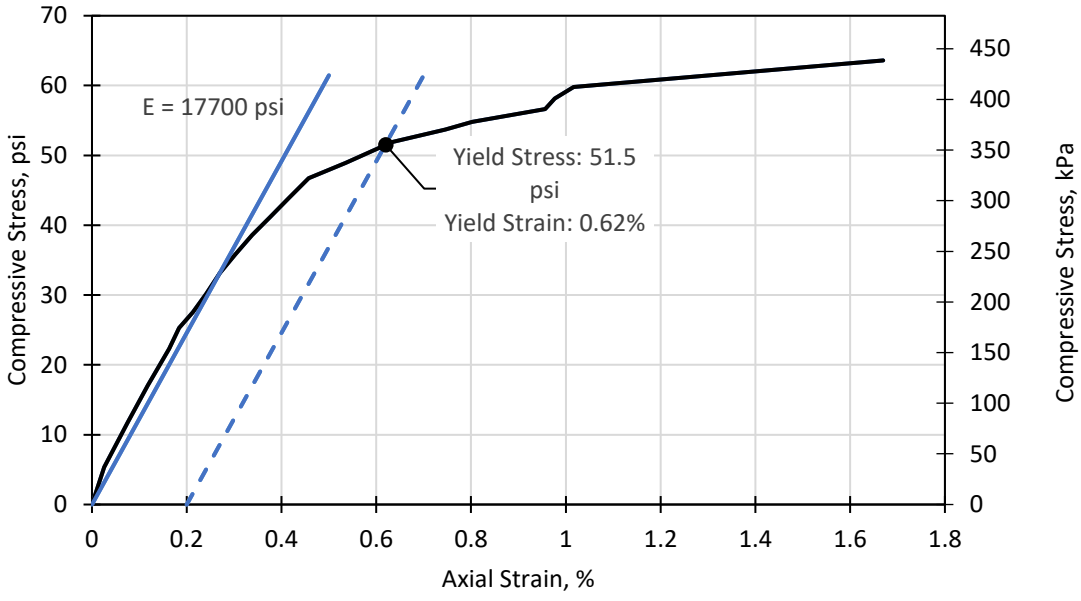

Figure 6-4: Compressive stress vs. axial strain for the RCC test analyzed using the 0.2% offset method

To provide some context, the test sample cylinders had an average yield stress of 92 psi (634 kPa) at the time of the RCC test. The yield stress for the large LCC block was significantly lower than the average cylinder yield stress, indicating that the governing failure mode in the RCC test was likely shear, or a combination of shear and compression, rather than pure compression. This result indicates that exclusive reliance on the unconfined compression test to characterize the strength of an LCC backfill is not always appropriate.

6.1.3 Comparison to Sample Cylinders

To compare the stress-strain curve of the full LCC block in the RCC test with the behavior of the sample cylinders, an anticipated stress-strain curve for the LCC block, based on the UCS tests performed on all four batches of sample cylinders, was generated. The anticipated stress at any given strain was calculated using the equation

$$\sigma_{average} = \frac{H}{\frac{h_i}{\sigma_i}+\frac{h_{i+1}}{\sigma_{i+1}}+\ldots+\frac{h_n}{\sigma_n}} \qquad \text{Equation 6-1}$$

where H = total LCC block height (10 ft), h = individual lift height corresponding to each sample cylinder batch (approximately 2.5’ per lift), and σ_i = stress applied to the sample cylinder at a given strain point. The anticipated stress was calculated at strain increments of 0.01% to create a full stress-strain curve rather than just a maximum anticipated strength. Equation 6-1 produces a harmonic mean, which tends to skew the average toward the lower-strength material. This equation was chosen over a simple arithmetic mean to account for the possibility of weak layers within the LCC block.

Figure 6-5 shows the harmonic mean stress-strain curve compared to the stress-strain curve generated in the RCC test. Typically, the stress-strain curve in the RCC test is only about 67% of the anticipated curve based on the UCS tests performed on the sample cylinders. Even with the downward skew and the lack of a correction factor for the low height-to-width ratio of the LCC block, the anticipated stress-strain curve predicts significantly higher stresses than were measured. This further indicates that the failure of the LCC block in the RCC test was not a pure compression failure like the cylinders, but rather a shear or combined shear/compression failure.

Both the measured and anticipated stress-strain curves show the ultimate stress being reached at a strain of approximately 1%, but the strain at the yield point is much lower in the measured test than in the anticipated test. This is likely due to the difference in the failure mechanism, where the anticipated curve represents a pure compression failure and the measured curve represents a shear or combined shear/compression failure.

In the preliminary test described in Chapter 4, the average UCS from the sample cylinders was lower than the surcharge pressure applied to the surface of the uniformly-loaded LCC block; nevertheless, there was little movement of the RCC wall or distress seen in the LCC block. The LCC had a higher overall strength in the RCC retained-face configuration because the confining walls of the reaction frame and the RCC wall added to the overall compressive strength of the material.

In the test described in this chapter, the LCC block had a much lower ultimate strength than the average UCS of the sample cylinders despite the presence of the same confining walls. In addition, the test in this chapter was performed on a material with a UCS that was more than twice that of the material described in Chapter 4. This comparison clearly demonstrates that a shear or combined shear/compression failure, rather than a pure compression failure, is a more

critical loading scenario for structural stability. LCC backfill should be designed based on shear strength rather than unconfined compressive strength to ensure adequate performance.

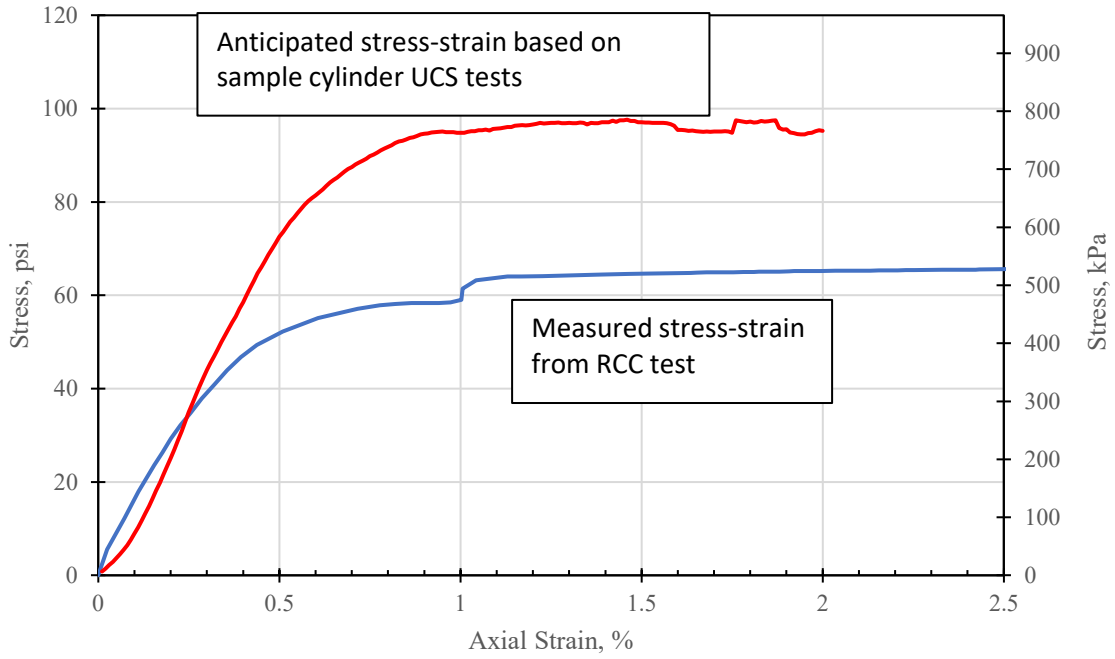

Figure 6-5: Harmonic mean of the unconfined stress-strain curves of sample cylinders compared to the large-scale LCC block in the RCC retained-face test.

6.2 Surcharge Pressure Effects on Horizontal Displacement

String potentiometers were used to measure the horizontal displacement of the steel frame and wood test box walls in several locations. Because the validity of the test depends greatly on accurately modeling a plane-strain condition with movement primarily occurring in the direction of the RCC wall and not in the transverse direction, a summary of the displacement results and analyses will be presented in this section.

The walls and columns of the frame were anchored to the structural concrete laboratory floor by post-tensioned steel anchors tied directly to the floor of the structures lab. The anchors consisted of 1.5” diameter 100-ksi steel bars with 9” steel plate washer plates above and below the structural floor, extending through the floor by way of 2” diameter holes spaced every 36” in each direction. The bars were post-tensioned to a tensile stress of 10 ksi to ensure there would be no movement of the anchors when they were loaded. The anchors were also loaded horizontally with respect to the floor during installation to ensure the rod could not slide horizontally inside the hole within the floor during the test.

6.2.1 Wood Wall Panels

The walls of the test box were constructed with wood wall panels (2x4 studs spaced at 12” on center, faced with ¾” OSB sheathing) braced by horizontal steel beams spaced 30” apart in the vertical direction (see Section 3.4.1). Some settling of the wood studs against the steel beams was expected as the cellular concrete expanded horizontally because every stud did not sit perfectly flush against the steel beams. Wood shims were inserted in the gap between the steel beams and wood walls as necessary to make it as flush as possible, but construction limitations were such that some settling was still likely to occur. Some settling of the bolted connections at the steel beams was also expected. None of the steel connections were designed as slip-critical connections, and all holes were drilled 1/8” larger than the diameter of the bolt to aid in the construction process. Based on construction limitations, a deflection of approximately 1/8” was expected at each wall as both the wall and beam connections settled.

The wall panel deflections were measured at the midway point between bracing beams, the point where the expected movement was highest. The wall panel on the south side of the reaction frame deflected more than any of the other wall panels, with a maximum of 0.25 inches

of deflection at the most extreme point. At the measurement location between 6 and 7 feet above the ground surface, the recorded settlement was very large, but at the rest of the measured locations, the deflection was close to that of the steel beams along the South side. This deflection was likely due to the wood panel settling against the steel beams because the movement of the steel beams was minimal. Between 55 psi and 58 psi, a sudden increase occurred in the deflection of a beam on the North side of the frame—the other two beams on the North side saw no such increase. This is indicative of a bolted connection slipping. The wood wall panels deflected approximately the same amount as the beams on the North side excepting this connection slip.

Figure 6-6 and Figure 6-7 show the total deflection of the full wall system on the North/South sides of the frame and the total deflection of a mid-height steel beam on the North/South sides, respectively.

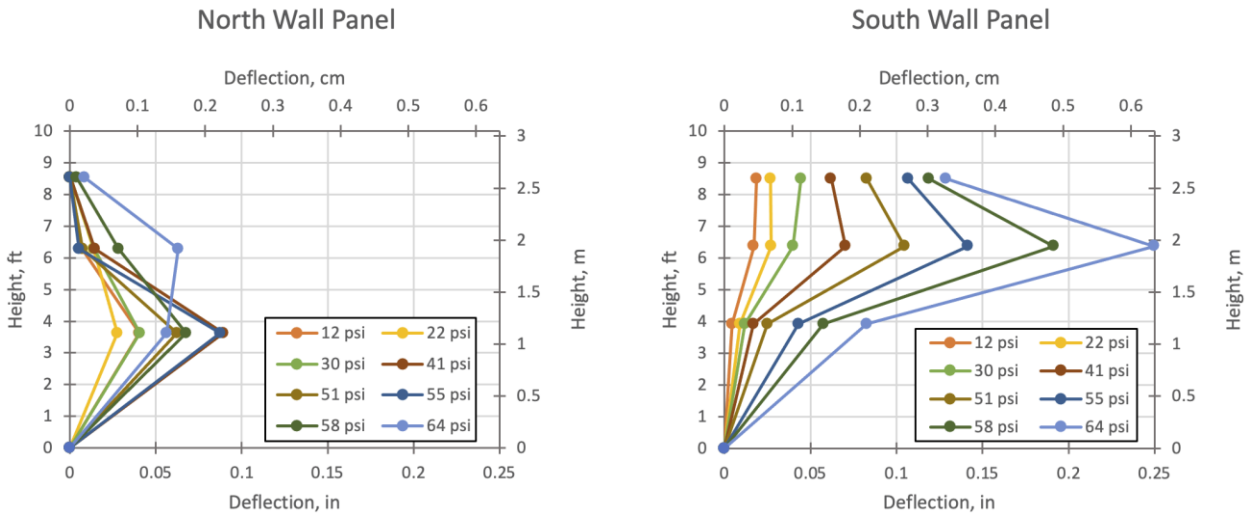

Figure 6-6: Deflection of the wood wall panels at various surcharges

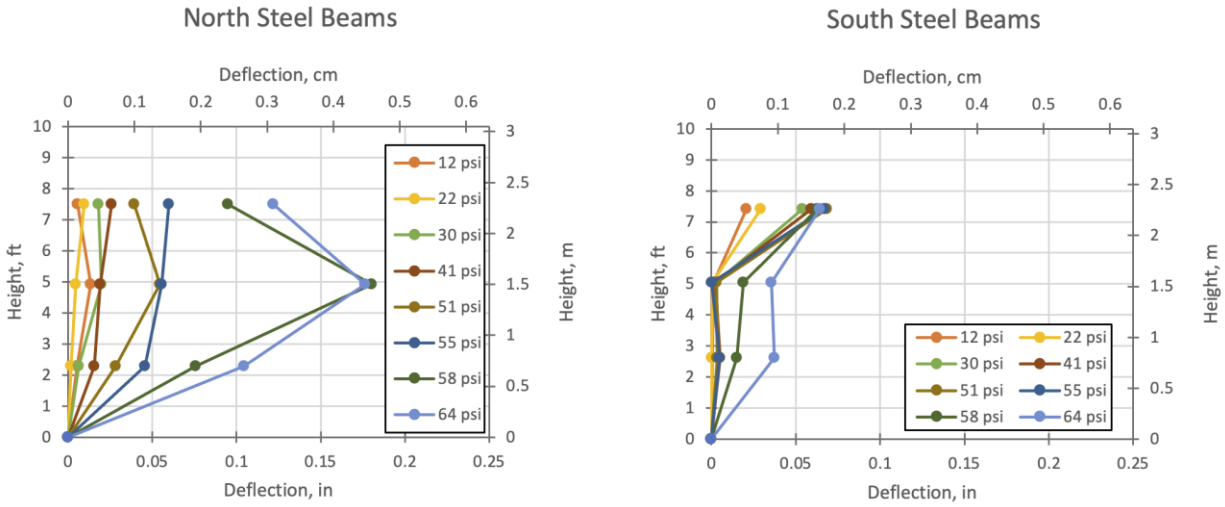

Figure 6-7: Deflection of the steel reaction frame beams at various surcharge levels

The deflection of the wood wall panels was very small—less than 10% of the total vertical deflection of the LCC block, and approximately 13% of the horizontal deflection of the retaining wall. Although the wood wall panels were not perfectly rigid, the deflection ratio of the wall panels to the RCC wall was small enough relative to approximate the plane strain condition.

The maximum deflection measured on the wood wall panel located on the East side of the frame (opposite the RCC wall) was 0.07 inches (1.8 mm). The measurements for this wall are not shown in Figure 6-6 and Figure 6-7 because the movement is negligible compared to the deflection of the North and South walls.

6.3 Horizontal Pressures

Horizontal pressures acting on the retaining wall were measured with a series of six pressure plates embedded flush with the face of the RCC retaining wall. The pressures recorded

on each plate are presented in Figure 6-8 as a function of applied surcharge pressure. The depth of each plate relative to the surface of the LCC block is shown on this figure.

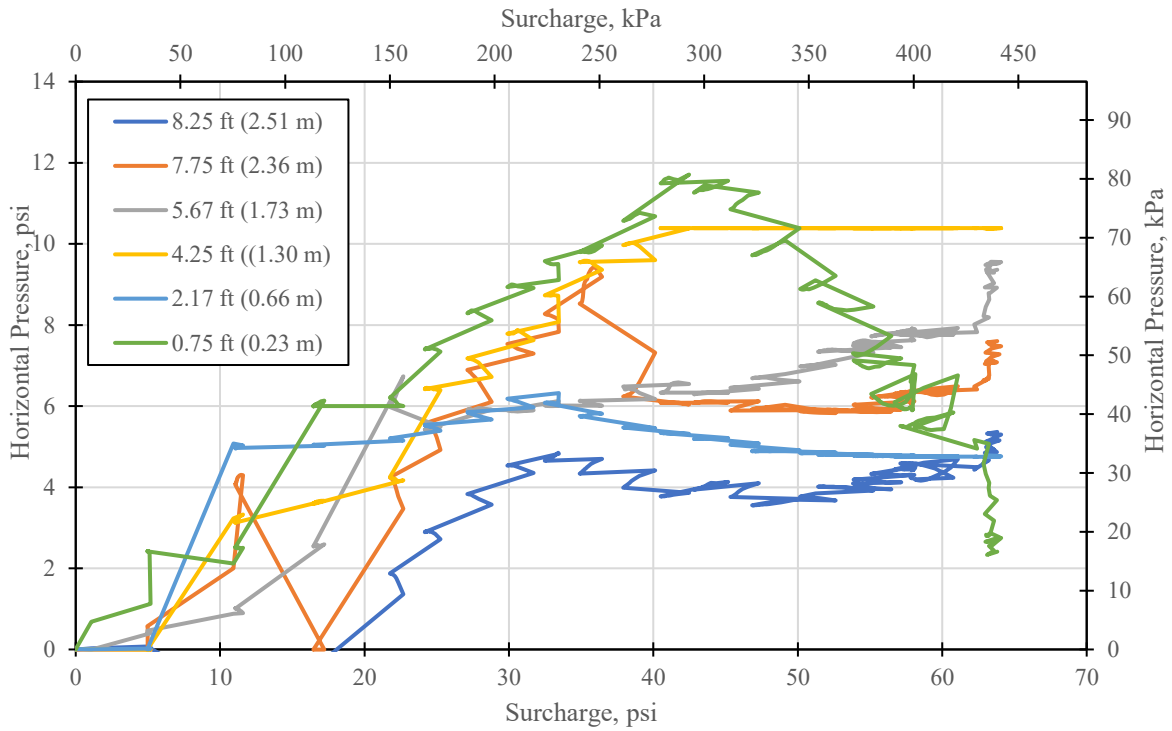

Figure 6-8: Measured horizontal pressures at the RCC wall face vs. applied vertical surcharge

An overview of the measured horizontal pressure from the pressure plates on the RCC stem wall is presented in Figure 6-9. This figure shows several curves plotting the measured horizontal pressure as a function of depth at selected levels of vertical surcharge. The pressure on the wall gradually increased as the surcharge pressure increased up to a surcharge pressure of about 27 psi; the rate of increase slowed dramatically once the surcharge pressure exceeded about 27 psi. At the maximum surcharge of 63 psi, the measured pressure at the top of the wall was about 25% of its peak value.

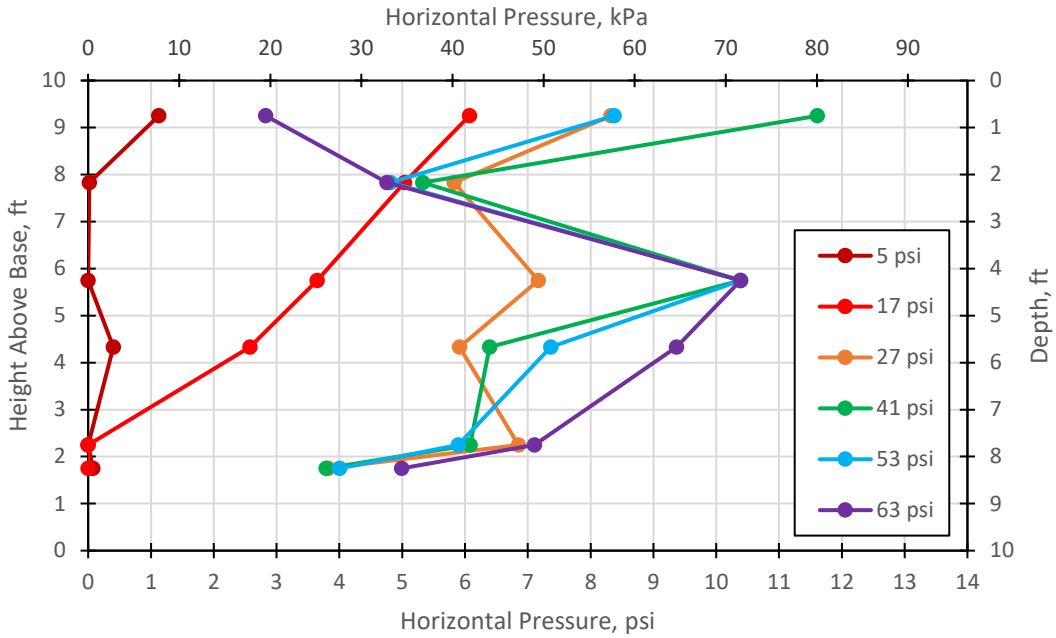

Figure 6-9: Horizontal pressures on the RCC wall as measured by Geokon pressure plates at selected levels of vertical surcharge

6.3.1 Horizontal Pressure vs. Movement

A prominent trend seen in this data is that of decreasing pressure near the surface of the LCC as the surcharge increases past 40 psi. At a surcharge of approximately 40 psi, the pressure plate nearest the top of the wall appears to reach its maximum load. The decrease in horizontal pressure at the top of the wall with increasing vertical surcharge indicates that the steel reinforcement in the RCC retaining wall yielded and allowed the wall to rotate outward and away from the LCC. It also indicates that the LCC remained a cohesive block rather than crumbling and filling the void created by the wall displacement. The plates located at depths of 7.75 and 5.67 feet record somewhat consistent pressures as the RCC wall rotated. This indicates that the LCC block bulged outward to maintain contact with the wall, but not with sufficient force to increase the pressure on the wall at these locations.

Because the RCC wall had a finite strength, it was expected that the total force applied to this wall would have a limit before the wall ultimately failed. Once the horizontal force exerted by the LCC was sufficient to exceed the strength of the retaining wall, the wall was expected to displace without any significant increase in applied force, similar to the behavior of a steel rod after reaching its yield strength in tension.

According to Rankine's equation for active earth pressure (Equation 2-3), all horizontal pressure developed within the LCC block must be resisted by a combination of material cohesion and external forces. If the total horizontal force resisted by the material cohesion is modeled as a linear spring, displacement of the RCC wall (with constant confining force) would force the material cohesion to resist more of the horizontal force until the whole system reached a point of equilibrium. With each degree of additional vertical surcharge, the RCC wall displacement and horizontal expansion of the LCC would work together to equilibrate the horizontal forces until the cohesive structure of the cellular concrete broke down and the entire system reached a point of ultimate failure. The yielding of the wall and the decrease in pressures measured near the top of the wall suggest that equilibrium of the horizontal forces was reached repeatedly but the cohesive structure of the LCC was never destroyed, and thus ultimate failure of the material was not reached.

Figure 6-10 presents the average horizontal pressure applied to the RCC wall compared to the measured pressures shown previously in Figure 6-8. The average pressure was calculated by weighting the pressure measured by each plate according to its area of influence, which accounts for the inconsistent vertical spacing between plates. As expected, the average pressure applied to the wall hit a maximum level and stayed at approximately that level throughout the yielding of the retaining wall. The average pressure ceased to increase linearly at a surcharge of

35 psi, which is approximately the point where the wall began to yield. Additional discussion on this point is provided in Section 6.5.

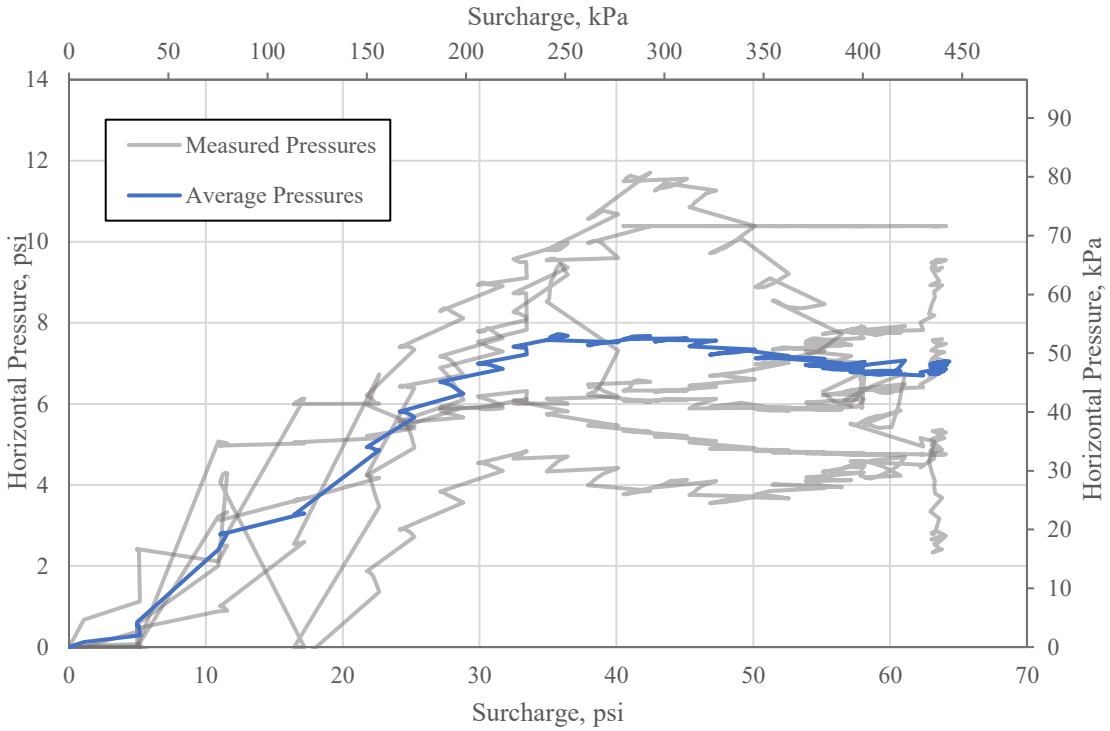

Figure 6-10: Average horizontal pressure at the RCC wall vs. applied vertical surcharge

6.3.2 Measured Active Pressure Coefficient

The active pressure on a structure retaining a cohesive backfill with a friction angle greater than 0 can be estimated using Equation 2-3, Rankine's active earth pressure equation modified for cohesive fill. Assuming a constant cohesion, depth and density, this equation may be re-written as

$$\sigma_H = C_1 + C_2 K_a - C_3 \qquad \text{Equation 6-2}$$

where $C_1 = \gamma z\, K_a$, $C_2 = q$, and $C_3 = 2c(K_a)^{0.5}$. This can be further simplified to the equation

$$\sigma_H = a + bK_a \qquad \text{Equation 6-3}$$

where $a = C_1 - C_3$ and $b = q$. This simplified equation is a linear function of K_a, with the assumption that σ_H may never be less than 0. An estimate for the value of K_a may be obtained graphically from the measured pressures by calculating the slope of linear best-fit lines for each pressure plate. Figure 6-11 shows best-fit lines drawn for each plate along the region where the horizontal pressure increases linearly as the surcharge load increases. While there is some variation, the slopes for the various plates show reasonably good consistency.

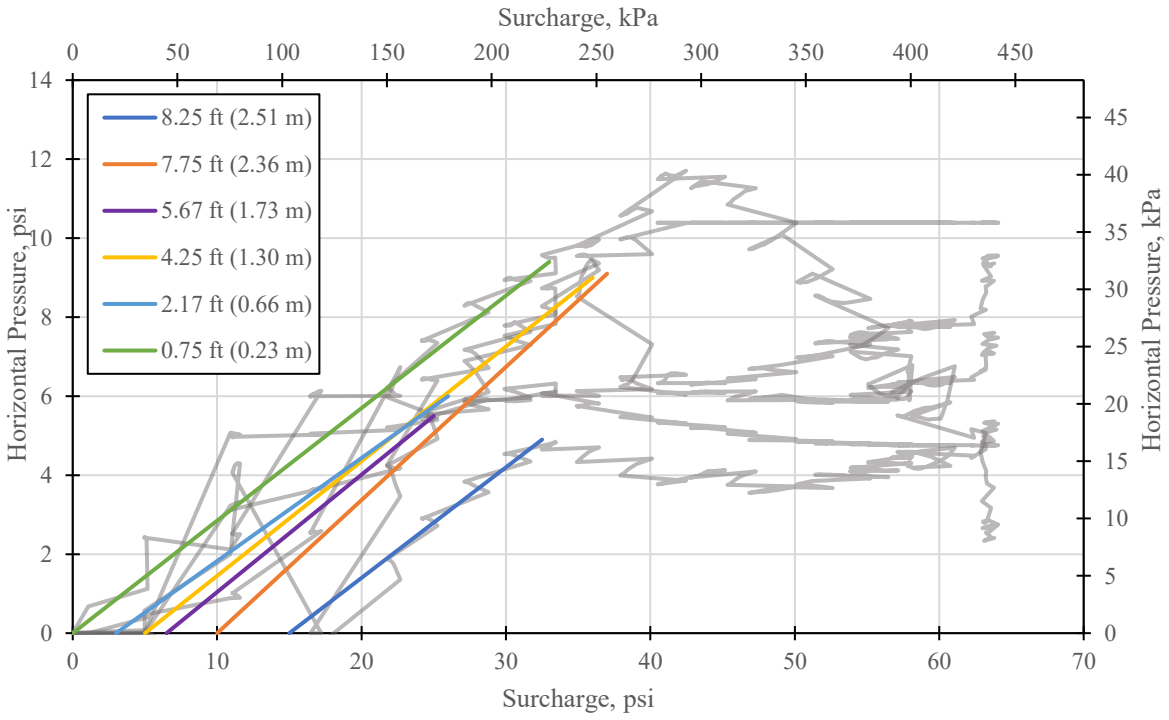

Figure 6-11: Graphical analysis of Rankine's active pressure coefficient

Table 6-2 summarizes the calculations for friction angle and active pressure coefficient, K_a, at each of the six measurement points along the RCC wall, using the graphical analysis method described above. Very good agreement exists among the different measurements for the active earth pressure coefficient K_a. The friction angle measured at a depth of 7.75 ft is lower than all the others, but the average friction angle is very close to the anticipated friction angle of 34º with an average K_a of about 0.3. The difference in K_a calculated using friction angles of 33.3º and 34º is 0.011, or about 4%, which is not large enough to suggest that the friction angle is not 34º. An angle of 34º will be used in all analyses in this report.

Table 6-2: Active pressure coefficient, friction angle, and cohesion values calculated from pressure plate measurements.

Plate Depth, ft	K_a	Friction Angle, degrees
8.25	0.280	34.2
7.75	0.337	29.7
5.67	0.297	32.8
4.25	0.290	33.4
2.17	0.261	35.9
0.75	0.285	33.8
Average	0.292	33.3

6.3.3 Measured Cohesion

Cohesion can be calculated using the maximum applied surcharge and the maximum horizontal pressure measured on the RCC wall with a known active pressure coefficient, K_a. Equation 6-4, an algebraic simplification of Equation 2-3, can be used to calculate the true cohesion of the LCC.

$$\sigma_h = C_1 + C_2 - c * C_3$$ Equation 6-4

In this equation, $C_1 = \gamma z$, $C_2 = qK_a$, $C_3 = 2K_a^{0.5}$, σ_h is equal to the maximum uniform pressure exerted on the RCC wall (7.6 psi), q is equal to the maximum applied surcharge at the point of ultimate failure (64 psi). Solving this equation for "c" using a friction angle of 34º (K_a = 0.283) results in an estimated cohesion of 1460 psf (69.8 kPa).

Previous research suggests that the cohesion of Class II LCC after 28 days of cure time is between 700 and 1600 psf, while the strength is approximately 100-150 psi (Tiwari et al., 2017). Though the LCC used in the RCC test had only cured for 7 days, its average strength of 105 psi and cohesion of 1460 psf fit the expected range for 28-day cured material very well. The reasons for the early strength gain are unknown, but the results of the RCC test indicate that the material used is very similar to standard LCC after a full 28-day cure.

6.3.4 At-Rest Cohesion Observations

Active pressure is developed within a backfill only after movement of the retaining structure. Typically, movement of H/1000 (where H = height of the retained backfill) at the top of the retaining structure is required to develop active pressure within dense granular backfill, while movement of H/100 is required within stiff clay backfill. Because LCC behaves in a similar manner to both stiff clay and dense sand, it is likely that the required deflection to create an active pressure condition within LCC is between H/1000 and H/100, or between 0.12 and 1.2 inches; however, determining the exact movement ratio required to develop active pressure within LCC is outside the scope of this research.

The RCC wall began to yield at a surcharge of approximately 34 psi—a more thorough investigation of the yield point is presented in Section 6.5, but the approximate surcharge and

deflection at the yield point is sufficient information for the purposes of the analysis in this section. At the yield point, the total deflection at the top of the RCC wall was 0.11 inches (0.28 cm), or H/1100. This is likely insufficient movement to develop active pressure. Near the end of the test when the RCC wall had deflected by 2 inches (5.1 cm), the deflection ratio reached H/60. Because the deflection ratio at the end of the test was greater than the maximum anticipated deflection bound of H/100, it is very likely that active pressure was developed at some point between the yielding of the retaining wall and the end of the test.

Using Equation 2-3 and the cohesion and active pressure coefficient (K_a) specified in Section 6.3.3, pressure would not be expected to develop on the wall until a surcharge of approximately 37.2 psi (256.5 kPa) was applied if the conditions for active pressure were met. Because the wall yielded before this load was reached, which required a sizeable uniform pressure, the estimated cohesion of 1460 psf is clearly not applicable for the at-rest condition.

The at-rest pressure condition likely dominated the behavior of the LCC up to the wall yield point. In this state, the cohesion of the material is rendered ultimately ineffective because the material has insufficient space to expand; however, in the active pressure condition, the cohesion can be fully activated as the material expands to fill the void left in the wake of the retaining structure. The transition between the at-rest and active pressure states allowed the activation of the material cohesion, which enabled the LCC backfill to support increasing surcharge even after the RCC wall yielded and ceased to offer increasing resistance.

The effective at-rest cohesion can be calculated from the measured horizontal pressures using Equation 6-4, where $\sigma_h = 0$, q = applied surcharge required to register horizontal pressure, and $K_a = 0.283$. Averaging the effective cohesion calculated at every measurement location results in an average cohesion of 295 psf (14.1 kPa), approximately 20% of the active-pressure

cohesion. Figure 6-12 shows the calculated cohesion values at each measurement location as a function of depth. A linear trend is apparent in these calculated values. Equation 6-5 predicts the at-rest cohesion as a function of depth, where c_{eff} = at-rest effective cohesion (psf) and z = depth behind the retaining structure. This equation was developed from a best-fit line drawn through the calculated effective cohesion points, with an intercept of 0.

$$c_{eff} = 66.2z \qquad \text{Equation 6-5}$$

Equation 6-6 is a modification of Rankine's at-rest earth pressure equation with the at-rest cohesion included. In this equation, all variables are as previously defined, but c = 28-day active pressure cohesion rather than the effective at-rest cohesion calculated in Equation 6-5.

$$\sigma_h = K_a \gamma z + K_a q - 0.2c\sqrt{K_a} \qquad \text{Equation 6-6}$$

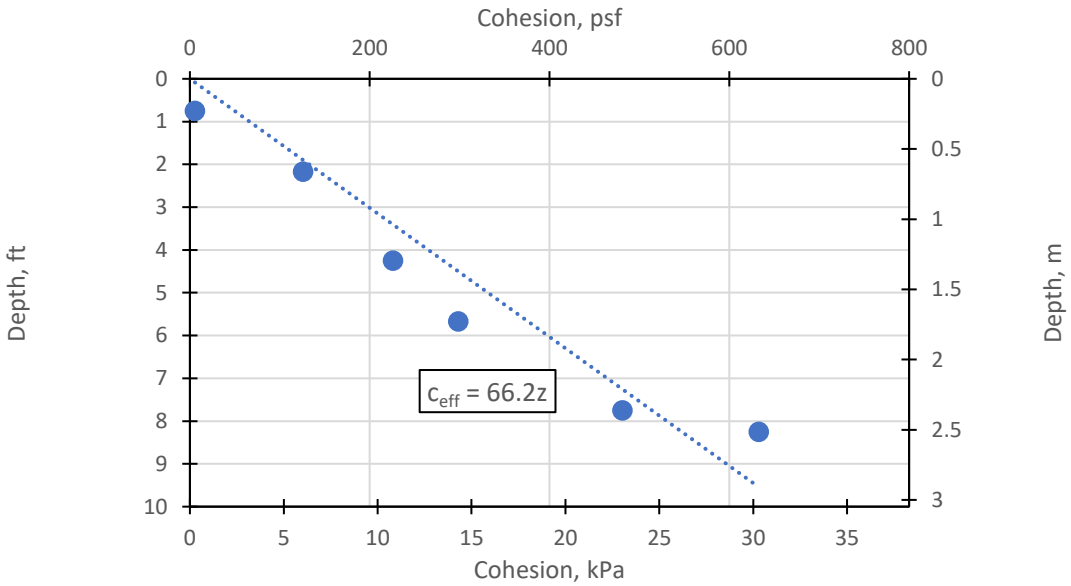

Figure 6-12: At-rest effective cohesion in the LCC block along the wall height, back-calculated from horizontal pressure measurements

All equations and trends presented in this section require further testing to confirm. Until such testing is completed, effective cohesion in the at-rest state should be ignored in design.

6.4 Lateral RCC Wall Displacement and Rotation

The movement of the RCC wall leads to additional insights about the behavior of the LCC under load. Figure 6-13 shows the deflection of the RCC wall at various surcharge levels as a function of wall height. The wall deflected with increasing applied surcharge, but the deflection was more substantial when the applied surcharge was higher. The bottom of the wall did not experience any deflection due to the restraining blocks placed against the footing.

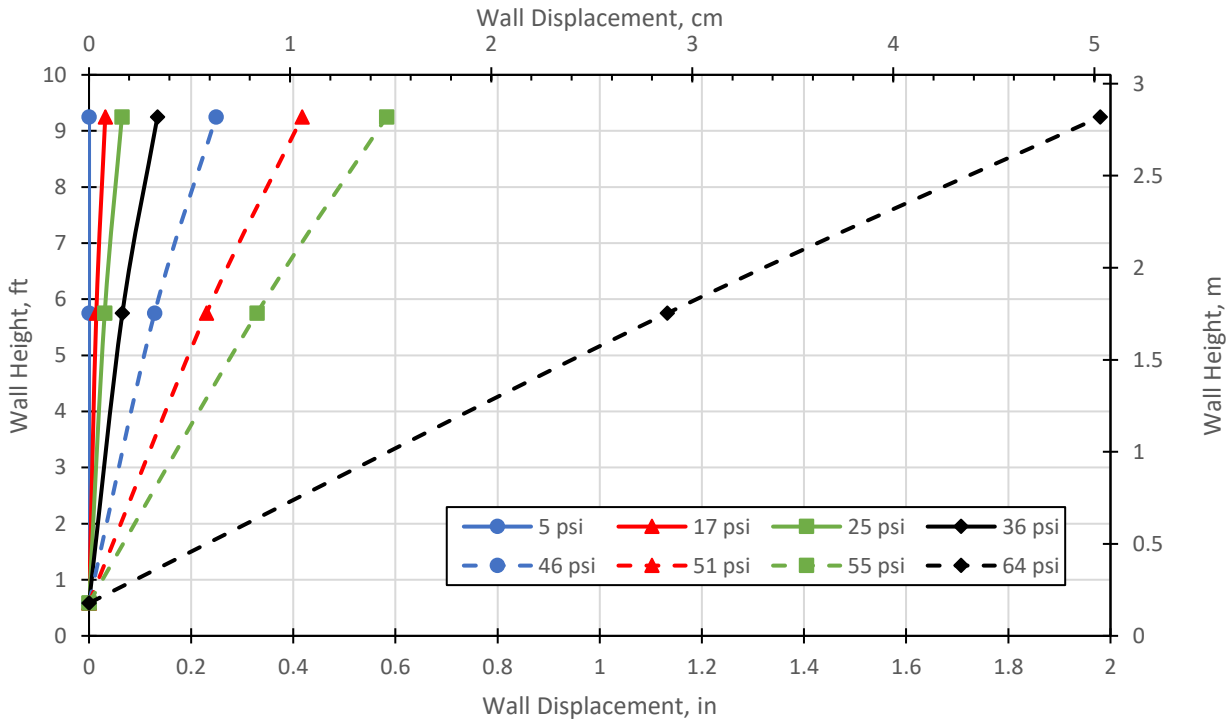

Figure 6-13: RCC wall deflection vs. height at selected levels of vertical surcharge

Figure 6-14 shows the deflection of the RCC wall as a function of surcharge for the three measured locations along the wall namely: 9'-3", 5'-9", and 7" from the base of the wall. These locations will be referred to hereafter as the top, middle, and bottom of the wall for simplicity. An additional curve has been added to this figure to show the theoretical deflection at the top of the RCC wall, Δ_{top}, should the wall rotate solely about its base using the equation

$$\Delta_{top} = \frac{d_{top}}{d_{mid}}(\Delta_{mid} - \Delta_{bottom}) + \Delta_{bottom} \qquad \text{Equation 6-7}$$

where d = height from the base of the wall to the location of the string potentiometer and Δ = deflection measured by the string potentiometer. This does not represent the anticipated behavior of the wall because the wall is not perfectly rigid with a hinge at the bottom, but it serves as a theoretical model of pure rotation.

As seen in Figure 6-14, the pure rotational deflection model predicted slightly lower deflections throughout the test than were measured, which indicates that the RCC wall was not perfectly rigid along its length; this is the expected behavior.

Though the predicted deflections are slightly lower than the measured deflections, they are very close to each other throughout the duration of the test. Because the theoretical deflection values align closely with the measured deflections at the top of the wall, the assumption that the wall failed by rotation about the base, rather than sliding, rotation about the top, or failure of the reinforcing steel in the middle of the wall, is valid. Knowing the mode of failure is critical for proper analysis and will be explored in later sections.

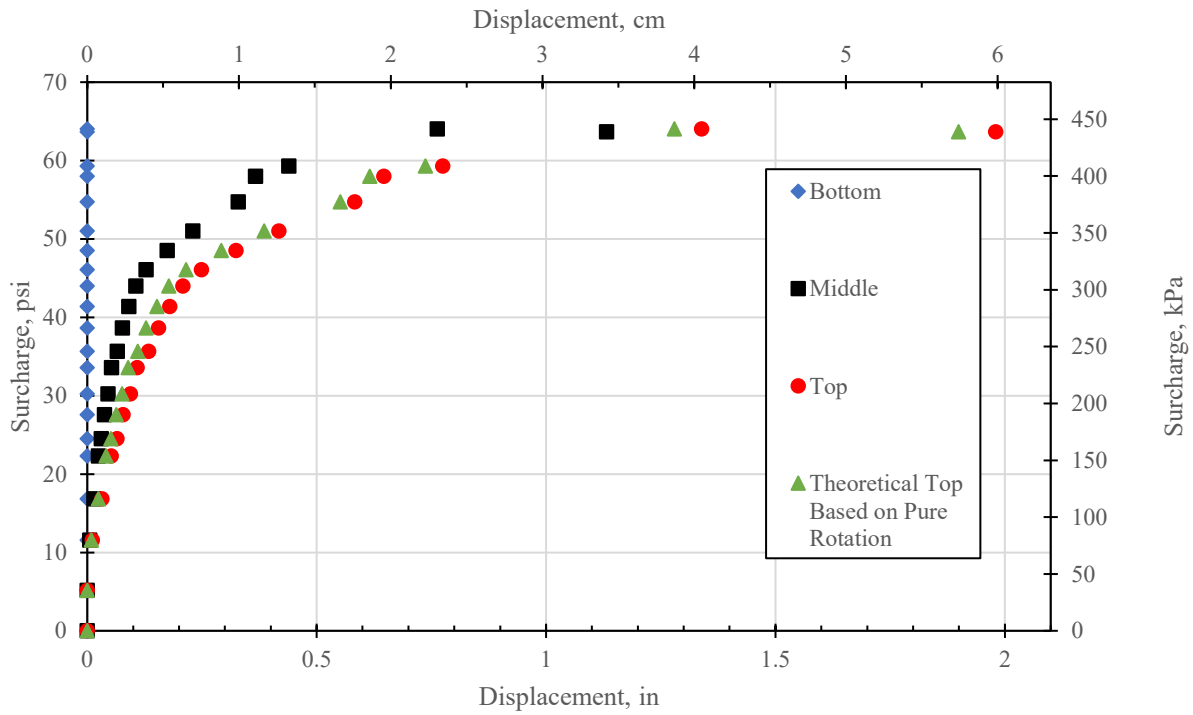

Figure 6-14: RCC lateral wall deflection vs. surcharge pressure measurements compared to theoretical deflections based on pure rotation about the base of the wall.

Additional insights into the wall behavior can be seen with further analysis. Figure 6-15 shows the difference between the measured deflections at the top of the wall and the deflections calculated using the theoretical rotational model, expressed as a percent using the equation

$$\Delta_d = \left(\frac{\Delta_t}{\Delta_m} - 1\right) * 100\% \qquad \text{Equation 6-8}$$

where Δ_t = theoretical deflection at the top of the wall, Δ_m = measured deflection at the top of the wall, and Δ_d = difference in deflection, expressed as a percent. Four areas of the plot have been highlighted with best-fit lines, identifying different phases of wall behavior. The regions of interest are initial deflection, elastic rotation, elastic rebound, and inelastic yielding.

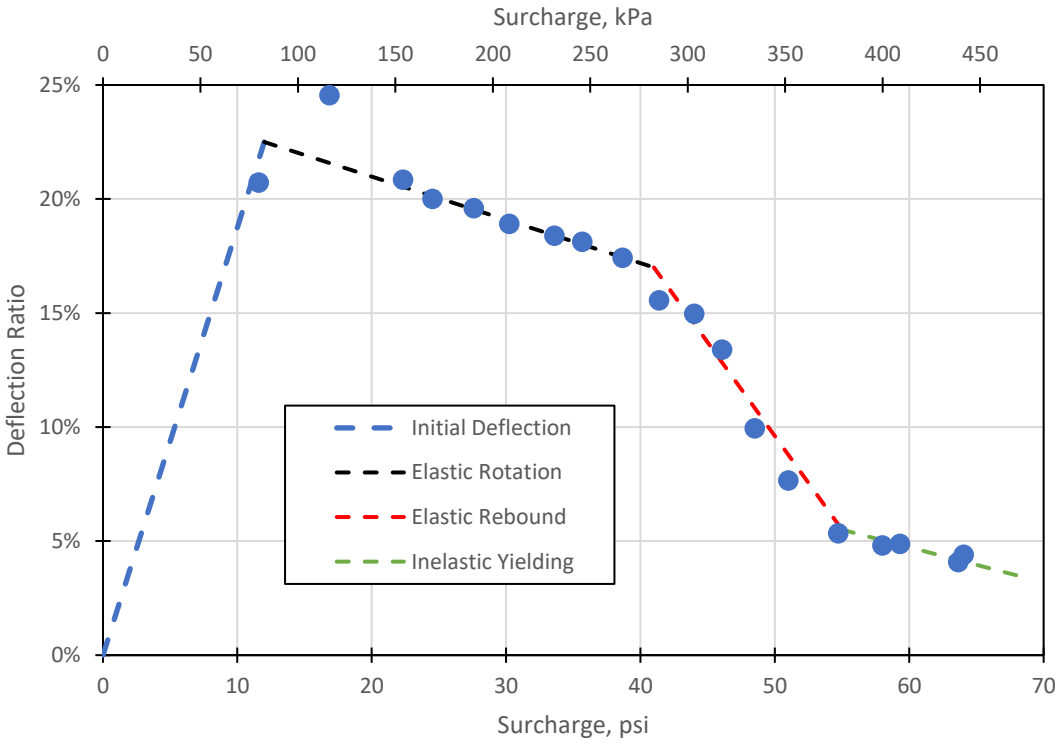

Figure 6-15: Percent difference between measured and theoretical displacement at the top of the RCC wall as a function of surcharge.

6.4.1 Initial Deflection

In the Initial Deflection region, the top of the wall deflected at a higher rate than the pure rotational model predicted. Rankine's equation for active pressure predicts that the pressure applied to the surface of the wall due to vertical surcharge is equal to qK_a (see Equation 2-3), where q is the applied vertical pressure and K_a is the active pressure coefficient. This uniform horizontal pressure applied to the surface of a retaining structure with a constant EI (modulus of elasticity multiplied by moment of inertia) is expected to deflect progressively along its entire

length rather than just rotating around its base. Therefore, during the initial deflection stage, the top of the wall is expected to deflect at a greater rate than predicted by the theoretical rotation model.

6.4.2 Elastic Rotation

The Elastic Rotation region is defined by the slight downward trend of the deflection ratio occurring immediately after the Initial Deflection region. In this region, the RCC wall deflected elastically as pressure was applied to the wall approximately uniformly. The higher applied moment at the base of the wall inherently implies a slight decrease in the deflection ratio because the bottom is expected to deflect at a higher rate than the top.

6.4.3 Elastic Rebound

At approximately 40 psi, the deflection ratio pitched sharply downward. This is indicative of the point where the RCC wall had deflected enough to allow the elastic deformation near the top of the wall to be released. Initial yielding at the base of the wall likely occurred just prior to this point. Additional discussion on the yield point is given in Section 6.5.

Yielding occurs as a plastic hinge is formed at the base of the wall, allowing very rapid deflection with little or no increase in applied moment. In this test, the wall deflected such that the measured pressure near the top of the wall began to decrease at a surcharge of approximately 40 psi. Such a decrease in pressure allowed the elastically-deformed wall to partially rebound as it continued to yield at the base, thereby decreasing the ratio between the measured and theoretical deflections. Figure 6-16 compares the wall deflection behavior to the measured horizontal pressure at a depth of 0.75 ft (0.23 m). The elastic rebound region aligns very well with the point at which the measured horizontal pressure began to decrease, reinforcing the

accuracy of the pressure measurement at this location. It is more likely that the decrease in measured pressure was caused by the rotation of the wall than by faulty measurements.

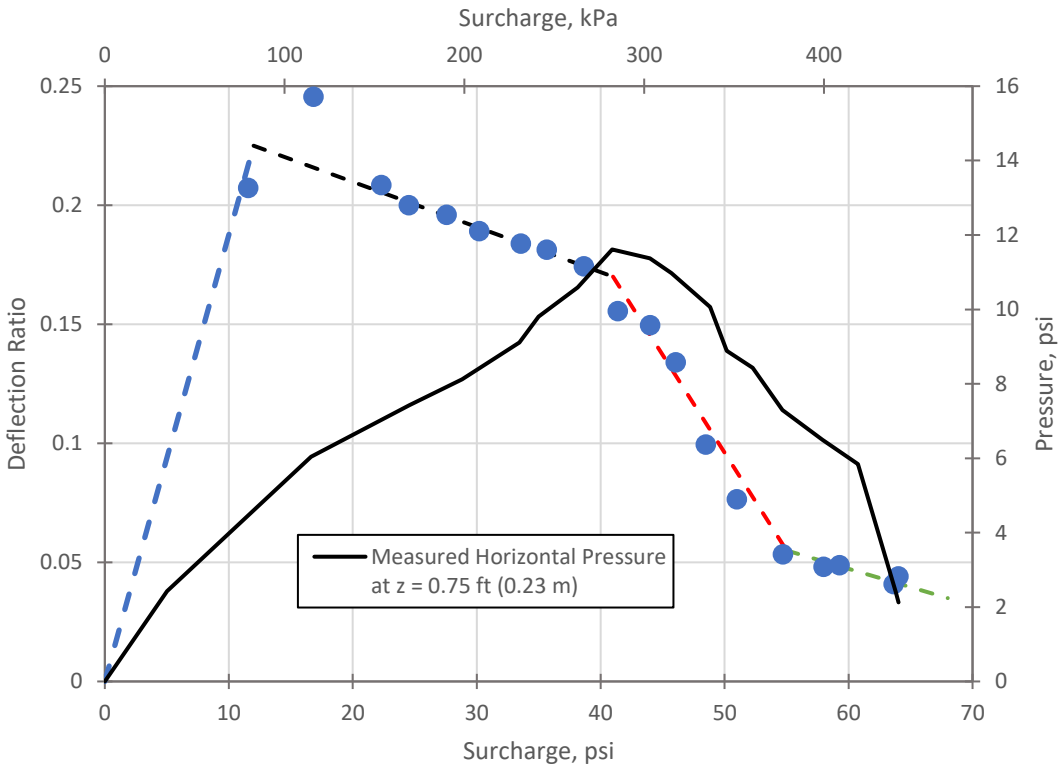

Figure 6-16: Wall Deflection Behavior Compared to Horizontal Pressure at Wall Top

6.4.4 Inelastic Yielding

In the final region, the slope of the deflection ratio returns to approximately the same as seen in the elastic rotation region. The elastic rebound in the wall was largely complete at this point, and additional applied surcharge simply caused the wall to deflect more. Very little elastic

rebound or additional elastic deformation is seen in this region—nearly all the deflection was caused by continual inelastic yielding of the RCC wall.

6.5 RCC Wall Yield Point

Figure 6-17 shows the lateral displacement at the middle and top of the RCC wall as a function of the applied surcharge. The base of the wall was pinned against a reaction frame and experienced no measurable movement. At a surcharge of 34 psi, the displacement of the wall ceased to be linear and began increasing rapidly with little increase in surcharge. A second change in the yield curve occurred at approximately 44 psi, where the deflection increased yet more rapidly with additional surcharge.

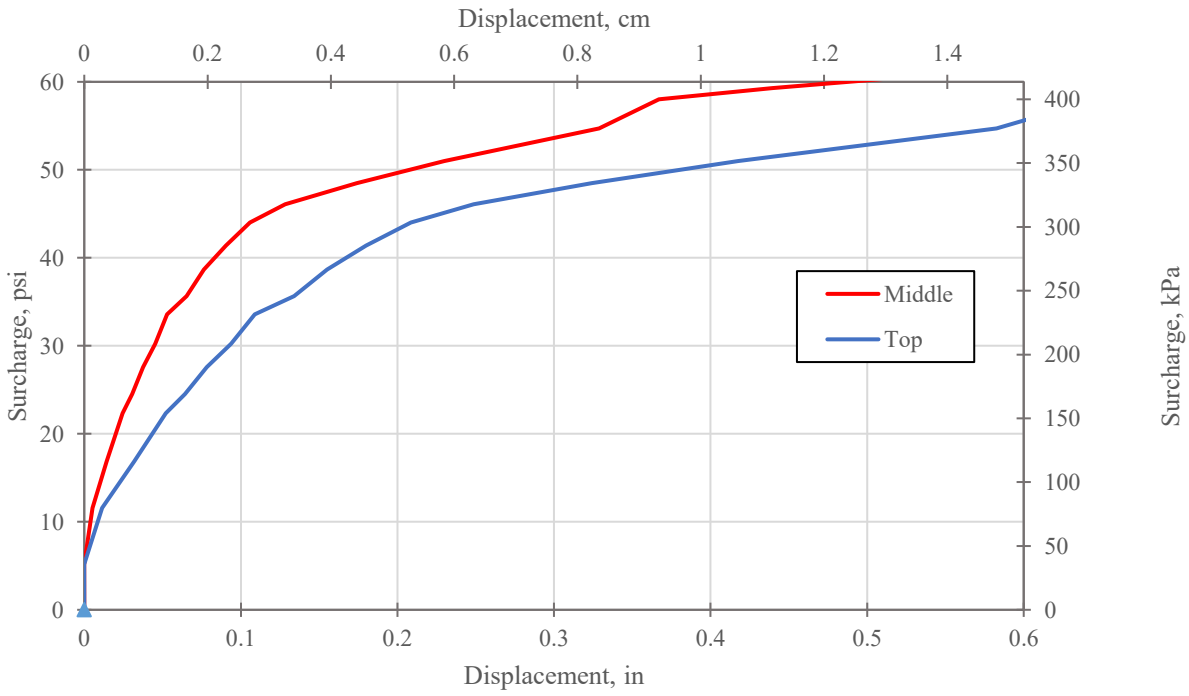

Figure 6-17: Measured lateral wall deflections at the middle and top of the RCC wall as a function of vertical surcharge pressure.

The RCC wall was designed using LRFD design methodology to resist a maximum moment of 27.1 k-ft (36.8 kN-m). Assuming the pressure on the stem of the wall is uniformly distributed along the entire wall length, the maximum design pressure to achieve this moment is 4.9 psi (34 kPa). The measured horizontal pressure at both yield points (34 psi and 45 psi vertical surcharge) was approximately 7.5 psi (see Figure 6-10), which is much higher than the design yield pressure. However, the design yield pressure accounts for a strength reduction factor, phi, of 0.9. From Table A3.1 in the ANSI/AISC Seismic Design Provisions manual, a factor of 1.2 (R_y) is to be applied to the yield stress of ASTM A615 Gr. 60 reinforcing steel in place of the strength reduction factor, phi, to determine the expected yield stress (ANSI, 2016). This factor accounts for extra strength that may be present in the steel since the minimum required yield stress of 60 ksi (414 MPa) is a minimum requirement, not an average among all the steel produced by a given manufacturer. An additional factor of 1.1 is also applied to account for residual strength that may be present in other members. Using these factors, the expected maximum moment capacity at the base of the wall is 39.8 k-ft (54.0 kN-m), which is developed by a uniform pressure of 7.2 psi (49.8 kPa) applied to the full wall surface. This is very close to the maximum applied average pressure measured at the RCC wall.

Figure 6-18 shows the average measured pressures compared to the design and expected yield pressures for the RCC wall. At approximately 34 psi surcharge, the average measured pressure reached the expected yield point of the wall. This corresponds very well to the yield point seen in Figure 6-17.

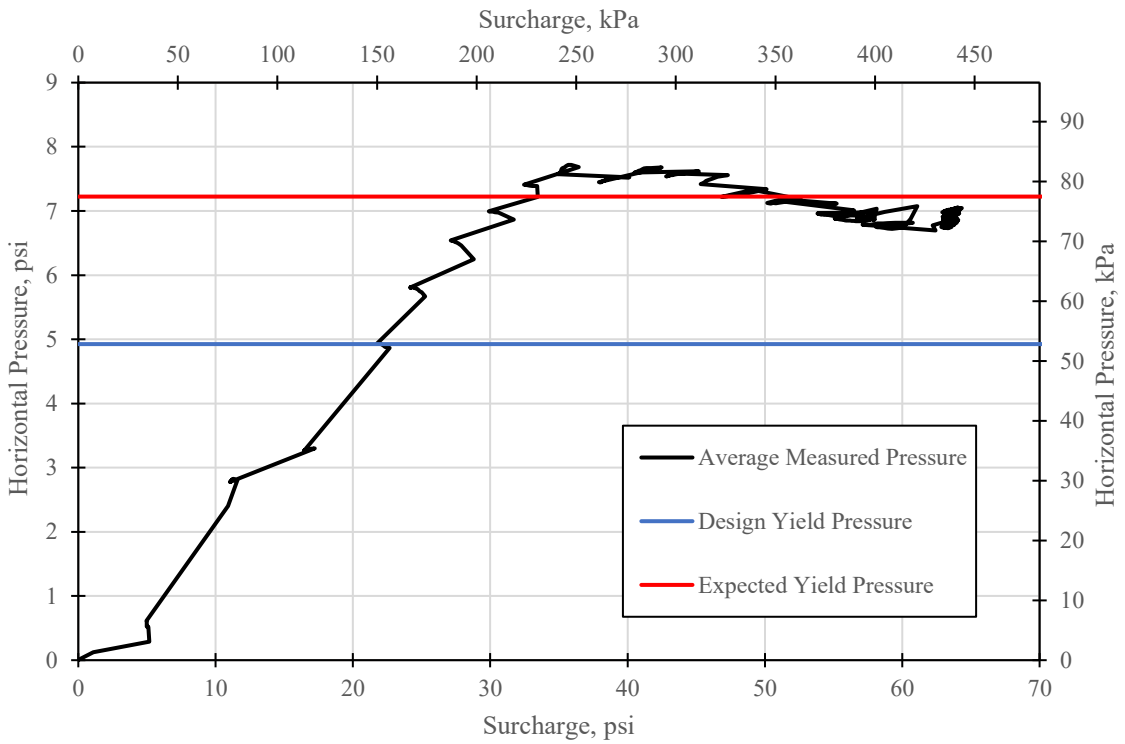

Figure 6-18: Average measured horizontal pressures on the RCC wall compared to the design and expected yield pressures for the wall

6.6 Temperature Effects

Temperature data was recorded inside each lift of LCC and at the face of every pressure plate. Because the RCC retained-face test was performed when the LCC had cured between 4 and 7 days, temperatures inside the LCC block were still higher than the ambient room temperature due to residual heat from hydration. The effects of temperature did not appear to have a significant influence on the performance of the LCC. Figure 6-19 shows the variation in temperature during the test as a function of time. No clear steps or unusual trends can be seen in the chart, and the cooling after initial hydration in each of the lifts and at each plate was consistent.

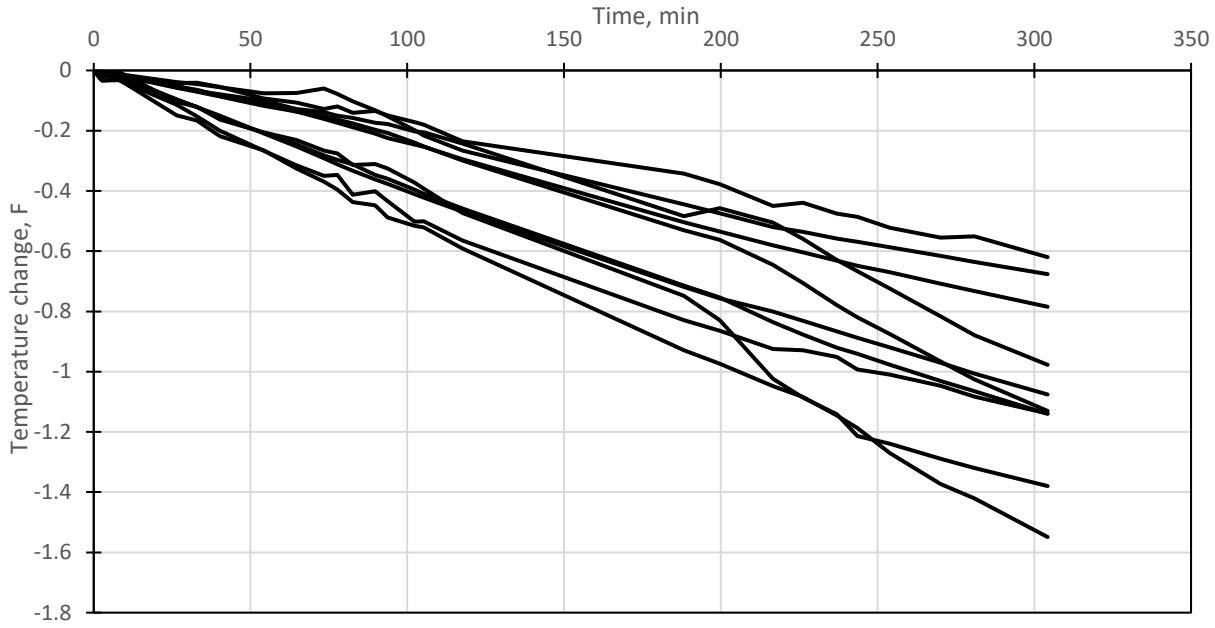

Figure 6-19: Temperature change vs. time during the RCC test

6.7 Summary of Results

Owing to the large amount of data gathered in this test, a summation of the results of the RCC test is helpful before comparing these results to the results of the free-face test, which are presented in Chapter 7.

The LCC block most closely behaved like soil with both a defined friction angle and cohesion. The friction angle, interpreted from the horizontal pressures measured at the face of the RCC wall, is approximately 34º. The cohesion of the LCC was calculated assuming a friction angle of 34º and was approximately 1460 psf. The axial yield stress of the LCC was determined to be approximately 51.5 psi at a vertical strain of 0.62%, with an elastic modulus of 17700 psi. The LCC supported an ultimate surcharge stress of 64 psi, at which point the test was stopped

because the axial strain was increasing rapidly with no increase in load. Its ability to resist the surcharge load did not diminish as it strained, but rather remained constant (see Figure 6-5).

The RCC wall yielded by rotating about the base as it was designed to. The measured pressure on the wall reached a maximum point and did not increase thereafter, which is consistent with the expected behavior of yielding steel reinforcement. After the wall began to yield, it rotated away from the LCC block at a rapid rate, but the surcharge applied to the surface of the LCC increased further until it reached an ultimate stress of 64 psi. The transition between the at-rest and active pressure states allowed the inherent cohesion in the material to support this additional surcharge.

These test results largely agree with the tests conducted by Tiwari et al. (2017) and Black (2018), where the friction angle of LCC was determined to be between 34º and 35º, with a 28-day cohesion between 700 and 1600 psf.

7 FREE-FACE TEST RESULTS

The free-face test was performed 48 hours after the RCC test. In the time between tests, instrumentation was adjusted and the wood wall panels on the East side (opposite the RCC wall) of the steel reaction frame was removed. The steel beams on the East side of the frame were left in place to maintain the structural integrity of the reaction frame, but a 6" gap between the surface of the LCC and the beams remained to ensure the LCC could move freely without interference from the beams. The LCC surface was loaded as shown in Figure 3-10, with the total surcharge area extending 6'-0" from the free face for a total surcharge area of 60 ft^2. The loading procedure was carried out in the same manner as the RCC retained-face test Similar results and analysis will be presented in this section as were presented in Chapter 6. Comparisons between the results from these two tests provide improved insight regarding the improved performance provided by the presence of the RCC wall.

7.1 Vertical Displacement Due to Applied Surcharge Pressure

The vertical displacement of the cellular concrete was measured with a series of nine string potentiometers, with three potentiometers located on each of the three concrete surcharge beams that were loaded during this test. Figure 7-1 presents the vertical strain of the LCC block during the free-face test as a function of surcharge pressure. The strain increases linearly with an increase in pressure until ultimate failure was reached at a stress of approximately 45 psi and a

strain of 0.6%. This is the approximately the same strain as was observed in the RCC wall test when the displacement of the RCC wall accelerated After the material failed, the strain increased rapidly and the surcharge pressure which could be supported by the wall decreased by about 66% from the peak.

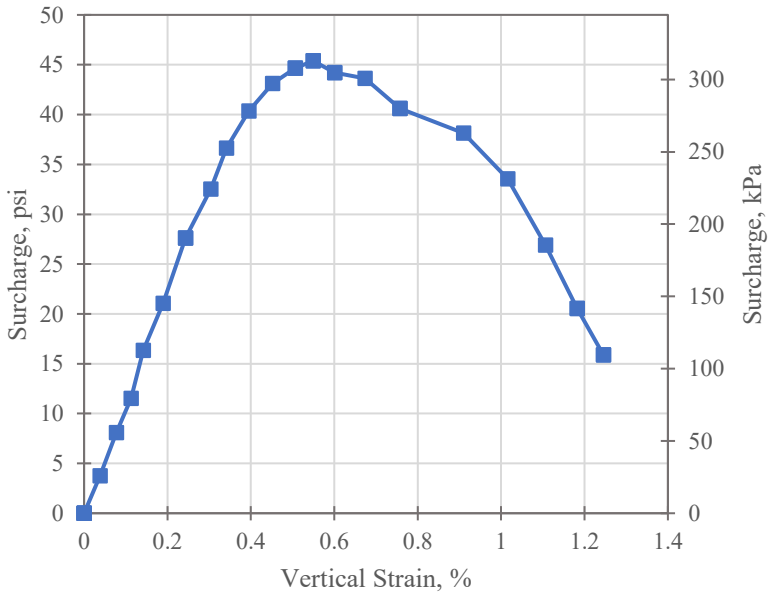

Figure 7-1: Average surcharge stress vs. vertical strain curve for the free-face test

Figure 7-2 compares the behavior of the free-face and RCC tests over a larger strain range. The stress-strain curves for the two tests are very similar up to a surcharge pressure of about 44 psi (303 kPa), although the material in the RCC test is slightly stiffer. This similarity suggests that resistance is primarily being provided by the LCC itself in both cases. However, stress-strain curves diverge significantly beyond this point. The stress-strain curve for the RCC increases up to a failure pressure of about 64 psi (425 kPa), owing to the increased resistance

provided by the RCC wall, and experiences a relatively ductile failure in which the surcharge pressure is maintained while the axial strain increases. In contrast, the stress-strain curve for the free-face test loses strength post-peak and experiences a catastrophic failure. This would pose substantial consequences should this type of failure happen in a field application where the applied load would remain constant. The difference between the brittle and ductile failure of the two tests illustrates the improved performance provided by the RCC wall in comparison with the free-face condition.

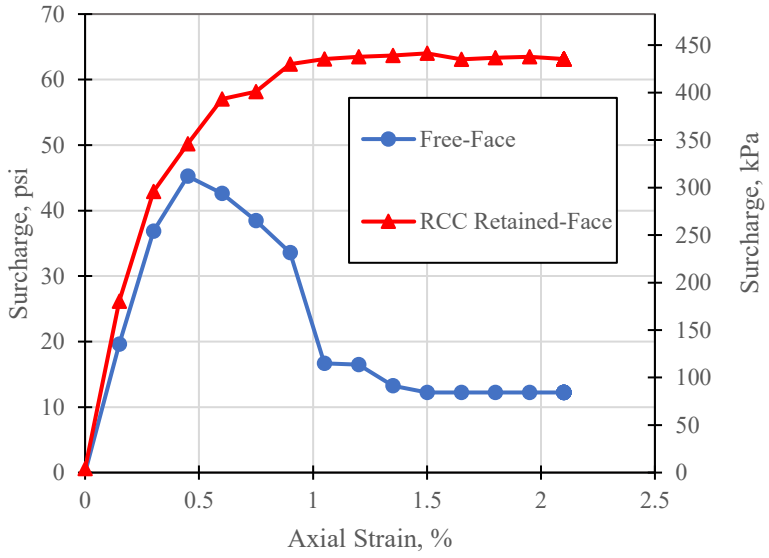

Figure 7-2: Comparison of surcharge stress vs. vertical strain between the RCC Retained-Face and Free-Face Tests

From these charts, it is clear that the cellular concrete is stronger and more predictable when a retaining structure is present than when one face is exposed and unrestrained. The free-face test reached a point of ultimate failure, while the RCC retained-face never failed catastrophically. Neither test reached the unconfined compressive strength of the tested

cylinders, which was about 100 psi (see Section 5.2.1), but both tests sustained a surcharge pressure equal to the minimum 28-day unconfined compressive strength of 40 psi specified in the mix design. This may question the validity of using sample cylinders to predict the strength of a large backfill mass when a shear plane is likely to be induced, but exploring such a possibility is outside the scope of this research.

7.2 Lateral Displacement Due to Applied Surcharge Pressure

A series of nine string potentiometers were anchored to the East face of the LCC block prior to testing with 1" eyelet screws inserted into OSB blocks glued to the surface of the LCC with quick-set epoxy. As surcharge was applied, the face of the block cracked and bulged, causing a wide variety of readings on the potentiometers, especially as the surcharge approached the point of ultimate failure. Figure 7-3, a photo from the preliminary test, shows the magnitude of the cracking and bulging in the LCC after the free-face test was completed.

Figure 7-3: Cracking and bulging of the East face of the LCC block after the free-face test

Averaging the displacement measurements of all nine string potentiometers on the wall provides a reasonable depiction of the overall behavior without the effects of localized cracking and bulging. Figure 7-4 compares the lateral deflection of the RCC wall in the RCC test to the average displacement of the LCC face in the free-face test. Both tests showed very similar horizontal displacement until the LCC reached ultimate failure in the free-face condition.

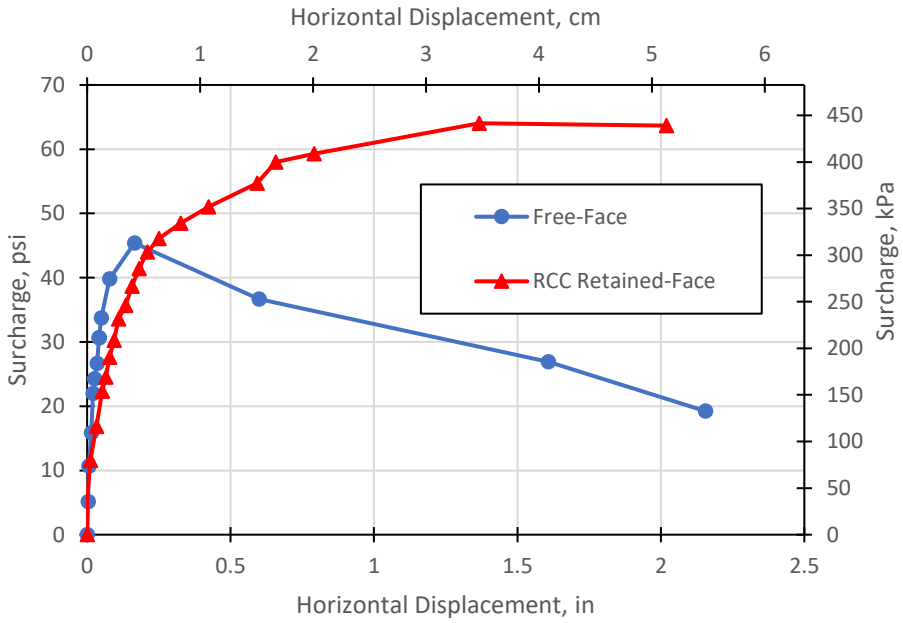

Figure 7-4: Comparison of lateral deflection in free-face and RCC retained-face tests

7.3 Failure Surface Analysis

Figure 7-5 shows the North face of the LCC block after all the tests were completed and the walls of the test box were removed. All major cracks in the material were painted after the removal of the wall: the blue cracks developed during the RCC test, while the yellow developed

during the free-face test. The approximate failure surfaces for both the RCC and free-face tests are drawn on the image in red, purple, and white, while the black lines represent the cold joints between lifts of cellular concrete.

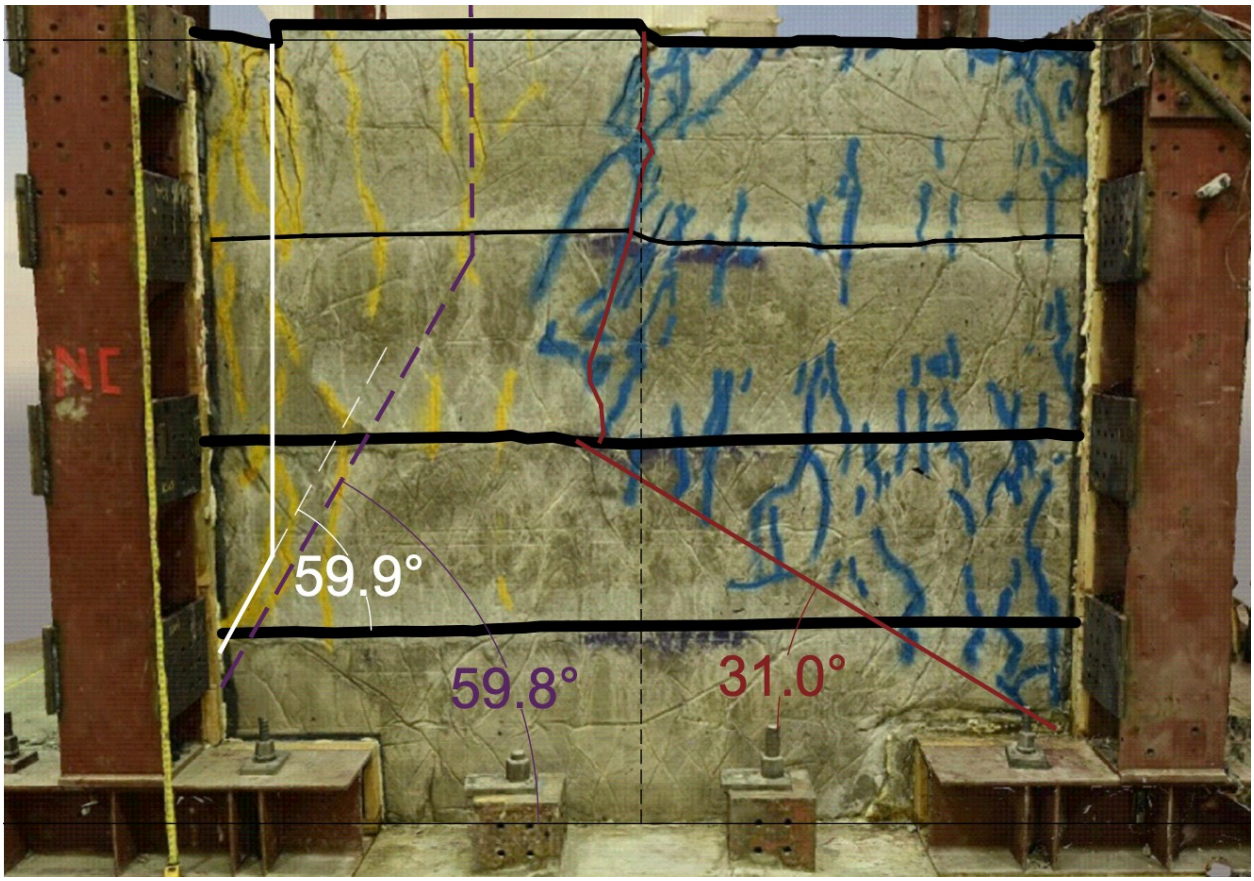

Figure 7-5: North face of LCC block with cracks and failure surfaces highlighted

In the RCC test, the LCC block was loaded from the midpoint of the block (dashed black line in Figure 7-5) to the right side of the block. The shear plane induced at the edge of the surcharge, marked in red in the top lift, lines up with this midpoint, indicating that the failure of this lift was caused by the induced shear plane from the surcharge. Though an active failure wedge did not completely break away from the main block, no cracks originated below the 31º

diagonal line shown. This line has been marked as a potential failure surface even though it never fully developed.

In the free-face test, a full active pressure failure wedge did develop. Marked in white, this wedge formed approximately 2’ away from the wall face even though the surcharge pressure for this test extended back 6’ from the face. Like the RCC test, the failure wedge aligned with the edge of one of the concrete surcharge beams. The active pressure failure wedge developed at an angle of approximately 60º to the horizontal, and the lower bound of all the crack propagations was also approximately 60º. Further examination of the failure surface reveals a slightly spiralized shape, indicating that its failure may be more properly described by a log-spiral analysis; however, due to its short length, no definitive conclusions about the log-spiral behavior can be drawn.

A second failure wedge, marked in purple, began developing at the edge of the second concrete surcharge beam, but it never fully developed. It had a similar failure angle to the actual failure wedge.

7.4 Analysis of Friction Angle

The Rankine method for calculating active soil pressure states that the failure angle of the active and passive pressure wedges can be approximated by Equation 7-1 and Equation 7-2, respectively.

$$\theta = 45 + \frac{\phi}{2} \qquad \text{Equation 7-1}$$

$$\theta = 45 - \frac{\phi}{2} \qquad \text{Equation 7-2}$$

where θ = wedge failure angle relative to the horizontal and ϕ = friction angle of the material. Back-calculating the friction angle with $\theta = 31^{o}$, the angle of the approximate failure surface in the RCC test, the friction angle is less than 0. Because the full failure plane never developed in this test, this calculation is invalid. However, using the 60º failure angle produced in the free-face test, the friction angle is estimated to be 30º. This is slightly lower than the original estimates given by previous research, but it is within reason. It is also close to the estimated 34º friction angle calculated using the horizontal pressure measurements described in Section 6.3.1. If the wedge failure angle were interpreted as 62°, the friction angle would be 34º. Based on this observation, it is likely that the angle of the active pressure failure plane within cellular concrete can be accurately predicted using the Rankine equation.

8 ANALYSIS AND RECOMMENDATIONS

Further analysis of the results presented in Chapters 6 and 7 will be given in this chapter. Design recommendations for LCC subjected to surcharge will also be given.

8.1 Cohesion Analysis

In Section 6.3.3, the cohesion of the LCC was calculated using the ultimate applied surcharge and the horizontal stress required to yield the RCC wall, assuming a friction angle (ϕ) of 34º. The cohesion was approximately 1460 psf.

The maximum surcharge resisted by the LCC in the free-face test was 45 psi (see Section 7.1). This is markedly lower than the 64 psi maximum surcharge achieved in the RCC test. Using Equation 2-3 with q = 45 psi, γ = 28 pcf, and K_a = 0.283, the cohesion of the material is approximately 1760 psf. This is slightly higher than the estimated cohesion value calculated from the RCC test. The additional 48 hours of cure time for the LCC used in the free-face test likely led to a slight increase in cohesion, but the two values are very near each other.

Previous estimates of cohesion between 700 and 1600 psf fit the data from this test well. Because the material used in this test had an unusually high strength after only 7 days, and only a single test was performed, more specific recommendations about the cohesion of LCC will not be given until further testing is done. It is recommended that a cohesion of between 700 and 1600 psf be used in design.

The UCS of the sample cylinders was 105 psi after an average cure time of 5.5 days and 205 psi after a cure time of 28 days, a ratio of approximately 2:1. Because cohesion is closely correlated to UCS in cohesive soils, the cohesion is expected to follow the same ratio as the UCS. For cases where LCC backfill is to be loaded seven days after the last lift is placed, a design cohesion of between 350 psf and 800 psf should be used rather than the 28-day cohesion of 700 to 1600 psf.

8.2 Design Recommendations

8.2.1 Recommended Active Pressure Design

Both the RCC and free-face tests demonstrated that a friction angle of 34º accurately describes the behavior of LCC in active pressure loading conditions. This is the recommended friction angle for LCC for active pressure conditions.

Because the LCC block cured for an additional 48 hours between the RCC and free-face tests, it is likely that the material in the free-face test was slightly stronger than that in the RCC test. The difference between the 1460 psf cohesion measured in the RCC test and the 1760 psf cohesion measured in the free-face test can be reasonably explained by the additional 48 hours of cure time. Determining the rate of strength or cohesion increase of LCC over time is outside the scope of this research, but additional tests should be completed to study its behavior over time.

Using Equation 2-3 and a friction angle of 34º, with a cohesion of 1460 psf, the anticipated ultimate surcharge in the free-face condition is 37 psi. This is lower than the measured 45 psi maximum surcharge but will be used in this analysis to reduce the influence of the additional 48 hours of cure time as much as possible. The difference between this anticipated capacity and the measured ultimate surcharge capacity with the RCC wall in place is 27 psi.

Because the only difference between the two tests was the presence of the RCC wall, it can be concluded that the wall dramatically increased the bearing capacity of the LCC.

The maximum average horizontal pressure measured on the RCC wall was 7.2 psi. Dividing this pressure by the active earth pressure coefficient (K_a) of 0.283 results in a pressure of 25.4 psi. This pressure is the expected additional surcharge that can be applied to the surface of the LCC because the RCC wall is present. This pressure is very near the 27-psi difference in ultimate surcharge between the free-face and RCC conditions. This indicates that LCC behaves in accordance with Rankine's active earth pressure theory and that the RCC wall adds ultimate bearing capacity at a ratio approximately equal to the active pressure coefficient. Equation 8-1 may be used to estimate the ultimate bearing capacity (q_{ult}) of LCC in an active pressure state. This equation applies to both free-face and retained conditions, with σ_{wall} equal to 0 for the free-face condition. Equations 8-2 and 8-3 may be used to calculate the required design strength of the RCC wall when a uniform surcharge is applied to the top of the LCC backfill. In these equations, all variables are as previously defined, with H equal to the height of the retaining wall and q_{ult} equal to the ultimate surcharge. M_n is defined as the moment capacity of the retaining wall per unit length, which may be governed by the yield strength of the wall, bearing capacity of the soil, or other failure mechanism determined by the design professional.

In cases where sliding, rather than rotation, governs the capacity of the retaining wall, the term σ_{wall} in Equations 8-1 and 8-2 may be defined as the uniform pressure applied to the face of the wall required to induce sliding, or the maximum uniform pressure that can be exerted by the wall on the LCC backfill before failure. Further research is needed to confirm this recommendation because sliding was not explicitly tested in this research.

$$q_{ult} = \frac{\sigma_{wall}}{K_a} + \frac{2c}{\sqrt{K_a}} - \gamma z$$ Equation 8-1

$$\sigma_{wall} = K_a \gamma z + K_a q_{ult} - 2c\sqrt{K_a}$$ Equation 8-2

$$\sigma_{wall} = \frac{2M_n}{H^2}$$ Equation 8-3

8.2.2 Design Recommendations Based on UCS

LCC is typically classified by its density and UCS rather than friction angle and cohesion. Because cohesion tests are not regularly performed on LCC samples while UCS tests are extremely common, equations relating the UCS and the ultimate bearing capacity are helpful for design.

The sample cylinders had an average UCS of 105 psi at the time of the RCC test and 205 psi after 28 days. The ratio of the free-face maximum surcharge load, 45 psi, to the average 28-day UCS is approximately 0.2. The ultimate bearing capacity of LCC subjected to a surcharge load may be estimated using Equation 8-4, where UCS_{28} is the average 28-day strength of the material, and all other variables are as previously defined. An upper limit has been placed on the ultimate surcharge so as to not exceed the UCS of the material. Further research is required to determine the behavior of the LCC subjected to surcharge higher than the material UCS.

$$q_{ult} = 0.2UCS_{28} + \frac{\sigma_{wall}}{K_a} < UCS_{28}$$ Equation 8-4

8.2.3 Comparison to Other Recommendations

Figure 8-1 compares the stress-strain curve of the free-face test with the ultimate surcharge pressures for the free-face condition proposed by other researchers. These maximum pressures were derived using Rankine's active earth pressure equation, using the recommended friction angle and cohesion values in each publication. These recommendations were given in Table 2-3, but the design parameters of each recommendation are repeated here for convenience. The final design recommendation from Tiwari et al. (2017) shown in Table 2-3 was directed toward design of LCC in the at-rest pressure state; however, the recommendation shown in Figure 8-1 is based on the static material property findings presented in that publication.

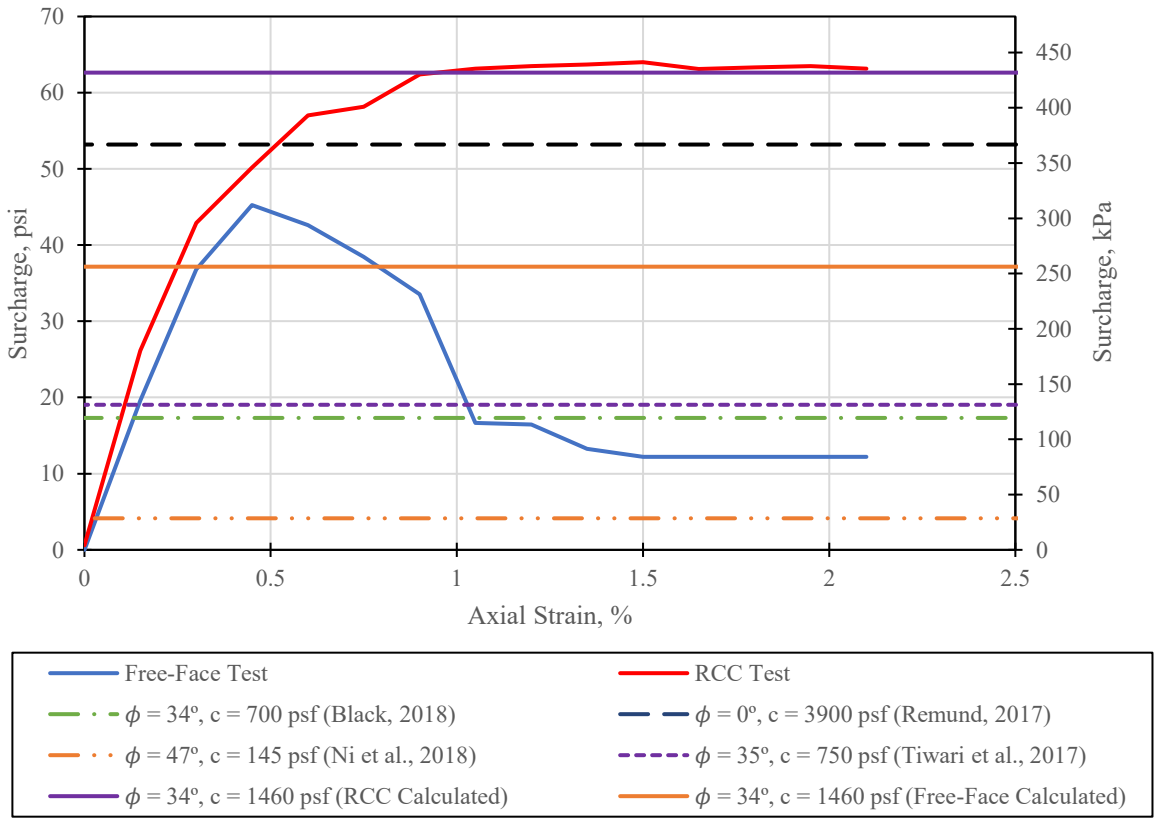

Figure 8-1: Cellular concrete design recommendations from previous research compared to measured data and proposed design recommendations in this research.

The estimate of $\phi = 0^{o}$ and c = 3800 psf, given by Remund (2017), over-estimates the bearing capacity of the LCC and should not be used for the active pressure condition. The other three estimates provide very conservative bearing capacities but may be appropriate for general design. These recommendations result in a design strength with a safety factor of between 2.0 and 2.5 against catastrophic failure.

8.2.4 Free-Face vs RCC Design Recommendations

The LCC that was supported by the RCC wall was able to continuously support the ultimate surcharge pressure as it strained axially; conversely, the LCC in the free-face condition lost approximately 70% of its strength when the ultimate load was reached. If such an abrupt loss of strength were to occur outside the laboratory environment, the consequences could be catastrophic. For this reason, it is recommended that LCC embankments be constructed with a retaining wall rather than left in the free-face condition when large surcharge loads are anticipated. Adding a retaining wall will add a measure of certainty that catastrophic strength loss will not occur should the ultimate surcharge pressure be reached.

In situations where the maximum anticipated surcharge is light, it may be appropriate to leave an LCC embankment in the free-face condition. However, as previously discussed, the durability of the exposed face should be considered if such a design is provided. Vehicle impacts, freeze/thaw cycles, animals, and weather events may all degrade the face such that it becomes unable to support the design load. Adding a retaining structure will reduce the likelihood of external forces negatively impacting the LCC's bearing capacity.

8.2.5 Scalability of Results

In this research, laboratory limitations required that active pressure be developed through yielding of the stem of the RCC wall. In retaining walls constructed in the field, active pressure is usually developed through settlement of the base soil or elastic deformation of the retaining structure, or some combination of these mechanisms. It may also be developed by small degrees of sliding on the base soil, though such sliding usually causes the top of the wall to rotate in conjunction with the sliding. It is rarely developed through yielding of the retaining structure as this mechanism requires structural failure.

Rankine's active earth pressure equation does not require that active pressure be developed through sliding or rotation, or some combination of the two. The only requirement is that active pressure is developed, which requires movement at the top of the retaining structure as discussed in Section 6.3.4. If sufficient movement does not occur, the pressure applied to the retaining structure is better described using at-rest pressure coefficients and equations.

In the tests performed in this research project, the friction angle of LCC subjected to surcharge load was determined to be 34º, with a cohesion value between 700 and 1600 psf for conditions where the wall failed by rotation. Though the testing did not explore the behavior of LCC in an active pressure condition caused by sliding of the retaining wall, or a combination of sliding and rotation, it is likely that the behavior will be the same regardless of how the active pressure condition is achieved.

This research was also limited to exploring the behavior of a single wall and loading scenario rather than multiple sizes and configurations. Additional research is required to confirm that the recommendations provided herein apply to apply to a multitude of situations; however, because the friction angle and cohesion based on small laboratory material tests (Tiwari et al.,

2017), as well as the values based on large-scale passive pressure tests (Black, 2018), coincide almost perfectly with the values seen in the active pressure tests performed in this study, there is very little evidence to suggest that these results are not scalable or that different design values need to be used for different loading scenarios.

9 CONCLUSIONS AND RECOMMENDATIONS

9.1 Conclusions

1.) The presence of a reinforced concrete cantilevered retaining wall can help increase the strength of LCC backfill at a rate proportional to the strength of the wall. The wall provides little increase in stiffness but can increase the ultimate bearing capacity.

2.) A concrete retaining wall enables the LCC backfill to continuously support an ultimate surcharge pressure rather than abruptly losing strength after failure.

3.) Stress concentrations on the surface of cellular concrete backfill may induce shear planes. These induced planes reduce the bearing capacity of the material to approximately 50% of its unconfined compressive strength.

4.) LCC gains strength and stiffness as curing time increases. This increase may lead to more brittle material behavior with increased time.

5.) Class II LCC behaves most similarly to a material with a friction angle of 34º and a cohesion between 700 and 1600 psf. For a conservative design, the cohesion may be taken as 700 psf, but using a higher cohesion may be appropriate if verified by laboratory testing.

6.) LCC subjected to surcharge load behaves in accordance with Rankine's earth pressure theory.

9.2 Recommendations for Future Research

More accurate representations of the behavior of cellular concrete could be created with additional testing data and more consistent material quality. The variability inherent in cellular concrete makes it difficult to accurately anticipate the strength of each batch, but additional research and better casting techniques may lead to a more consistent material and more accurate design criteria.

Another recommendation is to perform multiple smaller-scale tests to determine the effect of cure time on the behavior of the cellular concrete. Testing after various cure times would illustrate the importance or the insignificance of cure time on horizontal pressure development and material cohesion.

A final recommendation is to research the effect of density on horizontal pressures. Performing multiple small-scale tests with varying densities would facilitate the development of design criteria for other classes of LCC. The density is usually the key identifier of LCC so correlations between behavior and density are crucial.

REFERENCES

Abdul Rahman, M., Ahmad Zaidi, A., & Abdul Rahman, I. (2010). Analysis of comparison between unconfined and confined condition of foamed concrete under uni-axial compressive load. *Engineering and Applied Sciences, 3*(1), 62-72.

ANSI, A. (2016). 341–16.(2016). *Seismic provisions for structural steel buildings, 60601*.

Averyanov, S. (2018). *Analysis of construction experience of using lightweight cellular concrete as a subbase material.* University of Waterloo,

Black, R. E. (2018). Large-Scale Testing of Low-Strength Cellular Concrete for Skewed Bridge Abutments.

Caltrans. (2014). *Caltrans Geotechnical Manual - Ground Improvement*.

Chen, L. (2014). Active earth pressure of retaining wall considering wall movement. *European journal of environmental and civil engineering, 18*(8), 910-926.

Cox, L. S. (2005). Major Road and Bridge Projects with Foam Concrete.

Deni, N., & Gladstone, R. A. (2019). *Low-Density Cellular Concrete in MSE Structures with Steel Strip Reinforcements—Design and Construction Considerations and Case Histories.* Paper presented at the Geo-Congress 2019: Earth Retaining Structures and Geosynthetics.

Duncan, J. M., & Mokwa, R. L. (2001). Passive earth pressures: theories and tests. *Journal of Geotechnical and Geoenvironmental Engineering, 127*(3), 248-257.

Elastizell. (2014). *Technical Data Sheet for Elastizell EF (Engineered Fill)*. Retrieved from Ann Arbor, Michigan: https://cell-crete.com/build/wp-content/uploads/2018/11/Elastizell-EF-Tech-Data-Sheet.pdf

FHWA. (2017). *Geotechnical Engineering Circular No. 13 Ground Modification Methods Reference Manual*. (FHWA-NHI-16-027).

Filz, G., Reeb, A., Grenoble, A., & Abedzadeh, F. (2015). *Material properties for analysis of deep mixing support systems.* Paper presented at the Proceedings of the Deep Mixing 2015 Conference.

Frydman, S., & Keissar, I. (1987). Earth pressure on retaining walls near rock faces. *Journal of Geotechnical Engineering, 113*(6), 586-599.

Ghanbari, A., & Taheri, M. (2012). An analytical method for calculating active earth pressure in reinforced retaining walls subject to a line surcharge. *Geotextiles and Geomembranes, 34*, 1-10.

Greco, V. R. (2005). Active earth thrust by backfills subject to a line surcharge. *Canadian Geotechnical Journal, 42*(5), 1255-1263.

Grutzeck, M. W. (2005). Cellular concrete. *Cellular Ceramics: Structure, Manufacturing, Properties and Applications*, 193-223.

Guide for Cast-in-Place Low-Density Cellular Concrete. (2006). *ACI 523*(ACI 523.1R-06).

Güneyli, H., & Rüşen, T. (2016). Effect of length-to-diameter ratio on the unconfined compressive strength of cohesive soil specimens. *Bulletin of Engineering Geology and the Environment, 75*(2), 793-806. doi:10.1007/s10064-015-0835-5

Incorporated, E. (2016). *Unconfined Compression Testing (ASTM C495)* (13057.000.000). Retrieved from Yorba Linda, CA:

Jones, M. R., Ozlutas, K., & Zheng, L. (2016). Stability and instability of foamed concrete. *Magazine of Concrete Research, 68*(11), 542-549.

Matsuzawa, H., & Hazarika, H. (1996). Analyses of Active Earth Pressure Against Rigid Retaining Wall Subjected to Different Modes of Movement. *SOILS AND FOUNDATIONS, 36*(3), 51-65. doi:10.3208/sandf.36.3_51

Mohd Sari, K. A., & Mohammed Sani, A. R. (2017). *Applications of foamed lightweight concrete.* Paper presented at the MATEC Web of Conferences.

Nandi, S., Chatterjee, A., Samanta, P., & Hansda, T. (2016). Cellular concrete and its facets of application in Civil Engineering. *International Journal of Engineering Research, 5*(1), 37-43.

Ni, F. M.-W., Averyanov, S., Melese, E., & Tighe, S. (2018). Characterization of Lightweight Cellular Concrete.

Pradel, D., & Tiwari, B. (2015). *The use of MSE walls backfilled with lightweight cellular concrete in soft ground seismic areas.* Paper presented at the Proceedings of the Third International Conference of Deep Foundations.

Rahman, M. Z. A. A., Zaidi, A. M. A., & Rahman, I. A. (2010). Physical Behaviour of Foamed Concrete under Uni-Axial Compressive Load: Confined Compressive Test. *Modern Applied Science, 4*(2), 126.

Rao, P., Chen, Q., Zhou, Y., Nimbalkar, S., & Chiaro, G. (2016). Determination of Active Earth Pressure on Rigid Retaining Wall Considering Arching Effect in Cohesive Backfill Soil. *International Journal of Geomechanics, 16*(3), 04015082. doi:doi:10.1061/(ASCE)GM.1943-5622.0000589

Remund, T. K. (2017). Large-Scale Testing of Low-Strength Cellular Concrete for Skewed Bridge Abutments.

Shang, H.-S., Song, Y.-P., & Qin, L.-K. (2008). Experimental study on strength and deformation of plain concrete under triaxial compression after freeze-thaw cycles. *Building and Environment, 43*(7), 1197-1204.

Spinney, S. C. (1993). Cellular concrete. In: Google Patents.

Standard Test Method for Compressive Strength of Lightweight Insulating Concrete. In.

Standard Test Method for Consolidated Drained Triaxial Compression Test for Soils. In.

Standard Test Method for Obtaining and Testing Drilled Cores and Sawed Beams of Concrete. In *ASTM C42*.

Stuedlein, A. W., Bailey, M., Lindquist, D., Sankey, J., & Neely, W. J. (2010). Design and Performance of a 46-m-High MSE Wall. *Journal of Geotechnical and Geoenvironmental Engineering, 136*(6), 786-796. doi:doi:10.1061/(ASCE)GT.1943-5606.0000294

Sutmoller, N. (2017). *An Introduction to Cellular Concrete and Andvanced Engineered Foam Technology*. Presentation, Aerix Industries.

Tian, W., Li, L., Zhao, X., Zhou, M., & Wang, N. (2009). Application of Foamed Concrete in Road Engineering. In *International Conference on Transportation Engineering 2009* (pp. 2114-2120).

Tiwari, B., Ajmera, B., Maw, R., Cole, R., Villegas, D., & Palmerson, P. (2017). Mechanical properties of lightweight cellular concrete for geotechnical applications. *Journal of Materials in Civil Engineering, 29*(7), 06017007.

Tiwari, B., Ajmera, B., & Villegas, D. (2018). Cyclically Induced Deformations in Lightweight Cellular Concrete Backfilled Retaining Structures. In *IFCEE 2018* (pp. 130-138).

Wagstaff, K. B. (2016). Evaluation of Passive Force on Skewed Bridge Abutments with Controlled Low-Strength Material Backfill.

Xu, S.-Y., Lawal, A. I., Shamsabadi, A., & Taciroglu, E. (2019). Estimation of static earth pressures for a sloping cohesive backfill using extended Rankine theory with a composite log-spiral failure surface. *Acta Geotechnica, 14*(2), 579-594.